ALL-OPTICAL MANIPULATION OF PHOTONIC MEMBRANES

Blair Connell Kirkpatrick

**A Thesis Submitted for the Degree of PhD
at the
University of St Andrews**

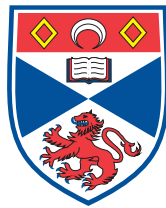**2017**

All-optical Manipulation of Photonic Membranes

Blair Connell Kirkpatrick

This thesis is submitted in partial fulfilment for the degree of

DOCTOR OF PHILOSOPHY

at the

UNIVERSITY OF ST ANDREWS

School of Physics and Astronomy
University of St Andrews
KY16 9SS
http://www.st-andrews.ac.uk/physics/synthopt/
2017-05-03

Abstract

Optical tweezers have allowed us to harness the momentum of light to trap, move, and manipulate microscopic particles with Angstrom-level precision. Position and force feedback systems grant us the ability to feel the microscopic world. As a tool, optical tweezers have allowed us to study a variety of biological systems, from the mechanical properties of red blood cells to the quantised motion of motor-molecules such as kinesin. They have been applied, with similar impact, to the manipulation of gases, atoms, and Bose-Einstein condensates. There are, however, limits to their applicability. Historically speaking, optical tweezers have only been used to trap relatively simple structures such as spheres or cylinders.

This thesis is concerned with the development of a fabricational and optical manipulation protocol that allows holographical optical tweezers to trap photonic membranes. Photonic membranes are thin, flexible membranes, that are capable of supporting nanoplasmonic features. These features can be patterned to function as metamaterials, granting the photonic membrane the ability to function as almost any optical device. It is highly desirable to take advantage of these tools in a microfluidic environment, however, their extreme aspect ratios mean that they are not traditionally compatible with the primary technology of microfluidic manipulation: optical tweezers.

In line with recent developments in optical manipulation, an holistic approach to optical trapping is used to overcome these limitations. Full six-degree-of-freedom control over a photonic membrane is demonstrated through the use of holographical optical tweezers. Furthermore, a photonic membrane (PM)-based surface-enhanced Raman spectroscopy sensor is presented which is capable of detecting rhodamine dye from a topologically undulating sample. This work moves towards marrying these technologies such that photonic membranes, designed for bespoke applications, can be readily deployed into a microfluidic environment. Extending the range of tools available in the microfluidic setting helps pave the way toward the next set of advances in the field of optical manipulation.

Candidate's declarations:

I, Blair Connell Kirkpatrick, hereby certify that this thesis, which is approximately 40,000 words in length, has been written by me, and that it is the record of work carried out by me, or principally by myself in collaboration with others as acknowledged, and that it has not been submitted in any previous application for a higher degree. I was admitted as a research student in September 2012 and as a candidate for the degree of Doctor of Philosophy in September 2012; the higher study for which this is a record was carried out in the University of St Andrews between 2012 and 2016.

Date   Signature of candidate

Supervisor's declaration:

I hereby certify that the candidate has fulfilled the conditions of the Resolution and Regulations appropriate for the degree of Doctor of Philosophy in the University of St Andrews and that the candidate is qualified to submit this thesis in application for that degree.

Date   Signature of supervisor

Permission for publication:

In submitting this thesis to the University of St Andrews I understand that I am giving permission for it to be made available for use in accordance with the regulations of the University Library for the time being in force, subject to any copyright vested in the work not being affected thereby. I also understand that the title and the abstract will be published, and that a copy of the work may be made and supplied to any bona fide library or research worker, that my thesis will be electronically accessible for personal or research use unless exempt by award of an embargo as requested below, and that the library has the right to migrate my thesis into new electronic forms as required to ensure continued access to the thesis. I have obtained any third-party copyright permissions that may be required in order to allow such access and migration, or have requested the appropriate embargo below.

The following is an agreed request by candidate and supervisor regarding the publication of this thesis:

PRINTED COPY
No embargo on print copy

ELECTRONIC COPY
No embargo on electronic copy

Date   Signature of candidate

              Signature of supervisor

Acknowledgements

During my time as a PhD student, my work has been influenced by a great many people. Primary thanks go to Andrea Di Falco, my supervisor. He has made a more mindful, focussed, and engaged researcher.

To the other members of the Synthetic Optics Group, both past and present: James Burch, Alasdair Fikouras, Adam Fleming, Xin Li, Nedyalka Panova, Monika Pietrzyk, Michiel Samuels, and Yufang Shen, thank you for being interesting, interested, and generous with your time. Special thanks goes to Peter Reader-Harris for being in equal parts helpful and silly. I would also like to extend my thanks to the various members of the Nanophotonics Group in St Andrews, led by Liam O'Faolain, who helped me understand the many processes involved in nanofabrication.

In the Department of Physics and Astronomy more generally I am extremely grateful towards Steve Balfour, Callum Smith, and Chris Booth, who maintained the cleanroom facilities and helped modify laboratory setups when necessary. I am also grateful to Scott Johnston, our Stores Manager, for his help with ordering equipment, paying conference fees, and for his friendly words of encouragement.

Finally, I wish to thank my parents for their love and support, without which I never would have made it this far. Special thanks go to Janice Kirkpatrick for taking the time to share with me her perspective on things, and for instilling in me the importance of being "a finisher". The biggest thanks of all must go to Veronica, my wife, for sticking by me through this whole process. Ours has not been the easiest road, but I am glad we walked it together.

Collaboration Statement

I would also like to thank Tomas Čižmár (University of Dundee) and Martin Ploschner (Macquarie University) for their help with the holographical optical tweezers system. They provided me with the basic design and showed me how to properly align an optical setup. Their help has been invaluable.

To Veronica. The enemy's gate is down.

Publications and Awards

Publications Resulting from this Work

- **B. C. Kirkpatrick**, M. Ploschner, T. Čižmár, and A. Di Falco, 'All-optical manipulation of photonic membranes', 2016. Submitted.

- **B. C. Kirkpatrick**, P. Reader-Harris, and A. Di Falco, 'Flexible Metamaterials for SERS applications', 2016. Submitted.

Book Chapters

- A. S. Mayer, **B. C. Kirkpatrick**, 'Silicon Photonics', in *Frontiers in Modern Optics*, ser. Proceedings of the International School of Physics "Enrico Fermi", D. Faccio, J. Dudley and M. Clerici, Eds., vol. 190, IOS Press and Società Italiana di Fisica, 2016, ch. 10, pp. 189–205.

Awards

- Newport Travel Grant, awarded by SPIE, to present paper 'All-optical manipulation of photonic membranes' at SPIE Optics and Photonics 2016, San Diego, USA. Award $670.

- Travel Grant, awarded by the Società Italiana di Fisica, for attendance of the International Summer School of Physics "Enrico Fermi", 2016, Varenna, Italy. Award €400.

Conferences

- **B. C. Kirkpatrick**, T. Čižmár, M. Ploschner and A. Di Falco, 'All-optical manipulation of photonic membranes', *Proc. SPIE 9922, Optical Trapping and Optical Micromanipulation XIII*, vol. 9922, K. Dholakia, G. C. Spalding, Eds., 99222A, Sept. 2016. Talk, presented by **B.C.K.**

- **B. C. Kirkpatrick**, T. Čižmár, M. Ploschner, A. Di Falco, 'All-optical manipulation of photonic membranes', *PECS XII, The Twelfth International Symposium on Photonic and Electromagnetic Crystal Structures, York, UK*, 2016. Poster, presented by **B.C.K.**

- P. Reader-Harris, **B. C. Kirkpatrick**, J. Wu, A. Heyerick, and A. Di Falco, 'Flexible metamaterials and new advanced photonics applications', in *9th Int. Congr. Adv. Electromagn. Mater. Microwaves Opt. - Metamaterials 2015*, 2015. Talk presented by A.D.F.

- **B. C. Kirkpatrick**, P. Reader-Harris, Y. Shen, J. Wu, and A. Di Falco, 'Advanced application of flexible metamaterials at visible frequencies', *Proc SPIE 9371, Photonic and Phononic Properties of Engineered Nanostructures V*, 93710Z, 2015. Talk, presented by A.D.F.

- P. Reader-Harris, M. Pietrzyk, Y. Shen, **B. C. Kirkpatrick**, and A. Di Falco, 'Flexible metamaterials for advanced photonics applications', in *8th Int. Congr. Adv. Electromagn. Mater. Microwaves Opt. - Metamaterials 2014*, 2014, pp. 109–111. Talk, presented by A.D.F.

- **B. C. Kirkpatrick**, T. Čižmár, M. Ploschner, A. Di Falco, 'Optical manipulation of photonic membranes for biophotonic applications', *The Physics of Soft and Biological Matter, University of Cambridge, UK*, 2014. Poster, presented by **B.C.K.**

- **B. C. Kirkpatrick**, A. Di Falco, 'Photonic Membranes for microfluidic applicaitons', *Fifth Annual SU2P Symposium, University of Strathclyde, UK*, 2014. Poster, presented by **B.C.K.**

- P. Reader-Harris, **B. C. Kirkpatrick**, and A. Di Falco, 'Design and applications of flexible photonic membranes', *Proc. SPIE 8993, Quantum Sens. Nanophotonic Devices XI*, vol. 8993, M. Razeghi, E. Tournié and G. J. Brown, Eds., 89930P, Dec. 2013. Talk, presented by A.D.F.

- **B. C. Kirkpatrick**, A. Di Falco, 'The application of optical manipulation to photonic membranes', *Fourth Annual SU2P Symposium, University of Glasgow, UK*, 2013. Poster, presented by **B.C.K.**

- **B. C. Kirkpatrick**, A. Di Falco, 'Optical manipulation of Photonic Membranes', *Application and Control of Light on the Nanoscale; Nanolight13, University of Strathclyde, UK*, 2013. Poster, presented by **B.C.K.**

- **B. C. Kirkpatrick**, A. Di Falco, 'Optical Manipulation of Photonic Membranes', *The 1st Bielefeld Workshop on Nanolayers and Artificial Membranes, Germany*, 2013. Poster, presented by **B.C.K.**

Summer Schools Attended

- International Summer School of Physics "Enrico Fermi", Course on "Frontiers in Modern Optics", Varenna, Lake Como, Italy, 30th June – 5th July, 2014.

Contents

Introduction

This thesis is concerned with the optical manipulation of photonic membranes via holographical optical tweezers. This work not only aims to extend the applicability of photonic membranes down to the microscopic scale, but also to augment optical tweezers technology by presenting a protocol that enables them to manipulate structures with extreme aspect ratios.

Here I provide some context for this work, both in terms of optical manipulation and the application of photonic membranes, before concluding with an outline of the thesis itself.

1.1   Optical manipulation

In 1619, Kepler conjectured that solar forces were responsible for pushing the tails of comets away from the Sun, leading him to believe that light carried momentum which could be transferred to physical objects. Almost three hundred years later his conjecture was confirmed by Nichols [1] and Lebedev [2], who observed this transferal of momentum in a terrestrial setting. It was not until after the invention of the laser that the field of optical manipulation really started in earnest. The earliest optical manipulation experiments were performed by Ashkin in the 1970's and 80's, in which several trapping configurations were developed [3]. These included counter-propagating traps, and optical levitation traps, but it has arguably been the configuration developed in 1986, optical tweezers, that has seen the most use in the field [4].

In an optical tweezers system a single beam of light is brought to sharp focus. Microscopic particles are drawn into the high-intensity area of the beam focus, and held there, due to a force known as the "optical gradient force". Optical tweezers allow particles and cells to be trapped and manoeuvred with Angstrom-level precision, all while measuring the external forces acting on the trapped object.

Because of this precision, and the ability to measure the properties of the local environment, optical tweezers have become commonly used tools in the field of microfluidics. They can be used to transport particles for study, moving them between various portions of a microfluidic system that have been designed to fulfil specific tasks. This could be as simple as moving a particle towards the entrance of a microfluidic channel, or holding a particle onto a sensor [5]. However, optical trapping of microscopic particles is not limited to simply allowing the trapped particles to be studied.

A complementary paradigm is to trap particles which are then used as tools themselves. The most typical "tool" that is trapped is a spherical bead, usually made from silica or polystyrene. Trapped beads have been used as microscopic objective lenses which can be manoeuvred through a sample and used to image the undersides of objects [6]. If angular momentum is imparted to a trapped bead, one can also take advantage of its rotational motion. Pairs of rotating beads have been

used to drive fluid-flow through microfluidic channels [7], with single beads demonstrated to act as micro-rheological probes [8].

The capabilities of optical tweezers have also been applied to biological systems, and enabled a lot of early studies in biophotonics. These included the trapping and manipulation a range of cells, in some cases even probing the elastic properties of the cells themselves [9]. Fundamental investigations into the mechanical behaviour of various molecules were carried out, using microscopic beads, tethered to the molecules, as handles. Thanks to these studies, kinesin, a motor molecule, was observed to move in a quantised fashion. The "steps" with which it moved were found to be directly linked the discrete spacing of deoxyribonucleic acid (DNA) base pairs, showing that the kinesin was transcribing itself along the DNA as it moved [10]. Furthermore, by measuring the force required to make such movements it was found that kinesin hydrolysed a single molecule of adenosine triphosphate (ATP) each time it moved along a base pair. In a similar experiment, a bacteria flagellum was tethered in a sample cell and optical tweezers were then used to study its rotational compliance [11]. The elastic properties of DNA and similar molecules have also been probed by trapping both ends and stretching them [12]. Large numbers of DNA strands have been interrogated simultaneously in this fashion, by trapping their two ends in standing wave patterns generated in near-by optical waveguides [13].

Optical manipulation of biological systems has been strengthened by the addition of compliment-ary optical tools such as laser scissors [14] and optical stretchers [15]. These tools have granted us the ability to probe the elastic properties of cells and even to transfect cells via optoinjection [16]. This is again another example of the advantages that can be garnered from the high precision of these techniques.

Outside of probing the mechanical properties of biological materials, optical manipulation has enabled the chemical structure of materials to be studied too. A prominent example is where optical manipulation has been used alongside other optical techniques such as Raman spectroscopy [17]. This has applied directly to particles trapped from both free-space and optical fibre-based configurations.

Advancement in the field of optical manipulation is furthered via the design and fabrication of novel tools which can be utilised in a microfluidic environment. However, quite often the structure of these tools makes them too complicated to trap directly. A relatively recent solution to this limitation is to use structure-mediated design to incorporate simple, spherical, "handles" into the structure somehow. This approach extends the applicability of optical tweezers into new regimes, and has already allowed membranes and complex three-dimensional structures to be trapped.

Structure-mediated design [18] is itself indicative of a larger trend in optical manipulation at present in which the trapping beam and the particle being trapped are given equal consideration. Historically there has been much work done in improving optical tweezers by focussing attention on the trapping beam itself. Typically this means that the beam is shaped in some way, either by having its wavefront corrected for spherical aberration [19], or by manipulating the particle via a more exotic beam (e.g. Bessel beams) [20]. In contrast, not much attention has been paid to the particle and how its properties can be harnessed to improve the trapping quality, although this is now beginning to change. Perhaps one of the most notable and elegant examples of this is the work by Jannasch et al., whereby particles given an anti-reflection coating can be trapped with nN forces [21]. This holistic approach towards optical manipulation seems both promising and exciting.

1.2 Photonic membranes

Photonic membranes are of particular interest to this thesis in their capacity to be deployed into a microfluidic environment. PM are thin, flexible membranes, typically on the order of tens of nm thick, and ranging in lateral size from 5 μm to several cm. They are particularly useful in their capacity

to host plasmonic features, whereby they effectively act as flexible metasurfaces - two-dimensional equivalents of metamaterials.

In direct analogy to conventional materials, a metamaterial (MM) is made up of meta-atoms - sub-wavelength features typically made from metal. The meta-atoms are patterned in arrays with sub-wavelength periodicity, such that the incident light does not "see" this periodicity but instead experiences a homogenous material with emergent properties. The key aspect of MMs is that their emergent properties can generally not be found in nature, e.g. negative refractive index.

Early examples of MM include stained-glass, in which metallic nanoparticles have been added in nanocolloidal form. These plasmonic features display resonant behaviour which dictates the reflection and transmission coefficients of the glass. This effect can be seen in the coloured panes of glass found in church windows, for example, whereby different colours are created by altering the plasmonic constituents of the glass. A particularly striking example of plasmonic resonances at work is the Lycurgus cup, dating back to around the 4th century A.D, which appears green in reflection and red in transmission.

The resonant behaviour of a metasurface (MS) can be engineered such that they can perform the function of any number of optical elements. MS have been demonstrated which act as lenses, filters, sensors, and axicons, just to name a few, and as such they represent a tremendously powerful tool [22], [23]. The additional advantage to using a PM as a MS is that PM are flexible. This allows the plasmonic functionality to be transferred to a broad range of objects, simply by wrapping the object with the PM.

The ability to trap PM in a microfluidic environment carries with it two main advantages. Firstly, successful manipulation of PM allows their versatile properties to be utilised in a new (microfluidic) environment. One can imagine using a PM-based sensor to take chemical readings from a group of cells, simply by moving it from cell to cell and wrapping it around them. Alternatively, one can imagine a PM patterned to act as a Fresnel lens being used for *in situ* imaging applications. Secondly, PM themselves can strengthen the field of optical manipulation by providing pathway to trapping planar features. In this regard, even a PM without plasmonic features can be useful. These "blank" PM can themselves act as ultra stable "handles" for trapping experiments, and furthermore, the fabricational techniques developed to make them can then be applied to the manufacture of a range of microfluidic tools.

As mentioned above, the main limitation surrounding these sorts of applications is that optical tweezers cannot typically manipulate planar structures like PM. This thesis outlines a fabrication and optical manipulation protocol that makes it possible to manipulate PM using optical tweezers. Full control over the translation, pitch, yaw, and roll of a PM is demonstrated, despite the PM having an aspect ratio of over 200. This demonstration paves the way toward using PM-based MS in a microfluidic setting.

1.3 Structure of the thesis

Chapter 2 presents the background physics to optical manipulation. Here the history of optical manipulation is discussed further, with a particular focus on the major ways in which the field has developed over the last fifty years. This chapter also addresses the physics of optical manipulation, looking exclusively at the case of single-beam, optical gradient trapping, or optical tweezers. The forces imparted on a trapped object by optical tweezers will be explored, as will the important properties of the trapped particles themselves i.e. polarizability, size, shape.

Chapter 3 is concerned with fabrication procedures used, developed, and in some cases created, during the course of my PhD. The chapter is broken down into distinct processing steps, such as polymer deposition, electron-beam lithography, and processing. Each of these stages is commented

on in turn, and taken together they represent a complete procedure for the fabrication of the devices presented in this thesis.

Chapter 4 discusses holographical optical tweezers, both briefly in terms of their historical perspective, and more deeply from an operational perspective. Included here is a discussion on the underlying physics of a holographical optical tweezers (HOT) system, the practical concerns regarding their calibration, and their operational limits. The section concludes with an in-depth discussion on the software that was designed and built during this thesis to control the HOT system, and to process the results obtained. Specifically, this processing of data led to the extraction of several key metrics of the HOT system, notably the trap stiffness, which allow this system to be compared to the current state-of-the-art.

Chapter 5 demonstrates the optical manipulation of PMs using HOT. Here a PM is manipulated using optical tweezers by trapping handle structures at each of its four corners. The optical traps are controlled such that the user can directly control the translation, yaw, pitch, and roll of the photonic membranes, either on-the-fly, or as part of an automated sequence movements. The performance of the system is reported, showing the trap stiffness with which the membranes are trapped.

Chapter 6 concerns the application of PM to surface-enhanced Raman spectroscopy (SERS). The ultimate aim is to apply a PM to a curved biological object, such as a cell, and take a SERS reading from it. As an intermediate step towards this goal, a PM is applied to a biological "phantom" sample that has been doped with rhodamine 6G (Rd6G). The flexibility of the PM allows it to conform to the "hills and valleys" surface of the sample and detect the Rd6G from the bottom of valley features.

Chapter 7 summarises two further avenues of interest that were explored through this thesis. These applications seed novel research directions and demonstrate the versatility of the platform. They include the development of microscopic mechanical tweezers that can be actuated using optical tweezers, and PM-based optical filters, both to be employed in a microfluidic environment.

Finally, chapter 8 is the conclusion. Here I summarise the main points of this thesis, discussing how this work has built upon previous studies and added to the current state-of-the-art in the field. The potential for development of the work presented here is also discussed.

Optical manipulation: background and theory

This chapter is summarises the underlying physics and historical background of optical manipulation. Early observations which inspired the field are summarised, and a range of the original optical manipulation schemes are discussed. One of these schemes in particular, optical tweezers, is then addressed in more detail. The basic forces which are at work in optical tweezers are outlined, as are the methods used to determine a system's performance.

Some more advanced topics are introduced, such as beam-shaping and structure-mediated design. These two advances are complementary, and represent two aspects of an holistic approach to optical manipulation where both the properties of the light and particle are given equal importance. This trend in optical manipulation is central to this thesis, and is explored further in the final section of the chapter where the optical manipulation of photonic membranes is considered.

2.1 An historical perspective of optical manipulation

2.1.1 Back-of-the-envelope calculations

The fact that light carries linear and angular momentum had been widely accepted centuries before the invention of modern-day optical manipulation, although it was not until the turn of the 19th Century, when Nichols [1] and Lebedev [2] demonstrated the transferal of this momentum to microscopic objects and gases, that the effect was measured. It appears that interest in this field began and ended with these demonstrations as the forces involved had, to quote Poynting, "...a minuteness which appears to put them beyond consideration in terrestrial affairs..." [3]. Indeed, it was not until the invention of the laser in 1960 [24] that we had access to the high light fluxes required to make optical manipulation a viable area of study.

Around this time, Arthur Ashkin, working at Bell Laboratories, became interested in the idea of light momentum following a simple "back of the envelope calculation" [3]. He considered the case of a 1 W laser, focussed down to a spot size of 1 µm, transferring its momentum to a perfectly reflective particle, also 1 µm in size. The force acting on the particle is given by

$$F = \frac{2P}{c},\tag{2.1}$$

where P is the power of the beam and c is the speed of light in vacuum, and is typically on the order of 10 nN in magnitude. Assuming a particle density of $1\,\mathrm{g\,cm^{-3}}$, this translates into a particle acceleration of $\approx 1 \times 10^9\,\mathrm{cm\,s^{-2}}$.
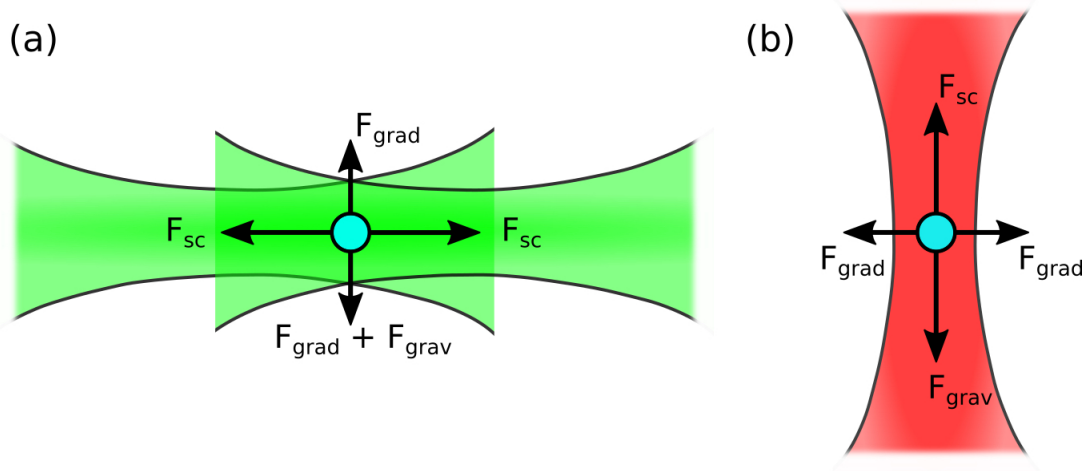
5

Figure 2.1: Common alternative schemes for optical manipulation. (a) Counter-propagating traps, whereby two weakly-focussed beams trap a particle in place by balancing each others scattering forces. (b) Optical levitation trap, where a single weakly-focussed beam has its scattering force balanced out by the gravitational force acting on the particle.

Ashkin tested his conclusion by focussing a laser on microscopic latex spheres suspended in water, and as predicted, he found that the spheres were accelerated through the water by the laser beam [25]. The force responsible for this acceleration, the scattering force, always acted along the propagation direction of the beam, and scaled directly with the beam power. What was not predicted was the presence of another optical force at work in the system. Not only were the particles pushed by the laser, but particles near to the beam focus would be drawn into it. The force responsible for this secondary behaviour was termed the "gradient force" as it acted in the direction of maximum optical intensity.

2.1.2 Early traps

From these observations Ashkin went on to create the first stable trapping system, based on two counter-propagating beams. In this setup, a beam-splitter was used to divide the input beam into two loosely-focussed beams which were made to counter-propagate. The scattering forces of the beams act to cancel each other out, while their gradient forces reinforce each other, leading to a stable trapping position [26]. It was noted that the gradient force is indeed a requirement of having a stable trapping position, and that it is not enough to simply counteract the scattering forces of the two beams (as would be the case for two counter-propagating plane waves, for example). This is analogous to the Earnshaw theorem in electrostatics, namely that it is impossible to form an equilibrium positon for a charged particle using only electrostatic fields. Indeed, when applied to optical manipulation, this theorem is often described as the optical Earnshaw theorem [27]. Ashkin also investigated a similar trapping scheme whereby a particle is trapped from below by a single laser. The scattering force from this beam is then balanced by gravity to form a so-called "optical levitation" trap [28]. Figure 2.1 shows the balancing of forces in both of these types of traps.

2.1.3 Optical tweezers

In 1986 Ashkin succeeded in creating a stable optical trap from a single laser beam without relying on an external force such as gravity to cancel out the scattering force from the beam [4]. These single-beam optical gradient traps, or "optical tweezers", rely on focussing a Gaussian beam using a high numerical aperture (NA) lens. If the NA is high enough, then the component of the gradient force acting backwards along the beam axis will itself be enough to overcome the scattering force, hence creating an equilibrium position for the trapped particle. This is shown in figure 2.2.

Aside from the obvious advantage that optical tweezers can trap particles regardless of angle of incidence of the trapping beam while optical levitation traps must necessarily originate from below the trapped particle, optical tweezers also perform better in terms of stability. In a levitation trap the gravitational force acting to counteract the scattering force is on the order of $\approx mg$, where m is the mass of the particle and g is the acceleration due to gravity. In contrast, the counteracting gradient force in an optical tweezers trap can be thousands of times mg and is limited only by the optical power in the beam. This is particularly important when trapping microscopic particles in liquid, where the influence of gravity is negligible compared to that of Brownian motion [29].

2.2 The basic forces in optical tweezers

The optical force, F, on a particle of radius, r, and volume, V, exposed to an optical field is given by [30]

$$\langle F \rangle = r^2 \int_V \hat{r} \, \langle TM \rangle \, dV, \tag{2.2}$$

where $\langle TM \rangle$ is the Minkowski form of the Maxwell stress tensor, and $\hat{r}$ is the unit vector in the radial direction. The Minkowski form of the Maxwell stress tensor is defined as

$$\langle TM \rangle = \frac{1}{2} \Re(\epsilon_r \epsilon_0 E \otimes E^* + \mu_r \mu_0 H \otimes H^*) - \frac{1}{2} (\epsilon_r \epsilon_0 E \cdot E^* + \mu_r \mu_0 H \cdot H^*) I, \tag{2.3}$$

where $\otimes$ is the outer product, I is the unit tensor, E is the electric field, H is the magnetic field, ϵ_0 is the permittivity of free space, μ_0 is the permeability of free space, and ϵ_r and μ_r are the material's relative permittivity and relative permeability respectively. The Minkowski form of the Maxwell stress tensor is chosen as it takes into account the momentum carried by the particle. This is in contrast to the Abraham form, in which the momentum is viewed to be contained solely within the electromagnetic field [31]. This makes the Minkowski form more appropriate when calculating light-matter interactions.

The study of optical trapping is usually divided into various regimes, depending on the radius, r, of trapped particle relative to the wavelength, λ, of the trapping beam. Here it is useful to define the wavenumber, $k = \frac{2\pi n_m}{\lambda}$, where n_m is the refractive index of the surrounding medium. Trapping of particles that are large with respect to the wavelength ($kr \gg 1$) can be fully described using a ray-optical approximation whereby the particle refracts the incident beam. When particles are small compared to the wavelength ($kr \ll 1$) they are viewed as dipole oscillators (the dipole approximation). The optical trapping reported in this thesis took place in the intermediate regime (i.e. $kr \approx 1$), and yet understanding gleaned from both the ray optics and dipole approximations is still valid. For this reason both of these extreme cases are used in forming an intuitive understanding to the optical trapping problem.

By employing the Maxwell-Faraday equation, $\nabla \times E = i\omega\mu_0 H$, and knowing that the optical force given by the dipole approximation is:

$$\langle F \rangle = \frac{1}{2} \Re \left(\sum_i \alpha_p E_i(r) \nabla E_i^*(r) \right), \tag{2.4}$$

7

we can write that the force felt by the particle in an optical trap is given by [32]

$$\langle F \rangle = \frac{1}{4}\Re(\alpha_p)\nabla|E|^2 + \frac{\sigma(\alpha_p)}{2c}\Re(E \times H^*) + \sigma(\alpha_p)c\nabla \times (\frac{\epsilon_0}{4\omega i}E \times E^*), \tag{2.5}$$

where $\sigma(\alpha_p)$, the total particle cross-section, is defined as the sum of the scattering and absorption cross sections, i.e.

$$\sigma(\alpha_p) = \sigma_{sc}(\alpha_p) + \sigma_{abs}(\alpha_p), \tag{2.6}$$

where all cross-sections are a function of the particle's polarisability, α_p. The polarisability of a material can be viewed as a measure of how readily it will become polarised when exposed to external field, i.e.

$$p = \alpha_p E, \tag{2.7}$$

where p is the induced dipole in the material, and E is the externally applied electric field.

The first term in equation (2.5) represents the optical gradient force [33], [34], while the second and third terms are non-conservative forces collectively representing the optical scattering force. The second term is the radiation pressure force, which acts on the particle to push it along the direction defined by the Poynting vector, $\mathbf{S} = \frac{1}{\mu_0}E \times B^*$ [35], [36]. The third term, the spin curl force, arises from nonuniform distributions in a beam's helicity, and was only identified recently [32]. Before it was discovered, it was thought that the radiation pressure force was exclusively responsible for the optical scattering force. In most cases the spin curl force can be ignored, but it does have an appreciable effect in beams which are tightly focussed.

The key aspect to note from equation (2.5) is that all three factors depend upon the polarisability of the particle in question. The polarisability, α, of a material is a measure of how readily it will become polarised when exposed to an applied electric field, E. The gradient force, F_{grad}, scales linearly with the real part of the particle's polarisability thus

$$F_{grad} = \frac{1}{4}\Re(\alpha_p)\nabla\left\langle |E|^2 \right\rangle. \tag{2.8}$$

The polarisability for small dielectric particles is given by [37]:

$$\alpha_p = \frac{\alpha_0}{1 - i\alpha_0 k_0^3/6\pi\epsilon_0}, \tag{2.9}$$

where the definition of α_0 is given by the Clausius-Mossotti relation:

$$\alpha_0 = 4\pi n_{m,1}^2\epsilon_0 r^3 \left(\frac{m^2 - 1}{m^2 + 2}\right). \tag{2.10}$$

Here we can see that the polarisability of a particle is a function both of its size, and the ratio of the real part of its refractive index to the real part of the refractive index of the surrounding medium, i.e. $m = \frac{n_{p,1}}{n_{m,1}}$. Here we have noted that refractive index, n_p, is generally complex:

$$n_p^* = n_{p,1} + in_{p,2}, \tag{2.11}$$

having a real part, $n_{p,1}$, and an imaginary part, $n_{p,2}$. The imaginary part of the refractive index relates to the absorption cross section, and will influence how much the particle will heat up. This is not a significant effect in dielectric materials, and so for the remainder of this thesis we simply equate total refractive index with its real-part, i.e. $n_p = n_{p,1}$.

From equation (2.10), it would seem that simply increasing either the refractive index contrast of the particle or its radius would result in the particle being trapped more strongly. Of course in reality it is not this simple, as the scattering force is also dependant on the particle's polarisability.
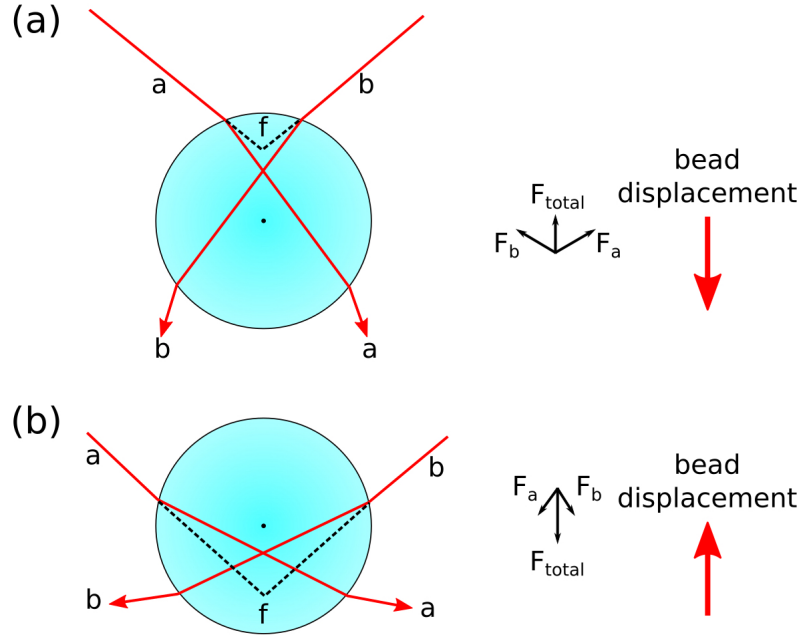
Figure 2.2: Ray-optics explanation of the forces in an optical tweezers trap. Particles with refractive indices greater than the surrounding medium act as positive lenses, bending the light that is incident upon. The light-rays are brought to focus at a point different from the default focal point, f, where they would have been focussed had the particle not been there (the default trajectory of the beams is shown by the dashed lines). The resultant change in momentum of the light is balanced by change in the momentum of the particle, giving rise to the gradient force. The top figure shows the case for a loosely focussed beam, while the bottom figure shows that for a tightly focussed beam. In the latter case the condition for a stable tweezers trap is met, namely the component of the gradient force acting backwards against the beam direction is larger than the forward scattering force.

As shown in equation (2.6), the cross section of the particle can be divided into the scattering cross section, σ_{sc}, and the absorption cross section σ_{abs}. The scattering cross section is proportional to the absolute square of the polarisability:

$$\sigma_{sc}(\alpha_p) = \frac{k^4}{6\pi\epsilon_0^2}|\alpha_p|^2 \tag{2.12}$$

while the absorption cross section is proportional to the imaginary component of the polarisability:

$$\sigma_{abs}(\alpha_p) = \frac{k}{\epsilon_0}\Im(\alpha_p). \tag{2.13}$$

The scattering cross section determines how much the particle will scatter incident light, with larger values being increasingly detrimental to the trapping ability of optical tweezers. The absorption cross section determines how much light the particle will absorb. Absorption can be a problem because the particle will locally heat the system, leading to instabilities linked to an increased Brownian motion in the sample. In this thesis typically only dielectrics (which have very low absorption cross sections) were trapped, meaning that heating of the sample was not usually a problem.

To understand how the optical force on a particle depends on the particle's refractive index we continue with the approximation that $n_p = n_{p,1}$. We note that the refractive index determines

the phase velocity of light passing through the material, and therefore determines the extent of refraction that incoming rays will undergo as they enter the particle. From figure 2.2 it is clear that a greater degree of refraction leads to a greater optical force on the particle. This can be demonstrated explicitly by considering the momentum of a photon as it passes from the surrounding medium into the particle. In the surrounding medium, each photon will carry a momentum, p_m, of

$$p_m = n_m \hbar k, \tag{2.14}$$

while in the particle its momentum will change to

$$p_p = n_p \hbar k, \tag{2.15}$$

where $\hbar$ is Planck's constant. Therefore each photon will impart a force onto the particle of:

$$F = \frac{\delta p}{\delta t} = \frac{\delta}{\delta t}(\hbar k n_p - \hbar k n_m) = \frac{\delta}{\delta t}\hbar k(\Delta n), \tag{2.16}$$

from which it is clear that an increase of the refractive index contrast between the particle and the surrounding medium, Δn, results in an increase in the optical force acting on the particle. This also explains why particles with refractive indices smaller than their surrounding medium (i.e. air bubbles in glycerine) are pushed away from the trapping beam; the sign of the optical force is negative for negative refractive index contrasts [38].

The dependence on refractive index contrast can also be demonstrated in the dipole regime. Reformulating equation (2.8) in terms of refractive indices, using the identities (2.9) and (2.10), gives:

$$F_{grad} \propto \left(\frac{m^2 - 1}{m^2 + 2}\right) = \Delta n \frac{n_p + n_m}{n_p^2 + 2n_m^2} \tag{2.17}$$

and for the scattering force:

$$F_{sc} \propto \left(\frac{m^2 - 1}{m^2 + 2}\right)^2 = (\Delta n)^2 \left(\frac{n_p + n_m}{n_p^2 + 2n_m^2}\right)^2, \tag{2.18}$$

where have assumed that the scattering force scales with reflectivity of the particle, which itself scales with $(\Delta n)^2$.

In this form it becomes clear that the scattering force increases much more rapidly than the gradient force does. So, even though it is true that increasing the refractive index of the particle leads to a greater gradient force, and in principle stronger trapping, the fact that the scattering force also depends on the refractive index places an upper limit on the refractive index of particles that can be trapped. Work has been done with particles which have been modified through the addition of an anti-reflection (AR) coating which greatly reduces their reflectivity and, hence, the scattering forces imparted on them by the light. With AR coatings one is able to trap particles with higher refractive than would otherwise be possible. This grants access to far higher gradient forces, and allows the trapping forces applied to the particles to reach into the range of several nN [21].

The other option when it comes to increasing the polarisability is to increase the size of the particle. If we take equation (2.8) and actually calculate the form of the gradient force for a particle of radius, r, we get:

$$F_{grad} = r^3 \pi n_m^2 \epsilon_0 \left(\frac{m^2 - 1}{m^2 + 2}\right) \nabla \left\langle |E|^2 \right\rangle. \tag{2.19}$$

While from equation (2.12) we can see that the scattering cross section of a particle depends on its radius via:

$$\sigma_{sc} = r^6 \frac{128\pi^5}{3\lambda^4} \left(\frac{m^2 - 1}{m^2 + 2}\right)^2. \tag{2.20}$$
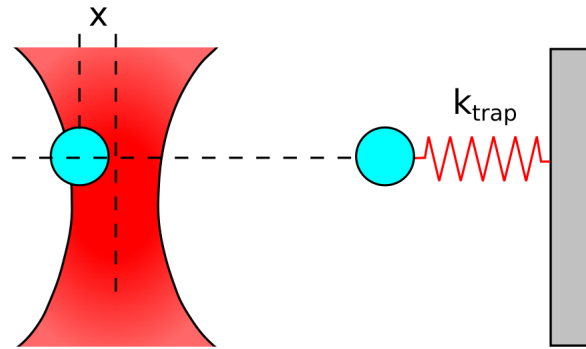
Figure 2.3: Equipartition model for particle trapped in an optical tweezers. The system is analogous to that of a mass on the end of a spring, attached to a immovable object. In both cases small deviations of the particle or mass are met by a linear Hookean restoring force. The natural frequency of the harmonic motion of the mass is determined by the spring constant of the spring. For the trapped particle it is determined by the trap stiffness of the optical trap.

From these relations it is clear that the scattering cross section increases much faster than the gradient force, putting an upper limit on the size of particle that can be trapped. The optimal trap stiffness will obtained when the particle being trapped is equal in size to the beam waist. As particles get larger, e.g. the size of a PM, the trapping beam no longer experiences a refractive index interface that has a curvature large enough to refract the light as shown in figure 2.2. As a result, the particle will not experience any significant gradient force, the scattering force will dominate the system, and the particle will simply be pushed through the sample by the laser.

2.3 Measuring the performance of an optical tweezers system

One would ideally wish for a trapped particle to remain perfectly still inside the optical trap, moving only as the trap does. In reality of course, this is not the case. The trapped particle is typically surrounded by a fluid of some description (normally water), and the molecules in this fluid move the trapped particle via Brownian motion. As a result, trapped particles will oscillate around the focal spot of the beam with a characteristic frequency. This is analogous to the case of a mass on a spring whereby the spring is "fixed" to the beam focus (see figure 2.3). For small displacements from the optical trap, x, the restoring force felt by the particle, F, obeys Hooke's law:

$$F = -k_{trap}x \tag{2.21}$$

where k_{trap} is the trap stiffness (in direct analogy to the spring constant of a mechanical spring).

By improving the quality of the optical traps, one increases the trap stiffness. This reduces the mean absolute displacement of the bead from the trap and increases the frequency of the oscillatory motion. There are several methods for measuring the trap stiffness of an optical tweezers system. Three of the most common of them are described below.

2.3.1 Equipartition theorem method

By considering the thermal fluctuations experienced by a trapped particle, one can infer the trap stiffness from the equipartition theorem [39]:

$$\frac{1}{2}k_b T = \frac{1}{2}k_{trap}\left\langle x^2 \right\rangle, \tag{2.22}$$

where k_{trap} is the trap stiffness of the trap, k_B is Boltzmann's constant, $\left\langle x^2 \right\rangle$ is the variance of the particle's position, and T is the temperature of the system. By rearranging equation (2.22)), one gets an expression for the trap stiffness:

$$k_{trap} = \frac{k_B T}{\left\langle x^2 \right\rangle}. \tag{2.23}$$

The equipartition theorem method is straightforward to implement, and is advantageous in that it can be employed without knowledge of the size or shape of the trapped particle, or the viscosity of the surrounding medium. One particular limitation of the technique is that it relies on the variance of the particle position, which is an intrinsically biased indicator. Any noise or drift in position measurements become positive when squared, which results in an overestimation of the variance, and a subsequent underestimation of the trap stiffness.

2.3.2 Power spectrum method

The one-sided power spectrum for a trapped sphere describes the characteristics of the particle by expressing the power in the system in terms of the frequencies present in the particle's motion. At the certain frequency, known as the "corner frequency", the power spectrum drops off linearly, and as a result it can be fitted well to a Lorentzian [40], [41] defined by:

$$S(f) = \frac{k_b T}{\pi^2 \beta (f_0^2 f^2)}, \tag{2.24}$$

where β is the hydrodynamic drag coefficient for the particle, and f_0 is the roll-off frequency.

For a spherical particle of radius, a, in a medium with a viscosity, η, the drag coefficient is given by the Stokes relation:

$$\beta = 6\pi\eta a. \tag{2.25}$$

The trap stiffness can be calculated from the roll-off frequency and drag coefficient via:

$$k_{trap} = 2\pi\beta f_0. \tag{2.26}$$

In order to calculate the trap stiffness one must ensure that the detector has sufficient bandwidth to fully capture the power spectrum of the particle well pass the roll-off frequency. If sufficient bandwidth is not used, low-pass filtering of the spectrum can occur which leads to an underestimated value for the roll-off frequency. Power spectra measured in this thesis were captured by taking high-speed video recordings ($\approx 1000\,\text{Hz}$) of the trapped particles.

2.3.3 Drag force method

Finally, there is the drag force method, which is perhaps the most direct method with which to measure the trap stiffness. Here a particle is trapped and the sample stage is moved at a known speed, imparting a drag force on the particle. As long as the drag coefficient for the particle is known one is able to extract the trap stiffness by equating the drag force and restoring force of the trap. Arranged in terms of trap stiffness, k_{trap}, this gives:

$$k_{trap} = \frac{1}{2}\frac{\rho v^2 \beta A}{x}, \tag{2.27}$$

where ρ is the density of the medium, and A is the projected surface area of the particle along the direction of travel.

2.4 Beam shaping for optical manipulation

The basic form of optical tweezers can be improved upon via some form of beam shaping. This allows optical traps to be moved around inside the sample, or for several traps to be generated from a single beam, or both. Beam shaping also allows one to move away from the optical tweezers scheme entirely, through the use of exotic beams, for example. This can have many advantages, although of course these come with unique limitations. Ultimately, the form of optical manipulation chosen is the one that best addresses the challenges being faced.

This section will explore the role that beam-shaping has had in the field of optical manipulation. Its impact on optical tweezers is addressed first, followed by a discussion on some of the more exotic optical manipulation schemes available.

2.4.1 Generating many tweezers traps and making them steerable

Using a simple optical tweezers system, one has a single, stationary, trap in the plane of the sample. One can trap an object and then move the sample around the trap via the use of a steerable stage, however this sort of manipulation is rather limited in scope. The first fundamental improvement to optical tweezers systems was to make them steerable.

This is achieved by Fourier engineering the transverse light distribution of the laser in the back focal plane (BFP) of the objective lens. The light-field in this plane undergoes a Fourier transform as it is focussed by the lens into the sample-plane, i.e the BFP of the objective and the sample plane are Fourier transform pairs. By understanding this relationship between the light in these two planes one can alter the light-field in the BFP of the objective such that the form of resultant light-field in the sample plane is desirable to the user. In reality it is very difficult to physically access the BFP of the objective lens, and so instead a relay telescope is used to form a plane which is conjugate to the objective lens' BFP. It is in this plane that the transverse structure of the beam is Fourier engineered.

By placing a steerable mirror in this Fourier plane one can alter the k-vectors of the ray-bundles leaving the plane simply by tilting the mirror. The spot that these ray bundles form as they are focussed by the objective lens will lie on the image plane, but are offset laterally from the optical axis. The greater the tilt in the mirror, the greater the change in the k-vector of the ray bundle and, hence, the greater the offset in the trap's position. In most cases a pair of steerable mirrors are used, controlled via a galvanometer, with each mirror being responsible for a single axis of rotation [42].

Similarly, acousto-optic modulator (AOM)s can also be used to influence the light-field in the Fourier plane. Acousto-optic modulators are typically made from a piece of quartz with a piezoelectric transducer attached to their side. The piezoelectric transducer causes the quartz to vibrate, which sets up a standing wave pattern across it. This standing wave pattern alters the density, and hence the refractive index, of the quartz periodically across its lateral aspect, effectively making it a diffraction grating. The system is aligned such that the first order diffracted beam reaches the objective lens and hence the sample. By altering the frequency of the vibration one can determine the pitch in the resultant grating. This has the effect of changing the angle of the first diffracted order, which is equivalent to the case of the steering mirror. The major advantage that AOMs have over steering mirrors is the speed with which they can be updated [43]. By switching quickly between two or more different grating patterns, an AOM can "share" light between various positions, effectively generating multiple tweezers traps from a single beam. This "time-sharing" approach to creating multiple traps is fine for AOMs, where switching times are greater than the time taken for a particle to diffuse away from a trap, but are not valid for slower modulation methods.

Finally, the Fourier plane can be influenced "holographically", typically through the use of a spatial light modulator (SLM). A thorough discussion of the structure and operation of SLMs is left for chapter 4, but for the time being it is sufficient to view a SLM as a small, pixellated, device capable of generating distinct phase delays in each of its pixels. The SLM as a whole is then able to impart near-arbitrary phase delays across the transverse aspect of incident light-beams. Using a SLM, one is able to generate a large number of tweezers traps, and address each one individually. The pattern which is displayed on a SLM can be updated at video frame rates, allowing the distribution of traps to be altered in real-time.

Despite having slower response times than AOMs, SLMs are widely used because of their unparalleled versatility which can allow extremely complex optical distributions to be formed. When highly-precise, feedback-based, optical trapping is required AOMs find more use.

2.4.2 Optical manipulation using "exotic" beams

2.4.2.1 Angular momentum

In addition to linear momentum, light can also carry angular momentum which it can impart to particles. Angular momentum is split into two distinct types: orbital angular momentum (OAM) and spin angular momentum (SAM). Spin angular momentum is associated with the polarisation state of the light. For example, a circularly polarised beam carries a SAM or $\hbar$ per photon. In contrast, OAM is associated with beams that have helical phase fronts, with the Laguerre-Gaussian (LG) mode set representing a perfect basis for OAM. LG beams have azimuthal phase structures, $e^{i\phi}$, meaning that their Poynting vectors have non-zero azimuthal components at all points along the beam radius, r, where ϕ is the azimuthal angle. Unlike with SAM, LG beams carry $l\hbar$ OAM per photon, where l is the mode number. An interesting consequence of the phase ambiguity at the centre of beam is that the light intensity there is zero. This gives LG beams a characteristic "donut" shape. LG beams are typically generated via modulating a Gaussian beam using a forked diffraction grating, displayed on some form of diffractive optical element. The forked grating generates a phase singularity in the the centre of the beam which cancels out the amplitude in the centre of beam, hence the donut-shaped intensity profile of the beam.

Both kinds of angular momentum can be imparted to particles through various mechanisms such as birefringence, absorption, and scattering [44], [45], with induced rotation rates of particles reaching several hundred Hz in water [46] and 5 MHz in vacuum [47]. This has enabled fundamental investigations into the nature of angular momentum, [48] as well as applied work in the field of microfluidics and biophotonics. These include the use of a rotating microparticle as a probe to measure the local viscosity of a medium via the rotational Stoke's drag [49], [50]. Such sensors can perform over a large dynamic range (in excess of 2 orders of magnitude). Additionally, a distribution of such LG beams can be used to make a series of micropumps that can drive fluid flow in a microfluidic channel. Particles with refractive indices that are lower than the surrounding medium can be isolated in the central dark region of a LG beam, which has been proposed as a means of manipulating and mixing microdroplets [51].

Some investigations in to the polarisation of the light used in trapping has been explored, particularly in regards to its affect on both radial and axial trap stiffnesses. It has been found [52] that for radially polarised light, the axial trap stiffness increases with respect to plain polarised light, and at the same time there is a reduction in the lateral trap stiffness. It is clear then that there is relationship between the trap stiffness and the polarisation of the trapping beam.

2.4.2.2   Non-diffracting beams

Beam shaping is also used to form so-called "non-diffracting" beams. These beams are of interest as they can travel for long distances without changing shape, and can "heal" themselves if they are disturbed in some way (e.g. passing through a scattering medium) by re-establishing their original form. The most simple non-diffracting beam is an ideal, infinite plane wave. This meets the condition for non-diffraction that its wavevector in the direction of propagation must remain unchanged with time. Because ideal plane waves are not realisable, and are necessarily limited in size, this condition is only approximately met for real "plane waves".

Indeed, all beams which we might have an interest in studying are finite in extent, and as a result they must be composed of a sum of many spatial frequencies. The fact that each component frequency travels with a different speed in dispersive media would seem to suggest that diffraction is unavoidable. While this is true in a strict sense, it is possible to make beams which diffract very little, which we call "non-diffracting" beams. This is accomplished by considering the k-vectors of all the waves which make up the beam. Specifically, a beam is classed as non-diffracting if the components along the propagation direction of each of the constituent waves' k-vectors are equal [53]. This is the case for several families of beam, most notably Bessel beams, Airy beams, and Mathieu beams [53]–[55].

Because these beams persist over long length scales, they are useful for long range "optical guiding". Here a particle is confined inside the beam due to a lateral gradient force and pushed, or guided, along the beam by the scattering force. This effect is particularly striking in Airy beams, which propagate along curved paths. In these instances so-called "optical snowblowing" [56] has been used to move particles between adjacent microfluidic chambers by "blowing" them over the chamber walls [57]. Mathieu beams have been used to make light moulds for microscopic structures [58]. Extended particle "conveyor belts" have also been demonstrated, formed from Bessel beams [59], which can transport particles over several mm. Bessel beams have also been useful in the study of optical binding phenomena [60]. Optical binding provides a pathway to forming 2- and 3-dimensional, crystalline arrangements of particles known as "optically-bound matter". The behaviour of these optical lattices has revealed much about the behaviour of natural crystals, with fundamental phenomena such as laser-induced freezing and melting having been observed [61], [62].

2.5   Manipulation of novel geometries

Since Ashkin's original work on the trapping of spherical beads, there has been growing interest in the manipulation of more complicated structures, many of which have been designed to perform particular functions. This is of particular interest to the field of microrobotics, in which the ability to fabricate structures at the microscopic scale has lead to an explosion in new applications [63] Examples include micropumps, either in the form of spherical particles or more complex "motor" designs, which can drive fluid-flow in microfluidic environments [64]–[70]. These microscopic tools can also be used to probe the microrheological properties of the surrounding medium [71]–[74]. Microscopic grippers and levers can provide intuitive means of particle manipulation and can also serve to amplify the the weak optical forces at work.

Microrobotics relies upon control over two key aspects: microfabrication and micromanipulation. In both of these regards light can play an important role.

2.5.1   Microfabrication

Direct-write techniques can define three-dimenisional structures by using a pulsed laser to write the features in the host material [75]. Similarly, two-photon polymerisation (2PP) has been used to define

structures beyond the diffraction limit of light [76]–[78], as has light-suppressed polymerisation [79]–[81].

These techniques are able to define complicated structures, although reproducibility can be an issue when the complexity of the design is too great. Additionally, because they are all scanning techniques, fabrication times can be long. However, recent speed gains of several orders of magnitude have been achieved by using several beams working in tandem [82]–[84], giving beam speeds of up to $550\,\mathrm{mm\,s^{-1}}$ [85].

The fabrication procedure outlined in this thesis, which is discussed further in chapter 3 is to use nanolithography. Nanolithographic procedures, like those developed in the silicon photonics industry, are complementary to the direct-writing techniques outlined above. In general nanophotonic techniques have better resolution due to the fact that sample writing is done with electrons rather than photons. These electrons have DeBroglie wavelengths far smaller than optical wavelengths. There are several factors which mean that limit represented by the DeBroglie limit is not reached in practice, but the sample writing with an electron beam can still reach resolutions of $\approx 50\,\mathrm{nm}$. They are also capable of higher throughputs. Once a write has been set up it is entirely automated, and will typically be set to run overnight. During this time (typically $15\,\mathrm{h}$) in excess of 150,000 structures can be defined. One major advantage to the direct-writing approach is that one can make truly 3-D features, whereas nanolithography is inherently 2-D. Choice of technique is ultimately dependant upon what aspects of the design are most important to the user. Direct-writing can create novel 3-D structures, while nanolithography can produce higher precision, 2-D structures.

Due to scaling laws, often a microscopic tool is not simply a scaled-down version of its macroscopic self. Microtool design is a very active field at the moment, with some of the best designs either taking inspiration from biology [86] or taking the basic feature of the tool and simplifying it as much as possible [87]. Fields such as topological optimisation (used frequently in engineering) are seeing increased usage in this area, often producing designs which are somewhat counter-intuitive [88].

2.5.2 Micromanipulation: structure-mediated design

Spherical particles are the most common object manipulated by optical tweezers. Spheres represent the simplest geometry in terms of behaviour in an optical trap, because of their perfect rotational symmetry. As one moves away from a spherical geometry, anisotropy in the design demands a more complicated description of the object's reaction to an optical trap. Figure 2.4 shows the rule-of-thumb behaviour for three distinct "families" of trapped structures, namely spheres, cylinders, and membranes. In general, extended structures such as cylinders and membranes will reorientate themselves within the trap to align their longest axes along the beam axis. This realignment is in response to their increased polarisability along the long axis (there is more material in that direction), with the orientations shown in figure 2.4 representing the lowest-energy states for the structures.

Although it is possible in some cases to trap non-spherical microscopic objects, one does not have access to fully arbitrary translational and orientational positioning in 3-D space (six-degree-of-freedom (6DOF) control). The most common way to circumvent this issue is through structure-mediated design. This involves adding features to the microscopic object of interest that act as "handles" for optical tweezers. These handles are typically spherical in shape (polystyrene or silica beads being common choices), which makes them amenable to optical tweezers. They can be adhered to the target that one wants to trap, or, in the case of microfabricated samples, integrated into the design itself. Figure 2.5 highlights a few examples of this sort of structure-mediated design.

Spherical beads have ben incorporated into the design of many microfludic structures, with one of the more notable examples being demonstrated by Oeherlein et al., in which they tethered silicon beads to planar silica structures [90]. The extreme aspect ratios of the silica structure makes it effectively impossible to trap directly, yet through the addition of the silicon bead "handles"
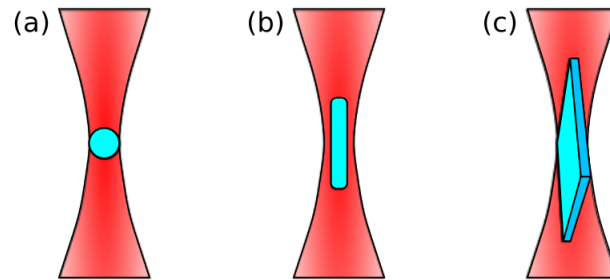
Figure 2.4: Default orientations for three trapped objects in the ray-optics regime. (a) The behaviour of spherical particles is well understood, their rotational symmetry making all orientation degenerate. (b - c) Extended objects will re-orient themselves to align their longest axis along the beam axis. This is the case for (b) rods and (c) membranes.
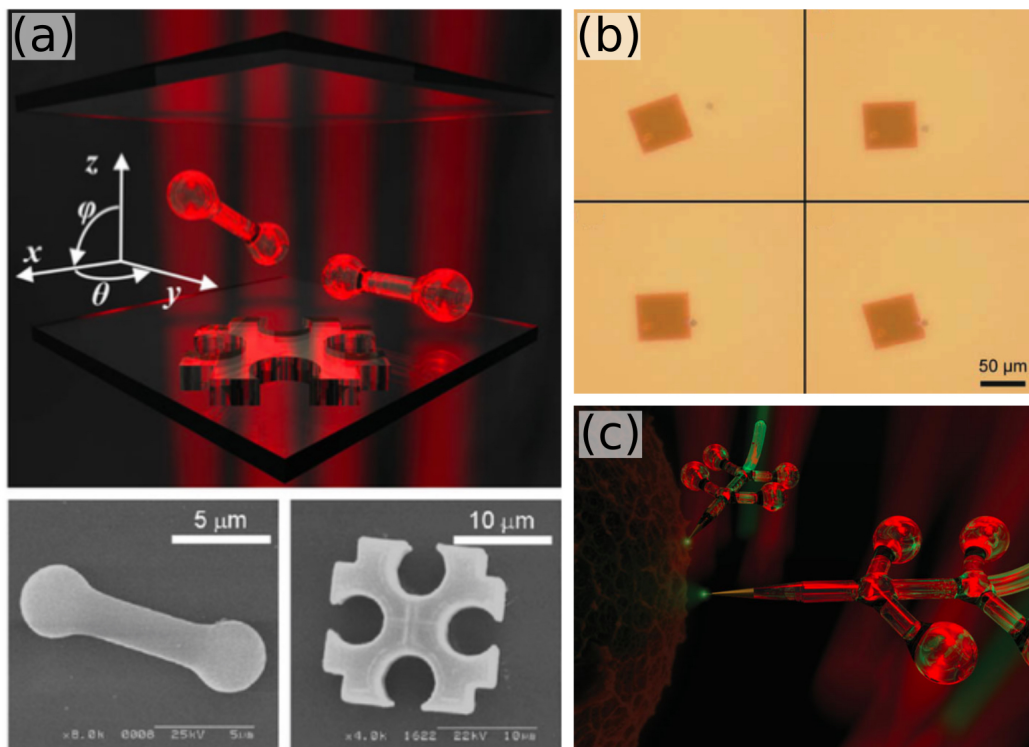

Figure 2.5: Optical manipulation through structure-mediated design. (a) Spherical features incorporated in shape-complementary objects which can be assembled using optical tweezers. Reproduced, with permission, from [89]. (b) A series of stills, reproduced, with permission, from [90], showing a silicon membrane being transported through a microfluidic environment using optical tweezers. (c) Artist's impression of optically actuated waveguide sensors, reproduced, with permission, from [91].

manipulation is made possible. This configuration of a structure tethered to a bead is known as an "optical trailer hitch". Using this scheme it is possible to translate the planar structure and rotate it about the beam axis, yet access to out-of-plane rotations is limited.

Spherical handles can also be defined in the design of microscopic structures themselves. Optical probes with handles have been trapped and used for scanning probe microscopy (SPM) [92]–[95]. These probes are brought toward the object of interest and scanned along its surface, with the surface's profile being discerned from the movements of the trapped handles. One advantage that these probes have is their ability to extract the surface profile from the sides of objects rather than only being able to access the top surface, as is the case with more traditional SPM methods.

Similar structures, made using 2PP, have been demonstrated that act as waveguides which focus the light at the end of the (tapered) waveguide [96]. These waveguides can be controlled with 6DOF control, and the waveguides allow low NA light to be coupled into them and converted to high NA light at the output facet. Because the waveguides can be positioned almost arbitrarily they can be used to deliver and collect light from target cells over a wide range of angles.

Light-driven microtools that were capable of performing a "syringe action" have recently been demonstrated which were defined via 2PP and controlled via counter-propagating beams [97]. Four of these beams are focussed onto the four spherical handles that are bound to the device, while another beam, use for heating, is directed into a hole in the top of the structures. By heating and cooling the fluid inside the device, small particles in the sample can either be drawn into, or expelled from, the device via a syringe-like protuberance at the front of the structure through the expansion and contraction of the fluid.

Optical assembly of structure-mediated devices has also been demonstrated. Banas et al. showed that it is possible to trap a number of structures that have complimentary shapes and to assemble them in a jigsaw fashion [98]. This paradigm circumvents some of the issues surrounding some of the complex fabrication procedures in nano-fabrication. It also extends the applicability of optical manipulation into optical assembly - a necessary capability if true microrobotics is to be realised.

2.5.3 Manipulation of photonic membranes

This thesis is concerned with the manipulation and application of photonic membranes - thin, robust membranes capable to supporting plasmonic features [99]. These PM can be made with a range of thicknesses and lateral aspects, but for the sake of this thesis we focus on PM that are 90 nm in thickness and 20 μm in side length. These dimensions give the PM an aspect ratio of over 200, placing them firmly in the category of planar structures.

When they are used to support nanoplasmonic features, PM can be considered to be flexible metasurfaces - the 2-D equivalent of a metamaterial [23]. Just as a traditional material is composed of atoms, a MM is composed of meta-atoms [100], [101]. However, where a material gains it properties from the specific atoms it is made from (i.e the chemical element), this is not such an important requirement of MMs. Rather, it is the size, shape, and periodicity of the meta-atoms which ultimately define the behaviour of the MM. Whatever form of meta-atom is used, they must be distributed in a sub-wavelength, periodic array. The result is that the light does not "see" the periodicity of the MM, but rather it discerns a uniform material with "effective" properties [102], [103]. A crucial aspect of MMs is that they can exhibit properties not found in nature. This has lead to applications in cloaking, negative refractive index, and epsilon-near-zero materials. The MS simply takes this same behaviour and confines it to a single 2-D surface.

The advantage of a MS is that it occupies far less space than a MM, and its reduced bulk allows it to be manoeuvred more easily. It planar structure also lends itself to established fabricational procedures, particularly those used by the silicon photonics industry. Using such techniques MS have been demonstrated to act as filters [104], axicons and lenses [22], sensors [105], and can even
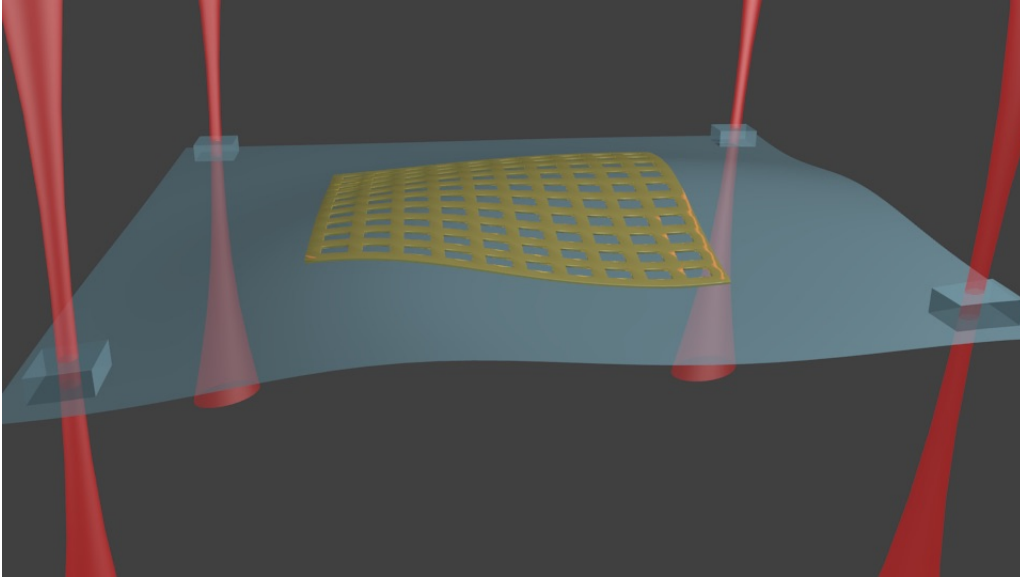
Figure 2.6: Artist's impression showing what it would be like to trap a membrane via handles patterned on each of the four corners. The photonic membrane has been patterned with a gold fishnet, allowing it to be used in microfluidic sensing applications.

create interfaces that override Snell's law [106]. For the most part MS are rigid, but their utility can be further extended if they can instead be defined on a flexible substrate, as is the case with PM.

Plasmonic effects are inherently short range, therefore to maximise the functionality of a MS it must be placed as close as possible to the object of interest. Because most objects are non-planar, it is extremely difficult to insure good contact using a rigid MS. The flexibility of PM allows it to circumvent this problem, as it can wrapped around the object, ensuring excellent contact. This gives greater contact between the two and maximises the utility of the PM, effectively by "dressing" the object with the photonic response of the PM.

The transferral of a PM's photonic response has been demonstrated in the case of an optical fibre [107]. Here a PM filter was wrapped around the end facet of the fibre, and successfully filtered the fibre's output. The PM could easily be removed and reapplied, and was robust enough to resist degradation. This is in stark contrast to the more traditional means of functionalising the end facet of a fibre, i.e. direct-writing. Direct-writing of an optical fibre is challenging, and any functionalisation is effectively permanent. Removing the photonic function means cleaving the fibre; an inherently destructive, wasteful, and non-reversible process. The application of PM to SERS is discussed in chapter 6, whereby a PM, patterned with a gold fishnet structure, is used to build a 2-D map of the chemical content of an undulating surface.

Both of the applications outlined above have been performed at the macroscopic scale, where positioning the PM by hand is sufficiently precise. In order to produce similar applications in a microfluidic environment, one needs to be able to position PM with far higher degrees of accuracy. It is with this requirement in mind that we explore optical tweezers as a means of manipulating photonic membranes.

2.6 Summary

The theory surrounding optical tweezers is well understood in the cases where simple objects such as spheres and rods are manipulated. The optical forces acting on a particle are known to depend upon on both the material properties of the particle and the optical properties of the beam. The picture becomes more complicated when one attempts to manipulate more exotic structures such as membranes, or microtools. To date, the most successful method to circumvent these issues is through the use of structure-mediated design. This involves fixing handle-like structures (usually spherical particles) to the target object, and trapping them instead. In this way one can achieve 6DOF control over structures and objects which could not be trapped directly.

The ability to manipulate these structures opens the door to the trapping of microscopic tools, including PMs. PMs have been used in a number of sensor and filtering applications at the macroscale, and yet have not been deployed into a microfluidic environment due to their strict manipulation requirements. The ability to optically manipulate PMs opens them up to new applications, most notably biophotonic applications such as *in vitro* SERS or filtering.

Fabrication

This chapter outlines the fabrication protocol that I developed to realise the photonic membranes. Considering the full spectrum of photonic membranes made in this thesis, thicknesses range from 90 nm to 1 µm, with lateral aspects ranging from 20 µm. Modifications can be made to the design of these devices to increase flexibility or stability, as desired.

The outline of this chapter starts with an overview of the fabrication procedure used, before going process by process and exploring the various aspects of the procedure in more depth. Complete recipes are provided for all the devices discussed here. The fabrication of substrates used for surface-enhanced Raman spectroscopy will also be covered, both in their rigid and flexible forms.

3.1 Overview

The fabrication protocol outlined in this thesis is a top-down process that utilises the tools and techniques typical of the silicon nanophotonics industry. Through this procedure a number of layers are applied to the sample, from which unwanted material is stripped away though various processing steps. An overview of the fabrication protocol is shown in figure 3.1.

Fabrication begins with a silicon wafer substrate, cleaned using acetone and propan-2-ol (IPA) (fig. 3.1(a)). A sacrificial layer (fig. 3.1(b)) and a membrane layer (fig. 3.1(c)) are spin-coated on top, baked, and patterned by ultra-violet (UV) or electron beam lithography (EBL). Non-patterned areas are removed through chemical development (fig. 3.1(d)). Another layer can be applied and patterned to define handles for optical manipulation, if desired (fig. 3.1(g)). If plasmonic features are called upon by the design, then gold can be evaporated onto the device and patterned through a combination of EBL and reactive ion etching (RIE) (fig. 3.1(e)).

Once the photonic membrane has been defined, it remains only to remove it from the substrate. This is achieved by submerging the sample into the appropriate lift-off solvent (fig. 3.1(h)). The photonic membranes can either be mounted onto a frame for applications where they will be manipulated by hand, or they can remain in solution with a view to using them in a microfluidic environment.

All the fabrication steps outlined were performed in a class 10,000 cleanroom, with spin-coating and development steps being carried out in class 1,000 wetdecks. The class of a given environment is equal to the number of particles under 0.5 µm in diameter, found in a cubic foot of air. A generic environment, such as an office space, typically "operates" in excess of class 10,000,000. Low particle counts are a must for this type of precise nanofabrication.
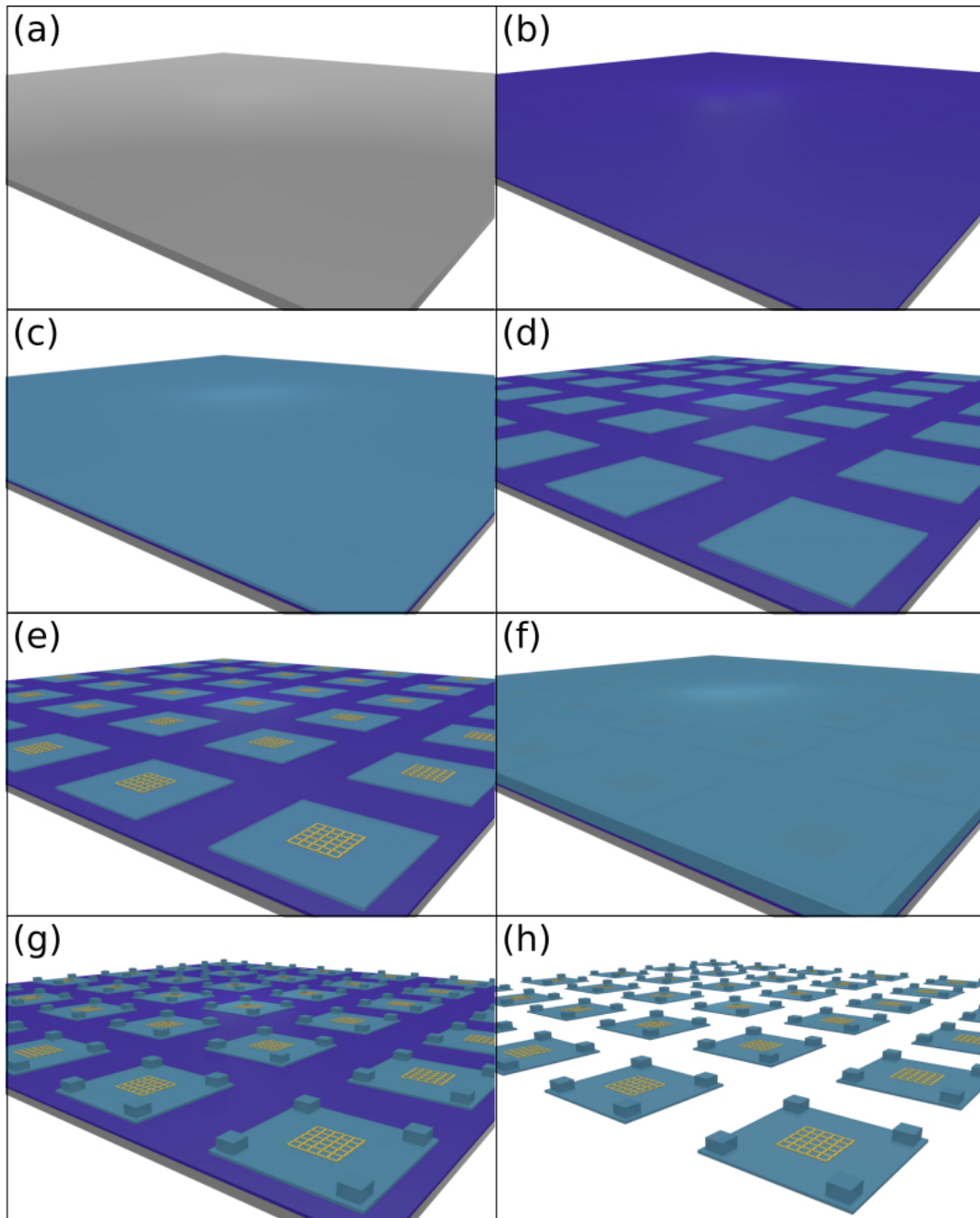
Figure 3.1: Overview of the fabrication steps discussed in this chapter. For demonstration purposes the example of a photonic membrane, hosting plasmonics, used in a microfluidic environment is shown. (a) A silicon substrate is spin-coated with (b) Omnicoat, and (c) SU-8, thickness 90 nm. (d) This layer is patterned via EBL, and developed chemically. (e) Gold is evaporated onto the sample, SU-8 is spin-coated on top, and the sample is patterned, developed, and etched via RIE. (f) A thicker SU-8 layer is spin-coated onto the sample, before (g) it is patterned via EBL and developed to reveal handle structures. (h) Finally, the sacrificial layer of Omnicoat is removed and the membranes are left freely suspended.

3.2 Substrates

Either glass or silicon were used as substrates, depending on the application. In the framework of our application, both materials can be considered as perfectly flat. Silicon has the advantage that its superior electrical conductivity prevents it from charging to the same extent that glass does during EBL, making the process easier. Its lattice-like structure is also advantageous. Whereas silicon will give a very straight edge when it is cleaved, glass, with its amorphous crystal structure, will typically produce a less tidy edge when it is cut. Aside from it being cheaper, the only advantage that glass has over silicon is that it is transparent in the optical region of the electromagnetic (EM) spectrum. For this reason, glass was chosen when rigid substrates, used for surface-enhanced Raman spectroscopy, were being made. Transparency was a critical property in this case as the substrates were directly incorporated into an optical microscope. For all other applications silicon (supplied by Soitec) was used as the substrate.

Before a substrate can be used it must first be cleaved to a manageable size, usually a square 2 cm in length. Silicon can be cleaved very easily. A diamond-tipped scribe or a LatticeAx 220 cleaver (LatticeGear) are used to make a small indentation in its surface that, as close as possible, runs along its lattice direction. This introduces a structural weakness into the substrate. By applying firm pressure to both sides of this indentation the silicon breaks in two, leaving an extremely fine edge. Glass does not have a regular lattice-like structure and therefore it cannot be "cleaved" in the strictest sense of the word. Instead, a diamond-tipped glass cutter is used in conjunction with a ruler. A single score is made in the glass (repeated scoring only makes it less likely that the glass will break along a straight line), and the glass is placed on an elevated surface with the score overhanging the edge. A single downward blow with a finger is enough to cause the glass to snap along the score, and has been found to be the most reliable way to form a relatively clean edge. In the case of glass substrates, coverslips were used (Agar Scientific, thickness no. 0 - part number L46S24-0).

Whether glass or silicon is chosen, the substrate needs to be cleaned before it can be used. Because fabrication occurs at the nanoscale, the presence of dust has severely affects the uniformity of the subsequent membrane layers. To clean the substrates, they are immersed first in acetone for 2 min, and then in IPA for 2 min. In each case they are exposed to an ultrasonic bath. Acetone is a good organic solvent which dissolves any of the typical contaminants found on the substrate. This action is aided by the ultrasonic bath which acts to dislodge dust and dirt from the substrate's surface. Upon removal from acetone, one must be careful to ensure that the acetone does not simply evaporate from the surface of the substrate, re-depositing the particulates which were dissolved in the acetone back onto the substrate. To avoid this the sample is moved quickly from the acetone to the IPA. IPA dilutes any remaining contaminants, and keeps them in solution longer than acetone does, due to its higher boiling point. This latter point is important, as it gives one more time to perform the final step in the cleaning process: drying with a nitrogen gun. This involves removing the sample from the IPA and placing it on an absorbent cleanroom towel. From here, it is pressed gently into the towel such that it wont easily blow away, and a nitrogen gun is brought in from above. Nitrogen is blown onto the sample for about twenty seconds, making sure that any remnants of IPA are removed from the substrate's surface without evaporating.

3.3 Membrane deposition and definition

3.3.1 Spin-coating

The sacrificial and membrane layers are deposited onto the substrate via spin-coating. Spin-coating works by pipetting a few drops of a chosen polymer onto the substrate, and then spinning the substrate at high speed. The interplay between the centrifugal force and the surface tension of the polymer defines the thickness of the layer, which can be tuned by altering the spin speed. The

Membrane parameters			
Function	Solution	Spin Speed	Thickness
Sacrificial layer	Omnicoat	1000 rpm	20 nm
Microfluidic membranes	SU-8 2000.5:Cyclopentanone 1:2	5000 rpm	90 nm
Handles	SU-8 2000.5:SU-8 2050 3:1	3000 rpm	1.5 μm
Flexible SERS substrates	SU-8 2000.5:SU-8 2050 1:1	5000 rpm	4 μm

Table 3.1: The various membranes defined throughout this thesis, their parameters, and the specific function they performed.

technique is highly repeatable, and creates optically flat layers. After spinning the sample is baked to evaporate the solvent that that polymer is dissolved in, making the layer solid. Spins lasted 1 min, with an acceleration and deceleration of $50 \, \mathrm{rpm \, s^{-1}}$ on either side of this.

The first layer to be spin-coated (with the exception of rigid SERS substrates) is the sacrificial layer of Omnicoat (supplied by MicroChem). A spin speed of 1000 rpm is used, giving a layer thickness of approximately 20 nm. The Omnicoat is then baked at 230 °C for 1 min. SU-8 (also from MicroChem) is then spun on top, at a speed dictated by the desired thickness [108]. It is then baked at 100 °C for 5 min, although the temperature is ramped up from 65 °C to 100 °C over the first minute to prevent bubbles from forming in the SU-8.

Two different viscosities of SU-8 were used: SU-8 2000.5 and SU-8 2050. When spun at 3000 rpm these give layer thicknesses of 0.5 μm and 50 μm, respectively. By combining these two viscosities in various ratios, it is possible to create a SU-8 mixture that spins to any thickness between these two extremes. Additionally, if SU-8 2000.5 is diluted with cyclopentanone it can be spun at thicknesses below 0.5 μm. Table 3.1 shows a list of membrane thicknesses and recipes used in this thesis, determined through the use of a Dektak surface profilometer (Veeco).

SU-8 is chosen to form the membrane layer because it is optically transparent and mechanically robust, having a Young's modulus of 2.9 GPa to 3.5 GPa depending on the specific baking parameters used [109], [110]. Mechanical robustness is important, as the membranes must be strong enough to support their own weight once they are made thin and flexible. SU-8 is also a negative-tone photoresist [111], [112], meaning that area of it which are exposed to UV lithography or EBL become cross-linked and resistant to chemical development. This makes multi-layered structures, such as photonic membranes with handles, easier to fabricate as lithography runs no risk of influencing the previous membrane layers through accidental exposure. Additionally, SU-8 is biocompatible, making a suitable material on which to make *in vivo* sensors [113].

3.3.2 Membrane definition

Photonic membranes are defined through either UV lithography or EBL. Regardless of which technique is used, the energy introduced into the SU-8 is enough to trigger a cross-linking process. This causes the areas of SU-8 that are exposed to polymerise, with this polymerisation being further enhanced by a subsequent post-exposure bake.

Typically UV lithography is used when larger membranes, some cm in side-length, are desired. Under these circumstances the sample is loaded into a UV mask-aligner and exposed for 2 min, after which it is unloaded, and baked at 200 °C for 2 min. Patterning the membrane through EBL is more involved, but can produce excellent results, particularly when it comes to defining the photonic membranes used for optical trapping. Most of the membranes discussed here were made via EBL and so this technique is outlined in more detail below.

Electron beam lithography parameters		
	Area	Line
Basic SU-8 dose SERS	$10\,\mu A\,s\,cm^{-2}$	$12\,\mu A\,s\,cm^{-1}$
Basic SU-8 dose Membranes	$3.5\,\mu A\,s\,cm^{-2}$	n/a
Basic SU-8 dose Handles	$3.75\,\mu A\,s\,cm^{-2}$	n/a
Gun voltage	30 kV	
Aperture size	$10\,\mu m$	
Working distance	10 mm	
Write field size	$100\,\mu m \times 100\,\mu m$	
Basic step size	5 nm	
Area step size	20 nm	
Settling time	auto	

Table 3.2: Typical EBL parameters used for the various SU-8 features.

3.3.2.1 Electron beam lithography: General principles

EBL works by scanning a stream of electrons across a sample. For negative-tone resists like SU-8, the electrons "write" a pattern in the sample by cross-linking the areas they interact with. The extent of this cross-linking is dependent on dose, D, delivered to the area, defined as

$$D = \frac{IT}{A} \tag{3.1}$$

where I is the beam current, T is the dwell time, and A is the area being exposed. The doses used are dependent on the process, and can either be applied to areas of the sample or along lines. Typical values used in this thesis are listed in table 3.2.

The resolution of this technique depends on the aperture size and gun voltage used, and is on the order of 20 nm [114] for the values shown in table 3.2. Resolution is also affected by the thickness of the sample one wants to pattern. This is because the electrons undergo small scattering events (known as forward scattering) which broaden the beam. The increase in the beam diameter, d_f, measured in nm, due to forward scattering is given by

$$d_f = 0.9 \left(\frac{R_t}{V_b} \right)^{1.5} \tag{3.2}$$

where R_t is the thickness of the resist, in nm, and V_b is the beam voltage. Although forward scattering is usually seen as a limit to EBL resolution [115], if harnessed correctly it can be advantageous to certain designs [116].

Figure 3.2(a) shows a typical Monte Carlo simulation of an electron scattering in EBL. The beam broadens with a characteristic "plume" shape, reducing the resolution [117]. Additionally, the beam undergoes backscattering from the substrate, leading to a further decrease in resolution known as the "proximity effect" [118]. The proximity effect causes features to be overdosed as they receive additional electrons from neighbouring features, see figure 3.2(b–c). The range of these backscattered electrons depends on the beam voltage, and on the type of substrate used. For a beam voltage of 30 kV and a Si substrate, the range is on the order of $10\,\mu m$ [119].

The proximity effect is typically overcome in one of two ways. One can use "pattern biasing", in which the sample's design is altered in some way to take into account the higher dose it will receive. An example of this would be taking the desired output shape of a vertical pillar or column, and biasing the pattern such that it is slightly concave. The extra dose that comes from neighbouring
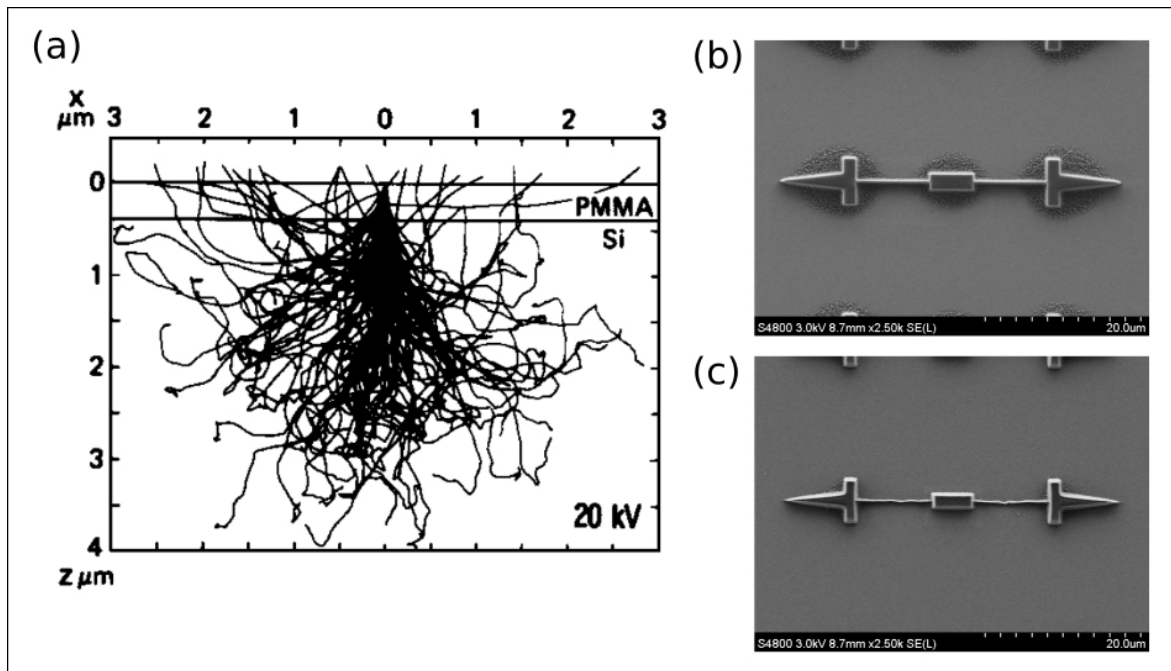
Figure 3.2: (a) Monte Carlo simulation of the scattering of an electron beam as it propagates through a dielectric medium (reproduced, with permission, from [117]). The beam broadens as it passes through the resist due to forward scattering, while electrons which penetrate into the substrate undergo back scattering. (b - c) The proximity effect, whereby backscattered electrons lead to an overdosing of designs. (b) Microtool design suffering from proximity effect, and (c) the same microtool but with an adjusted dose to counteract this effect.

pillars then acts to "fill in" the concavity, resulting in the straight pillars as desired. Alternatively one can adjust the dose each feature receives, rather than altering its design. The underlying philosophy is the same: the sum of this dose with the dose from neighbouring features results in the desired outcome.

3.3.2.2 Machine operation

Figure 3.3 shows a block diagram of the main components of the EBL system [120]. At the top of the machine is an electron gun, which generates the electrons needed to pattern the sample. These electrons are formed into a beam as they pass through the column, by being conditioned by a series of electron lenses and apertures. This beam is then focussed onto the sample by the final lens. The beam is scanned across the surface of the sample by deflecting it with a pair of electromagnetic coils. As the beam is moved off-axis, aberrations are introduced into the beam which worsen linearly with deflection angle. To limit the impact of aberrations, the angle deflection is limited by defining a "write field" for system. This write field is the area which can be patterned by deflecting the electron beam, and is related to the magnification and working distance of the system. The EBL parameters used in this thesis are summarised in table 3.2.

When a pattern is generated, the EBL system breaks it down into write fields. Within each write field the beam is deflected in steps of several nm as defined by the system's "step size". The beam is blanked as it is moved through the sample to ensure that unwanted areas are not exposed. The beam is kept stationary for a brief "settling" time at each position in order to give the system enough
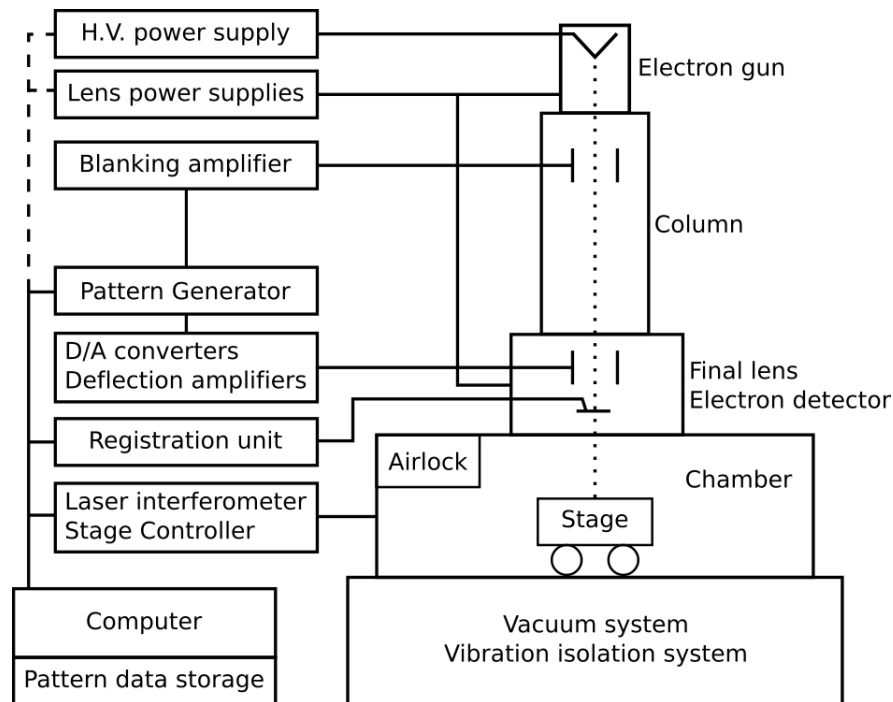
Figure 3.3: Block diagram showing the major components of an EBL system, recreated from [120].

time to un-blank the beam and write the desired feature. Once one write field is patterned, and the stage then drives to the next write field. This continues until the entire pattern has been written. This approach means that beam deflection is limited to an extent that aberrations are not an issue, however one does have to consider the positional accuracy of the stage. In general EBL will suffer from "stitching errors" whereby adjacent write fields do not match up with each other, and may produce overlaps or spaces between them. To minimise this effect, a computer-controlled algorithm known as "write field alignment" is used.

Write field alignment presents the user with an image of the EBL system's current location on the sample. Typically the user writes a few contamination spots in this area such that the image is mainly black with a few bright, recognisable features. The stage is then driven away, in a lateral direction, by some amount (usually 100 μm at first) and the beam is deflected back by the same amount. The user is shown the resultant image from this deflected beam scan. If the write fields are perfectly aligned then the two pictures will be identical, however this is almost never the case. In general there will be some shift between the images due to the fact that beam deflection and stage movement are not properly calibrated to one another. Provided with the second image, the user manually enters the position of one of the recognisable features that was defined earlier. By doing this, the EBL system learns how far away it is from acceptable calibration of the stage and beam. This process is carried out a total of four times (positive and negative displacements in the x- and y-axes) per run. Typically one run is done at a low magnification, one run is done at a medium magnification, and as many runs as necessary are carried out at high magnification (usually 3 or 4).

3.3.3 Chemical development

After the cross-linking and post-exposure bake are completed, the areas which have not been cross-linked are removed by submerging the sample in a beaker of EC solvent (MicroChem) for 30 s. The

active ingredient in EC solvent is ethyl lactate (also present is a small amount of surfactant) which dissolves non-polymerised SU-8. From the EC solvent, the sample is transferred to IPA where it is left for 30 s. IPA stops the reaction brought about by the ethyl lactate, and helps clean off any contaminants that may have formed. The sample is again addressed with a nitrogen gun to remove the IPA and any dirt or dust that may be dissolved in it.

3.4   Plasmonics

In the instances were plasmonic features are desired, an additional fabrication step is required. With the exception of rigid SERS substrates, where gold is applied directly onto the glass, the plasmonic layer is defined immediately after the membrane layer. Although it is possible to generate plasmons in any metal, it is common to define plasmonic features using either silver or gold. This is because the imaginary parts of the refractive indices of gold and silver are the lowest of all metals. As a result, they are the metals which produce the lowest losses. Silver has the lowest losses but will readily react with air to form silver oxide. Gold, with the second-lowest losses, is much more inert and therefore does not form its oxide so easily. The plasmonic features discussed here are made from gold because the benefit gained from their resistance to chemical degradation far outweighs the disadvantages related to their increased losses. Not only does gold bond readily with SU-8 [121], but, like SU-8, it is also biocompatible [122], making it an ideal candidate for use in a biophotonic environment.

3.4.1   Electron-beam evaporation

Electron-beam evaporation is primary method used to deposit gold onto photonic membrane samples. An Edwards AUTO 306 electron-beam evaporator was used for all recipes presented here, with all gold layers deposited to a thickness of 40 nm.

The main components of the machine are an electron source, and a crucible containing the material one wishes to deposit i.e. gold. The electrons are focussed using magnets, and directed to crucible, were they cause the gold to evaporate. A deposition rate of $0.05\,\mathrm{nm\,s^{-1}}$ is achieved by using a beam current of $80\,\mu\mathrm{A}$, with the thickness being monitored by a quartz crystal detector. This detector is effectively a crystal attached to the end of a cantilever. As gold is deposited its mass is added to that of the crystal, which results in a shift in its resonant frequency. The thickness of gold deposited is then inferred from this frequency shift. The electron-beam evaporator is pumped down to a pressure of $9 \times 10^{-6}\,\mathrm{Pa}$ before evaporation is commenced. The pressure during the evaporation process is typically $2 \times 10^{-5}\,\mathrm{Pa}$.

3.4.2   Patterning via EBL

In order to pattern the gold layer, one first spin-coats a layer of SU-8 on top of it at a thickness of 90 nm (see table 3.1). This layer is baked in the standard way, at 100 °C for 5 min with a temperature ramp from 65 °C to 100 °C over the first minute.

The plasmonic features fabricated in this thesis were fishnet gratings, with a wire spacing of 400 nm and a wire width of 90 nm. For flexible SERS sensors, these fishnets were 7 mm by 7 mm in size, whereas for rigid SERS substrates they were organised into a 3 by 3 array of fishnet "pads", each one 200 μm by 200 μm in size. They were patterned using the same EBL procedure outlined above, albeit with different parameters (see table 3.2 for specific details). After EBL the sample is baked at 100 °C for 2 min to finalise the cross-linking process.
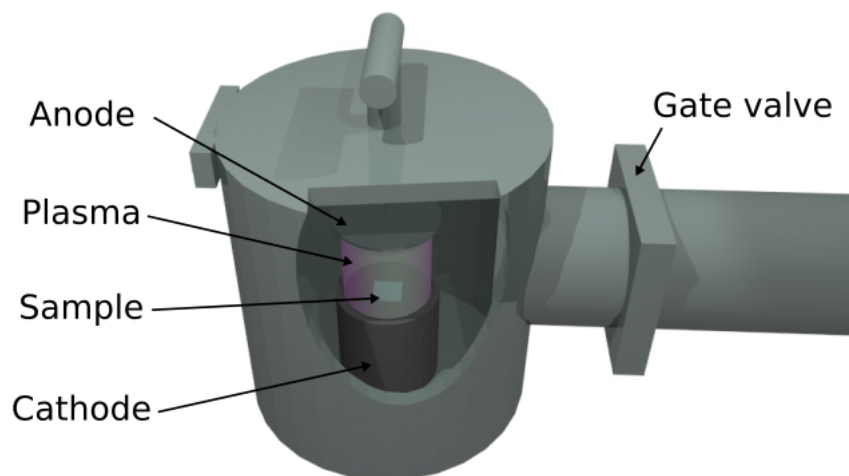
Figure 3.4: Cut-away diagram of RIE. A RF signal ionises the gas present in the chamber, creating a plasma, and the anode and cathode accelerates this into the sample. The gate valve is adjusted to maintain the appropriate pressure at the sample.

3.4.3 Development

Development of the sample is carried out in the standard way, by submerging it in EC solvent for 30 s followed by IPA for 30 s. The sample now has areas of exposed gold where the SU-8 was not patterned by EBL, and these areas can be removed via RIE. The cross-linked SU-8 shields the underlying gold from the etching process. The sample is etched for long enough that the cross-linked SU-8 will just be removed by the RIE, leaving the patterned gold underneath.

3.4.4 Reactive-ion etching

Figure 3.4 shows the a diagram of the major components of the reactive ion etcher. Once the sample has been loaded onto the stage, the sample chamber is pumped down to a pressure of 3×10^{-6} Pa to eliminate any impurities found inside. Argon is pumped into the top of the chamber at a rate of $500 \, cm^3 \, min^{-1}$ and the gate valve is adjusted until the pressure settles to 5×10^{-2} Pa. At this point a RF signal (13.56 MHz) is produced between the top of the chamber and the sample stage which ionises the argon. The argon nuclei are relatively heavy, and hence remain stationary, while the lighter electrons are free to move around in the chamber. Those electrons which reach the top-plate or walls of the chamber are conducted to ground, whereas the electrons incident on the electrically-insulated sample stage cause charge to build up there. This creates a potential difference inside the sample chamber. This potential difference, or direct current (DC)-bias, is one of the most critical parameters in RIE because it is responsible for accelerating the Argon ions toward the sample, and is directly related to their kinetic energy. A DC-bias of -330 V was used during all RIE performed in this thesis. This was achieved by setting the RF power to 19 W.

Argon is chosen as the gas used in RIE for two main reasons. Firstly, argon ions are heavy nuclei which allows them to etch the sample's surface. Secondly, on a related note, argon is inert. This means that any argon-based etching will be purely physical. Other gases can give a secondary etching affect due to them interacting chemically with the sample, but as gold is already non-reactive, this is not necessary. RIE of the samples was performed for 11 min 30 s.
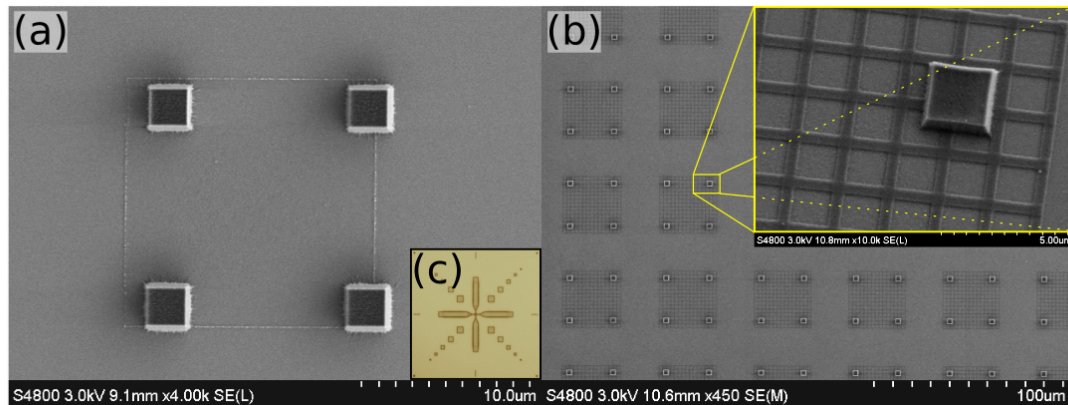
Figure 3.5: The effects of three point alignment. (a) Poor three point alignment resulting in a shift between the membrane and handle layers of a photonic membrane. (b) The result of correct alignment, demonstrated on another photonic membrane. Note this time that the handles are positioned symmetrically about the membranes' centres. Inset shows closer view of a handle, highlighting that the angular alignment is also of high quality. (c) An alignment mark used during the procedure, as seen through an optical microscope.

3.5 Handles for optical manipulation

Handles were required on any sample that was to be manipulated via optical tweezers. Defining these handles meant repeating the procedure for fabricating the membrane layer, but with different parameters. A 3:1 ratio mixture of SU-8 2000.5 and SU-8 2050 was spun at 3000 rpm in order to give a layer thickness of 1.5 µm. As usual, this was baked at 100 °C for 5 min with a temperature ramp from 65 °C to 100 °C over the first minute. Four square handles were written directly over each membrane, using EBL, such that there was one handle in each corner of the membrane. After EBL the sample was developed in EC solvent for 30 s, before being cleaned using IPA (30 s) and a nitrogen gun. No post-exposure bake was performed with this layer in order to give the handles a slightly curved profile. It was hoped that this would improve stability of the handles when they were trapped, as light refracted at sharp corners does so in an eratic manner that would be detrimental to trap stiffness.

The EBL system uses two different coordinate systems: global coordinates and local coordinates. Global coordinates have a physical basis and are linked to the sample chamber itself. In contrast, local coordinates are defined through software by the user and are typically made relative to the sample. After the sample has been loaded into the EBL system for the writing of its handles, it will no longer be sitting in the exact position it was in during the writing of the membrane layer. In other words, it now has a different set of global coordinates. This is not a critical requirement however, as long as its local coordinate system matches the one that it had before.

To this end, an algorithm known as "three-point alignment" is used. Alignment marks are incorporated into the design of the membrane layer, usually around the perimeter of the sample, and as such their positions relative to the membrane features are known. These marks are covered with tape whilst the handle layer of the sample is being spin-coated so that they are still visible when the sample is viewed through the EBL machine. The user drives the stage to the position of one of the markers, and tells the computer where its centre is in terms of the global coordinates of the system.
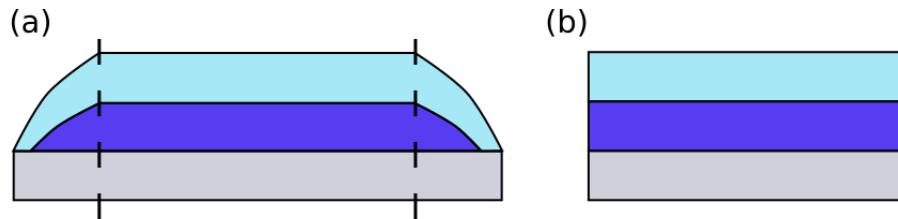
Figure 3.6: Diagram showing the importance of cleaving during the lift-off process. Silicon substrate shown in grey, Omnicoat shown in purple, and SU-8 shown in light blue. (a) By default the sacrificial layer is not accessible, but (b) after cleaving it is fully exposed to lift-off chemical.

The software then compares this to where it knows the marker must be located in local coordinates. This process is repeated for a total of three markers, at which point the computer will have generated a coordinate transform between the global and local coordinate systems. This transform allows the computer to knows where to write the handle features such that they match up with the membrane layer. As the name suggests, this algorithm needs three points in order to work, however for the sake of redundancy five or six alignment markers are typically made.

An additional complication to the fabrication process is that performing three point alignment using marks that are so thin (under 90 nm) requires a change in the acceleration of the beam. As mentioned earlier, a higher acceleration voltage gives better resolution, which is why the maximum voltage of 30 kV is used. However, this voltage is so high that electrons simply penetrate the alignment marks, making them impossible to see.

Initially the approach towards this problem was to perform three point alignment at a lower voltage, i.e. one that could detect the markers, and then switch back to high voltage to perform the actual writing. However, the problem with this technique is that the beam condition changes as one changes the accelerating voltage. Specifically, one will have a shift between the two layers. To counteract this, a procedure was developed which effectively aims to make the alignment marks visible at the high accelerating voltages used for EBL. The first stage in the process is to find the alignment marks using low accelerating voltages (in the range of 5 kV), and to burn contamination spots in the middle of them. The accelerating voltage is then increased in steps of 5-10 kV, and another contamination spot is patterned directly on top of the previous one. After each stepwise increase in voltage, the stigmation and alignment of the beam are readjusted to ensure that the contamination spots that are being written are as reliable as possible. Once the spots are visible at 30 kV, three point alignment can be carried out as normal. Alignment of the two layers extremely good, to the extent that no shift between them can be detected when they are analysed under a scanning electron microscope (resolution = 10 nm).

3.6 Lift-off and sample preparation

To remove the finished sample form the substrate it is necessary to dissolve the sacrificial layer, either in N-Methyl-2-pyrrolidone (NMP) or Microposit MF-319 developer. The edges of the sample are cleaved to allow the lift-off chemical better access to the sacrificial layer, see figure 3.6. The choice of chemical comes down to considerations of process time, and eventual application of the photonic membrane. NMP heated to 70 °C results in membrane detachment over the course of 1 h to 3 h, whereas MF-319 (at room temperature) can successfully lift-off a membrane in 30 min. When processed with NMP, the membranes exhibit hydrophobic behaviour which can be useful in the mounting process outlined below. If MF-319 is used as the lift-off chemical no such behaviour is observable.
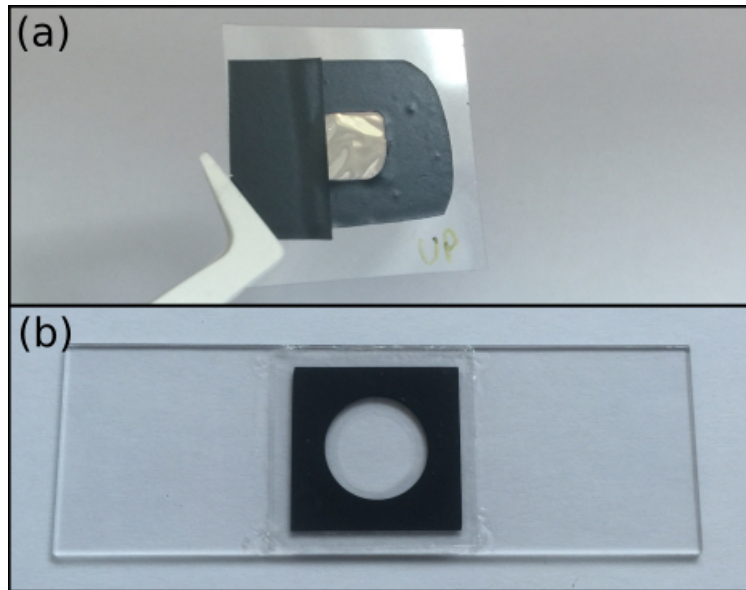
Figure 3.7: The sample presented in this thesis are typically prepared in one of two ways. (a) Large membranes for SERS applications can be mounted in acetate frames, while (b) microfluidic photonic membranes are incorporated into microscope sample cells, ready to be integrated into an optical tweezers system.

As a general rule, if large membranes were being processed for SERS applications then NMP was used. In these cases, the sample is submerged in a Petri dish containing NMP. Once it has lifted-off, it is scooped from the NMP using a piece of silicon and transferred to a beaker of deioinised (DI) water. Here it becomes suspended on the surface of the water due to its hydrophobic nature, which makes it much easier to access and manipulate. From here it is mounted onto an acetate or polystyrene frame where it is stored until it is used in an experiment, see figure 3.7(a).

The lift-off procedure for photonic membranes that are to be optically manipulated utilises MF-319 as the lift-off chemical. Not only does one benefit from a decreased membrane detachment time, but the resulting membranes are not hydrophobic; as a consequence their behaviour is not complicated in a microfluidic environment is not complicated by the presence of hydrophobic forces. The sample is placed into a vial (with the sample being cleaved into strips to ensure that it fits) along with $0.5\,\mu l$ of MF-319. Lift-off proceeds as normal and within $1\,h$ one has a photonic membrane solution. This solution can be incorporated into a microscope slide to be used in an optical trapping experiment in the same way that more typical microsphere solutions are. This involves taking a microscope slide and applying an adhesive vinyl spacer to it, see figure 3.7(b). $100\,\mu l$ of the photonic membrane solution is dropped inside the spacer and a glass coverslip (L46S24-1, Agar Scientific) is placed on top, taking care to make sure that no air bubbles have become trapped in the sample. The sample area is then sealed by applying nail polish to the four corners of the coverslip, and once this has dried, around the remaining perimeter. Applying the nail polish to the corners first ensures that the coverslip is adhered to the microscope slide. This prevents the coverslip from moving around as the nail polish is applied to its edges. Nail polish is used as a sealant because it is cheap, quick-drying, and transparent.

3.7 Summary

This chapter has outlined the fabrication procedures responsible for creating rigid and flexible SERS substrates, as well as photonic membranes that are capable of being manipulated via optical tweezers. The application towards optical manipulation is particularly novel, in that membranes have not historically been compatible with this technology. Because of this fabrication protocol, the utility of optical tweezers is extended to a new class of target geometries.

The main limitation of this fabrication protocol arises from the inherently planar nature of EBL. EBL is capable of creating high resolution features, on the order of 10 nm in size, however this resolution is only achievable in directions perpendicular to the normal of the sample. Due to the diffusive nature of the electrons, the range of structures that can be fabricated into the sample itself, along the beam direction, is limited. While this is not a problem for any of the structures discussed here, if one were to extend this work into more complicated, 3-D, structures then another fabricational approach would be required, e.g. two-photon polymerisation (TPP). The major advantage that EBL has over techniques such as TPP is its throughput and automatability. An EBL write will take approximately 1 h to set up, and once it is running it is entirely automated. When the sample is unloaded the next morning, the number of photonic membrane features that have been defined is on the order of 2,500,000.

Contributions

The basic fabrication recipe for photonic membranes was introduced to me by my supervisor, Andrea Di Falco. Since then I have made continuous modifications and improvements to the fabrication procedure, making the first membranes that we could use in a microfludic environment, capable of being manipulated via optical tweezers.

Holographical optical tweezers: set-up and characterisation

This chapter outlines the use of HOT for optical manipulation. I will describe the system that I built during my PhD with a particular focus on the discussion of the SLM, the key component in a HOT system. Additionally, I will discuss the methods used to extract metrics of performance of the system. This was achieved by tracking trapped objects and analysing their dynamics through the equipartition theorem.

All of the apparatus and computer programmes described in this chapter were built from scratch, by me.

The structure of this chapter is as follows. A brief overview of the HOT system employed in this thesis is provided, followed by a discussion on the importance of HOT technology as a technique for beam-steering. The various components and operation of our HOT system is given, with a particular focus on the SLM. Discussion of the SLM includes its underlying working principle, its operation, and its application to trap generation and wavefront correction. The methods used to characterise the performance of the HOT are then explained in detail, with examples.

4.1 Overview

HOT were chosen as the means of optical manipulation in this thesis due to their versatility and relatively simple design. While many HOT systems are built by incorporating a laser into a confocal optical microscope, simpler, stripped-down designs are also commonly used [123]. Such a stripped-down design was used here, which can be seen in figure 4.1, with the key components highlighted. The operating wavelength of the laser is 830 nm, with a maximum achievable power of 230 mW. To generate a net force backwards along the beam direction we use a water-immersion objective lens with a NA of 1.2.

The SLM is controlled via a custom built graphical user interface (GUI) written using LabView. This GUI allows the user to manipulate the optical tweezers manually, in real-time, or as part of a pre-defined automated sequence. This programme is also capable of saving images or videos of the trapped objects. Videos of trapping membranes or particles are passed onto a Matlab programme where they are analysed. This programme tracks the movements of trapped structures and extracts their trap stiffnesses.
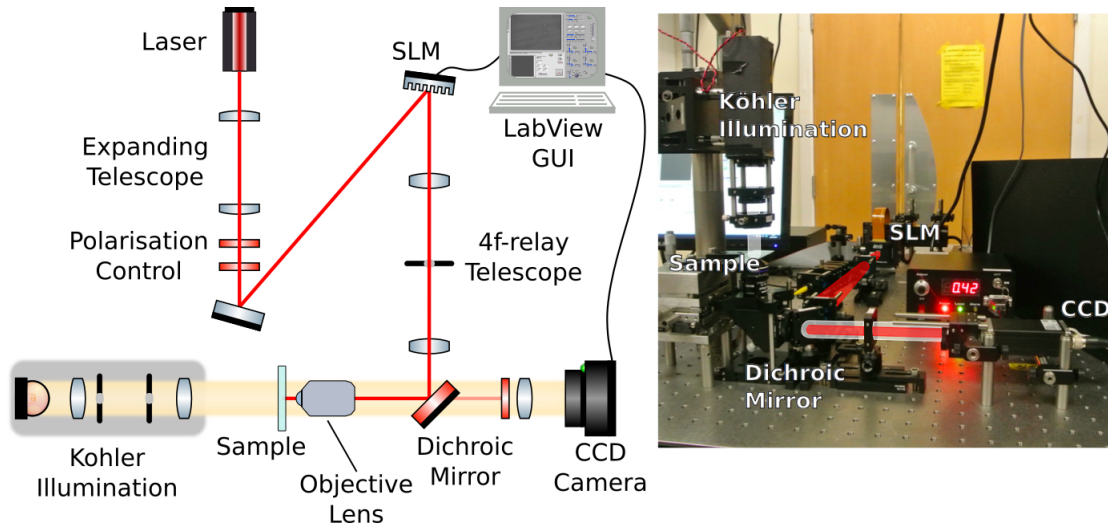
Figure 4.1: Schematic diagram of the holographical optical tweezers system used in this thesis [124]. A 830 nm laser is expanded, and passed through polarisation-control optics, before overfilling a SLM. Desired phase structures displayed on the SLM are imaged into the back focal plane of an objective lens via a 4f relay-telescope. The objective lens (a 60×, water-immersion objective with NA=1.2) forms an array of optical tweezers while also imaging the sample as part of an optical microscope. This microscope is illuminated from above via a Köhler illumination arrangement, and uses a tube lens with a focal length of 150 mm.

4.2 HOT system

In this section I describe the HOT set-up used in this thesis, addressing the three major components of it in turn. These components are: the imaging system, the laser used for trapping, and the SLM. In the case of the SLM I will discuss its operating principles and the specific computer programme used to control it.

The HOTs system was used to manipulate the membranes and other devices in an aqueous environment. For a basic optical tweezers system, a gaussian laser beam is focussed using a high numerical aperture lens such that the focus comes to a plane inside the sample cell. Particles can then become trapped in the focal spot due to gradient force of the laser beam [39]. In addition to the laser line, there is also an illumination line, typically running in a counter propagating direction to the laser, and a camera. Some setups are simply converted microscopes, with one of the ports being used to accept a laser line input. However, in the interest of cost and simplicity, the system described below was built using minimal components. Despite this, it retains all the functionality of a microscope-integrated system while its minimalist design grants it increased ease-of-access and versatility.

4.2.1 Imaging system

The sample of interest is illuminated from above using a white light-emitting diode (LED) (Thorlabs, model number LEDWE-15). It is then imaged onto a charge coupled device imaging sensor (CCD) camera via a telescope consisting of an objective lens and a tube lens. The objective lens used was an infinity-corrected, UPSALO 60× water-immersion objective from Olympus, which had a NA of 1.2. The tube lens was a biconvex N-BK7 lens with a focal length of 150 mm (Thorlabs).
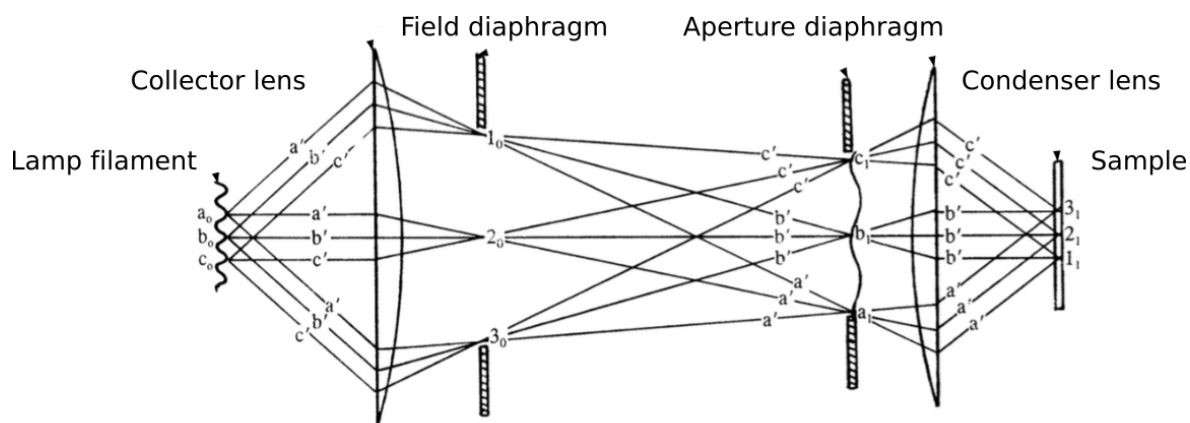
Figure 4.2: Schematic diagram of a Köhler illumination system. Two lenses act to provide even illumination of the sample by ensuring that light rays leaving from the same point in the light source reach the sample as parallel ray bundles. Two diaphragms control the brightness and contrast of resulting images. Adapted from [125].

To prevent hotspots being visible in the imaged sample, the LED was integrated into a Köhler illumination structure [125]. This arrangement of lenses and apertures allows the user to create flat, distributed illumination even when using a point-like source such as a LED. The key characteristic of such a Köhler system is that all light-rays which originate from a particular point in the plane of the light source will arrive at the sample plane as parallel ray-bundles. In this way the image of the light source is completely defocussed at the sample (figure 4.2).

The procedure for achieving Köhler illumination is to use a "collector" lens to image the light source onto an adjustable iris. This iris is known as the aperture diaphragm (AD). A second lens, the "condenser" lens, is then placed one focal length behind the AD, i.e. the AD lies in the front focal plane (FFP) of the condenser lens. The final component is the field diaphragm (FD), which is placed in the BFP of the collector lens. The FD is conjugate with the sample, and therefore controls the size of the illuminated area of the sample, while the AD, conjugate with the LED restricts the angular spread of the light which arrives at the sample from a single point on the source.

In this thesis biconvex N-BK7 lenses from Thorlabs were used for both the FD and AD. These lenses had focal lengths of 30 mm and 25.4 mm, respectively. The diaphragms were typically adjusted such that the FD was almost completely closed, whilst the AD was adjusted until the contrast in the microscope image was optimal. The Köhler system was mounted above the sample on a z-steerable stage. This allows the height of the system to be adjusted until the FD was successfully imaged onto the sample.

4.2.2 Trapping laser

The choice of laser for an optical tweezers system must be compatible with the environment in which one wants to trap. A continuous wave LuxX 830-230 diode laser operating at 830 nm (supplied by Omnicron Laserage) was used in this thesis. The laser was able to achieve a peak power of 230 mW, and operating and operated in the TEM-00 mode with a M^2 value of 1.05. Using infrared (IR) wavelengths is advantageous from a biophotonic perspective, as they are not strongly absorbed by biological substances such as cells. This reduces photo-damage caused to the cells, and allows higher optical powers to be used [126]. Operating at 830 nm also has the advantage that the absorption of

water is relatively low ($\approx 0.05\,\mathrm{cm}^{-1}$). This is in contrast to another commonly used wavelength of 1064 nm which has an absorption coefficient that is roughly 1,000 times higher.

The same objective lens that is used to image the sample also forms the optical traps from the laser. The choice of a high NA objective is important not just for good imaging, but is crucial for forming stable optical tweezers. As the NA of an objective lens is increased, the component of the optical gradient force acting backwards along the optical axis is made larger. The larger this component of the gradient force is, the more stable the optical traps become. A water immersion objective benefits from an increased NA because the refractive index of the water is higher than that of air. Additionally, spherical aberrations introduced into the wavefront when the light travels between media with different refractive indices is also lessened because water is used as both the immersion medium and the sample suspension medium [127].

One of the key components in a HOT system is the SLM. To be used effectively the laser is expanded such that the SLM becomes over-filled. This ensures that distribution of light across the surface of the SLM is as even as possible, while maintaining a Gaussian profile. To this end the laser beam is first expanded, by a factor of 8, using a telescope made from plano-convex lenses to maintain good beam quality. After the expanding telescope the beam is passed through a linear polariser and half-λ wave-plate which together control the beam's polarisation. The beam is then incident upon the SLM which is imaged into the BFP of the objective using a 4-f relay-telescope. Because the SLM and BFP of the objective are approximately the same size, and because the relay-telescope has a lateral magnification of 1, the condition that the beam overfill the SLM means that the objective is also over-filled. This is desirable as it means the full NA of the objective is utilised. Finally, the objective lens focusses the laser down to a spot in the plane of the sample, where it is used to manipulate the desired structures or particles.

In order to integrate the laser beam into the optical path of the setup a dichroic mirror is placed between the objective lens and the eyepiece lens. This allows the laser to enter through the objective lens and be focussed into the sample, while also allowing some of the laser light to be reflected back down the microscope where it is imaged by the camera. Visualising the beam in this way aides in manipulating particles. Once the desired object has been trapped, the image of the beam can be blocked by adding a short-pass filter immediately before the CCD camera. In this way one can observe the behaviour of trapped particles without the image being washed-out by the residual radiation of the trapping beam.

4.2.3   Spatial light modulator for Fourier-space engineering

To generate multiple beams, and have all of them be steerable, a SLM is typically placed in a plane conjugate to the BFP of the objective lens [128] (although alternate designs are possible [129]). This was achieved by using a 4f-relay telescope made from two biconvex N-BK7 lenses with focal lengths of 150 mm (Thorlabs). The incident Gaussian beam experiences a phase delay across its wavefront that is dictated by the pattern displayed on the SLM. The resultant optical field distribution in this plane will then be Fourier transformed into the sample-plane by the objective lens. In general a SLM can display near-arbitrary patterns; the only real limit being the restricted size of the SLM itself. Therefore, the key to its operation is in knowing which patterns to display in order to obtain a particular result in the sample-plane.

Here I discuss the operating principles of a SLM, the way one decides on which patterns to display on them, and the LabView programme I created to allow the user to control the optical tweezers in the desired way.
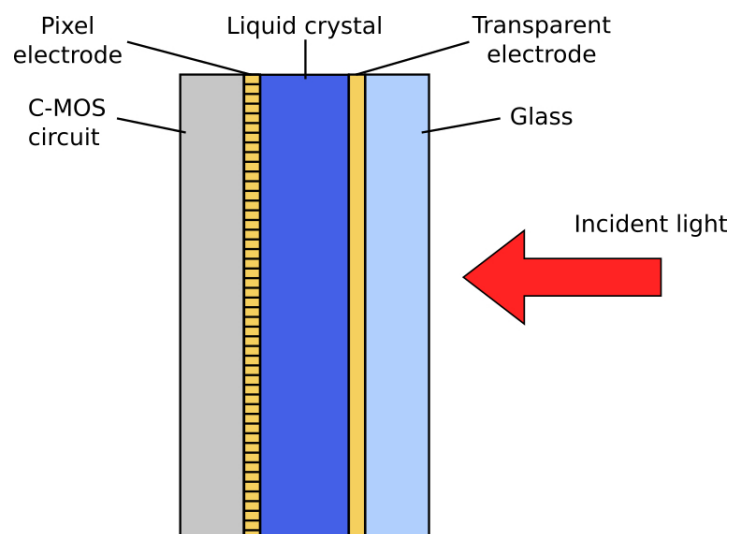
Figure 4.3: The inner workings of a spatial light modulator. Individual pixels can be addressed with a voltage, changing the refractive index of the liquid crystal in front of the pixel. This allows arbitrary phase delays to be applied to the incoming laser beam for beam shaping purposes.

4.2.3.1 SLM: operating principles, calibration, and constraints

At its core a SLM acts like a liquid crystal display (LCD) [130], see figure 4.3. At the rear of the device sits a C-MOS circuit which is used to apply voltages between the pixel electrode and transparent electrode, with each pixel receiving its own individual voltage. In between the two electrodes is a liquid crystal layer. The liquid crystal is composed of uniaxial organic molecules which can be made to align to an externally applied electric field. The final layer, on the front of the SLM is a sheet of glass. This encloses the device, and is typically anti-reflection coated to improve performance at the desired wavelength.

When a voltage is applied to a particular pixel the liquid crystals in front of that pixel start to rotate. As the voltage is increased the liquid crystals rotate more and more until they have fully aligned their long-axes with the electric field. Because nematic liquid crystals are also birefringent the refractive index of the liquid crystals in front of a particular pixel is in fact a function of the voltage applied to that pixel. Light which is incident on a particular SLM pixel will therefore experience a delay in phase which is proportional to this applied voltage. The SLM used in this work was an electrically-addressed SLM from Boulder Non-linear Systems. It had a 512×512 array of pixels which covered an area of 7.8 mm by 7.8 mm.

The SLM is attached to the computer and treated as a second monitor. Greyscale images are then displayed on it, with the greyscale value of each pixel determining what voltage will be applied to it. The voltages applied to a pixel translate into a change in refractive index of the liquid crystal immediately in front of that pixel, and so one can relate the greyscale value of a pixel to the optical delay imparted onto light that is incident onto that pixel. This relationship is illustrated in figure 4.4.

The full range of 256 pixel values will typically correspond to several full 2π phase delays. To successfully modulate the phase of incident light using the SLM one only needs access to a single 2π delay, meaning that one operates over a limited range of pixel values. This range of pixel values are chosen such that the response in the phase delay is linear, as highlighted by the red region in figure 4.4.

This region was accessed by defining two controls in the LabView programme that controlled
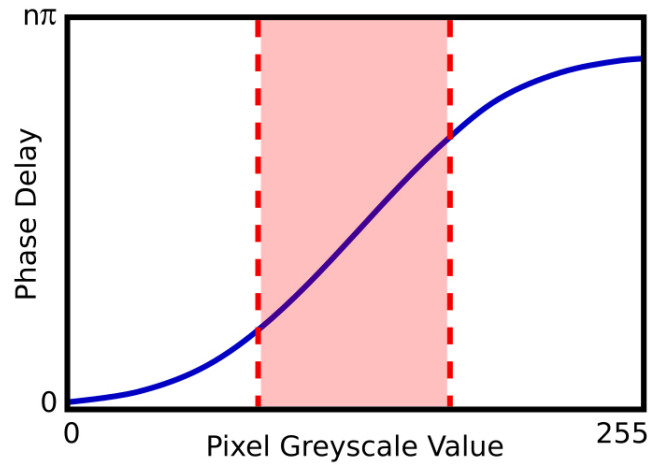
Figure 4.4: Cartoon illustrating the delay in the optical path in front of a pixel as a functions of that pixel's greyscale values. The SLM should be used in the linear region marked out in red.

the HOT. These controls, named "amplitude" and "offset", changed the gradient and y-intercept of the straight line representing the SLM response. They were altered until the straight line matched the linear regime shown in 4.4. In practice this is accomplished by displaying a blazed grating on the SLM and observing the relative intensities of the zeroth and first diffracted orders. The optimal values of the amplitude and offset are those which maximise the intensity of the first diffracted order.

Even once the performance of the SLM has been maximised there will still be losses associated with it [131]. An as example case, consider a SLM displaying a single blazed grating. Because only the first diffracted order is used in HOT, optical power that remains in the zeroth order is effectively lost by the system. Additionally, the structure of the SLM itself leads to further loses. Although SLMs are available which use their whole surface [132], most do not. Rather, the surface of the SLM is not continuous, but is instead made from a collection of pixels, each padded with a deadzone. As a result, the SLM acts as a $2 - D$ grating and therefore diffracts light into other orders regardless of what phase pattern is displayed on it.

Finally, if one tries to define a grating with too fine a pitch one runs into problems with the size of the SLM display itself. If the pitch is too high then there will not be enough pixels over which to alter the pixel values. The limit is where blazed gratings actually become binary gratings, where the pixel value simply alternates from high to low from pixel to pixel. The increase in the number of diffractive orders due to a blazed grating transitioning into a binary grating represents an additional source of losses.

It should be noted that these limitations do not degrade the quality of the traps which are formed, rather they restrict the amount of power which is directed into the usable first order diffracted mode As long as this limitations are kept in mind, HOT perform extremely well. This is especially true in terms of the versatility and control they grant the user.

4.2.3.2 Fourier-space engineering for HOT

The great advantage that HOT has over traditional optical tweezers is the ability to generate complicated phase patterns which can be updated in real-time [45], [133]. Of particular interest to this thesis is the ability to generate several optical traps from a single beam. Each of these traps can be moved independently of the others or, alternatively, an array of traps can be organised in a particular arrangement and then moved as a whole. This is of particular interest when it comes to
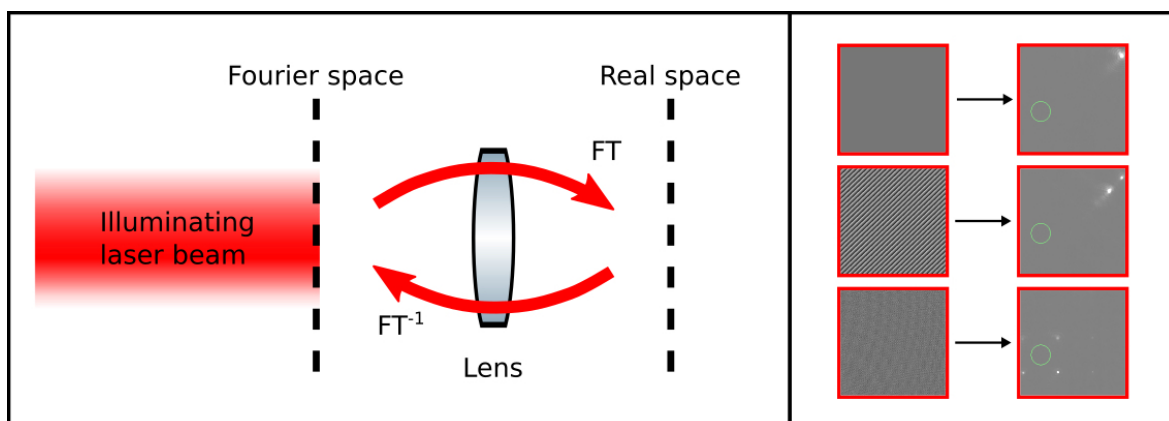
Figure 4.5: Diagram highlighting the function of a lens as a "Fourier lens". Fourier space (the plane of the SLM) a real space (plane of the sample) are related through a FT-inverse FT pair. The panel on the right shows affect that certain phase distributions in the SLM-plane have on the optical tweezers in the sample-plane.

trapping photonic membranes, as traps can be placed on the handles at each of the four corners and then moved in unison to manipulate the membrane.

The problem faced by the user is to calculate the appropriate phase structure to display on the SLM that gives the desired optical field at the sample. Since the SLM plane and the sample plane are a Fourier transform pair, there is a clear mathematical description which links the intensity of light in one plane to that of the other, see figure 4.5. However, although it is straightforward to calculate the amplitude of the optical field in the sample plane for a given optical field in the SLM plane, the opposite is not true.

Given a particular optical field distribution in the sample plane, one cannot simply perform an inverse Fourier transform to determine the field distribution in the SLM plane. This situation is an example of an inverse problem: a problem that is easy to solve in one "direction" but is extremely difficult to solve in the other. The classic example cited here is that, upon seeing a dragon one is able to predict what its footprints will look like. However, when faced with the footprints of a dragon it is impossible to infer its size, shape, colour and other properties.

The general solution to determining the appropriate pattern to display on the SLM is to perform some form of iterative algorithm, such as the Gerchberg-Saxton (GS) algorithm [134], see figure 4.6. In the GS algorithm one considers the amplitude and phase information of the light in both SLM and sample planes, in addition to the "source" intensity (in the case of this work, a Gaussian beam profile) and the "target" intensity (four optical traps). Starting in the sample plane, one considers a light-field with a flat phase structure and an amplitude equal to the target intensity. This light-field is then inverse Fourier transformed, resulting in a random phase and intensity distribution in the SLM plane. The phase information is kept while the intensity is replaced by the source intensity, with the resulting field being Fourier transformed back into the sample plane. This cyclical pattern of Fourier transforming and replacing intensity information leads to a gradual convergence in the phase information. This retrieved phase profile is then displayed on the SLM, giving the desired distribution of the optical-field in the sample plane.

The advantage to using iterative algorithms such as the GS algorithm is that one is able to generate arbitrarily complex field distributions in the sample plane. One disadvantage of this approach is that even to calculate a slightly different optical field the entire algorithm needs to be run again, which can be extremely time-consuming. Run times can be improved by using other algorithms
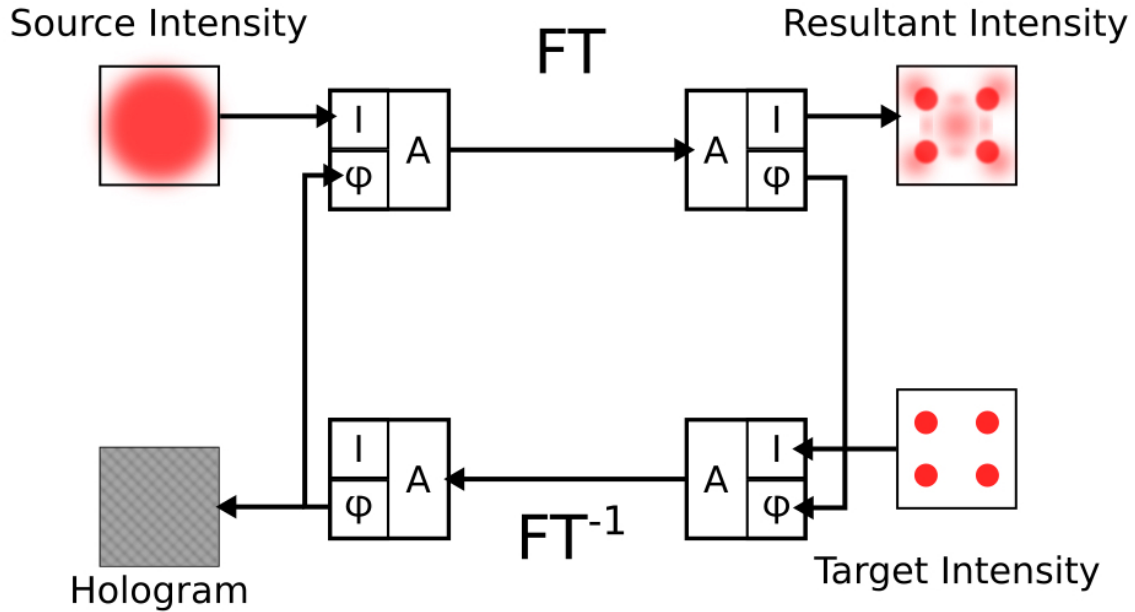
Figure 4.6: Graphical representation of the Gerchberg-Saxton algorithm.

besides the Gerchberg-Saxton [135], [136], but for the purposes of HOT, where relatively simple intensity distributions need to manipulated quickly, iterative algorithms are not well-suited and other methods tend to be employed instead.

The algorithm chosen for this thesis is known as "superposition of prisms and lenses". With superposition of prisms and lenses (SPL), a library of "solved" cases, namely blazed gratings (prisms) and Fresnel zone plate (FZP) (lenses), is used. These two basic patterns can be added together to displace the optical traps laterally and axially, respectively. This is ideal for HOT where any desired light-field in the sample plane is always in the form of some distribution of Gaussian focal spots. The simplicity of the algorithm makes it extremely fast and versatile.

To define SPL in LabView, a 256×256 matrix is generated which represents the display size of the SLM. The pixels can take values from 0 to 255, representing the grayscale value of the pixel as it will eventually be displayed on the SLM. To define a blazed grating one first defines a ramp in pixel value along a certain direction and uses modular devision to define the frequency of the grating. Similarly for the case of FZP, one takes the sum of the squares in x and y directions to define a radially varying pixel greyscale value. The pitch of this FZP can then be modified via modular division as before.

Most of the time four optical traps were used, with one trap being used to trap each of the four handles on a photonic membrane. By default these four traps are all generated in the same focal plane. Interfacing with HOT systems has been done in a number of ways [137]–[139], notably through the use of an Apple iPad [140] and real-time tracking of the user's hands [141]. The user controls the generation and manipulation of the optical traps through the use of a GUI written in LabView, see figure 4.7.

Each of the four traps can be turned on or off by clicking one of four virtual buttons, with each activated button generating its own blazed gratings and hence creating its own trap. The coordinates of each trap in x and y come from the x and y components of the vector which defines their blazed

grating. As the slider controls for the *x* and *y* coordinates of the trap are increased the pitch of blaze grating also increases, which translates the optical traps farther from their (0,0) position. There is one such pair of slider controls for each of the traps. Similarly, each trap had its own slider control to govern its translation along the *z*-axis.

Additionally, another set of controls (two for lateral displacement and one for axial displacement) are defined within the system which are responsible for manipulating all optical traps simultaneously. In practice this allows the user to turn activate the desired number of traps, position them individually (e.g. one trap centred over each handle of a photonic membrane), and then move the entire distribution of optical traps in unison. The ability to control the optical tweezers on both an individual and group basis is incredibly useful, and is the first step towards defining higher level controls parametrically.

Parametric control over structures such as photonic membranes is achieved by defining a default orientation for the membranes and expressing this as a vector. In-plane rotations are achieved by taking the membrane vector and multiplying it with a rotation matrix. Control over membrane "pitch" and "roll" is achieved by altering the axial position of various opposing pairs of traps by applying a pair of FZP. These FZP would have the same focussing power but act opposite sign i.e. if one trap was displaced downwards by 1 μm then the other trap would be displaced upwards by 1 μm.

All of the controls mentioned were available to the user to change manually in real-time. However, to free up the user and to make manipulation more precise, all controls can also be fully controlled via computer automation. This is achieved by utilising a state-machine architecture in LabView, whereby the programme passes through a number of states, with the condition of the current state determining which state the programme will pass into next. In each of these states there are a sequence of movement commands which are carried out in turn. These commands are set by the user and are typically in the form of "translate North 10 μm, rotate anti-clockwise 45°". Having the membrane follow a pre-defined path in an automated routine allows the user to focus their attention on other tasks. One can imagine photonic membranes functionalised as optical filters moving between particles in a sample. As they reach each particle they rest over them for a number of seconds, during which time the user can acquire a spectrum from the particle. This sort of computer-controlled manipulation can allow for a great increase in efficiency when it comes to experiments of this type.

4.2.3.3 Application of SLM to wavefront correction

The ability of the SLM to generate arbitrary phase patterns was also used to correct aberrations in the optical system. It is assumed that the laser beam incident on the SLM is perfectly Gaussian, but in reality this is not the case. In general there will be some form of optical aberration present in the beam that is responsible for altering the phase profile of beam away from the ideal case of the Gaussian beam. Aberrations can even arise from imperfections in the surface of the SLM itself [142]. These aberrations can be severely detrimental to the quality of the optical traps as they adversely impact the quality of the beam's focus [143]. Usually wavefront correction is achieved by detecting the aberrations in the beam using a Shack-Hartmann sensor [144], [145], with the SLM displaying a weighted sum of Zernike polynomials which counteracts this aberration [146], [147]. In this thesis, an *in-situ* method was used in which the signal from a probe embedded in the sample was used to correct the wavefront in the plane of the sample without the need for additional sensors [19].

The wavefront correction procedure consists of two distinct stages. The first stage is to determine the exact optical aberrations in the system, and the second is to calculate and apply an appropriate phase pattern on the SLM which exactly counteracts these aberrations. The underlying principle of the procedure relies on expressing the trapping beam as a *"composition of modes in an arbitrary representation"* [19]. The optimal focal spot is then obtained when the light in all of these orthogonal
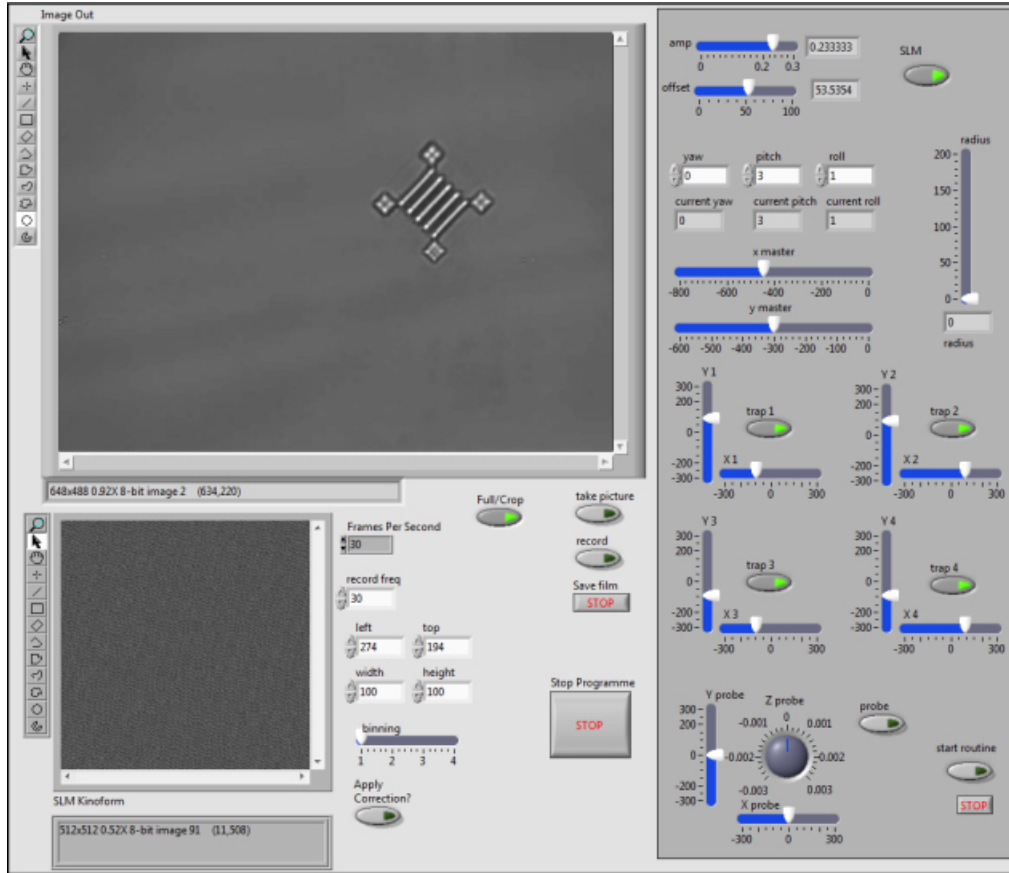
Figure 4.7: The custom-built LabView programme used to control the optical tweezers. The GUI included several sliders used to control the optical traps, as well as controls for SLM calibration. It also allowed the user to manipulate trapped objects in a pre-defined sequence of movements.

modes interfere constructively at beam focus. The display of the SLM is broken up into squares of pixels (typically 16×16 pixels in size), with these squares either displaying a flat phase structure (said to be in an "off" state) or a blazed grating ("on" state). Due to the interference conservation relation, the fact that none of the areas on the SLM overlap with each other is adequate to ensure that the light leaving each of these areas is orthogonal to all others [148]. With the light leaving the SLM now described as a collection of orthogonal ray-bundles, optimal focusing can be achieved by insuring these ray bundles interfere constructively at the beam focus.

A square of pixels near the middle of the SLM is switched on, diffracting the light incident upon it into the first diffraction order of the grating. This square of pixels is left on for the duration of the wavefront correction procedure, with the diffracted beam acting as the "reference" beam. Other "test" squares of pixels are then turned on, resulting in an interference pattern between the light leaving the test square and the light leaving the reference square. This interference pattern has maximal intensity when the two beams interfere constructively; a condition that can be met by applying a phase delay to the test square which varies from 0 to 2π. The applied phase which satisfies the condition for constructive interference is then assigned to the test square.

This process of testing squares is repeated until the entire area of the SLM has been probed and all squares have had an optimal phase delay assigned to them. When applied to the SLM these

phase delays correct any alterations to the Gaussian profile of the laser beam, thereby optimising the beam focus and trap stiffness. This "correction mask" is typically displayed on the SLM in such a way that it improves the quality of all traps simultaneously. Furthermore, any new traps which are generated after the application of the correction mask will still benefit from it and will have their focii optimised.

4.3 Characterisation through video analysis

As outlined in chapter 2, the equipartition model is used to determine the trap stiffness of the HOT system. A Matlab programme was written to process video files recorded during trapping by extracting the position of particles (or membrane handles) and tracking them frame-by-frame. Over the course of a single video (typically 10,000 frames) statistics are built-up around the position of each of the trapped particles from which the trap stiffness is inferred.

4.3.1 Identification of membrane handles

To illustrate this tracking algorithm the case of a membrane, trapped via handles at each of its four corners, is considered. The primary task is to identify the four handles, which is done in one of two ways. The first method is to use a centre of mass (COM) algorithm. Here a region of interest (ROI) is first defined around the area the handle is approximately located, with a padding factor to ensure that the handle does not leave this ROI during the procedure. Each pixel in this ROI has an x and y coordinate as well as a greyscale value, or "mass". In general, the pixel (x_i, y_j) has a mass of $m_{i,j}$. Considering the x-direction, the centre of mass theorem states that if one takes the mass of each pixel multiplied by its pixel index and sums this quantity over all pixels, the result is the same as would be expected from assuming all the sum of all pixel masses, M, is concentrated at a single point. This single point, X_{com}, is the COM in the x-direction, i.e.

$$X_{com}M = \sum_{i=1}^{p} x_i m_i.$$
(4.1)

Rearranging this equation, one arrives at the definition of the COM in the x-direciton

$$X_{com} = \frac{1}{M} \sum_{i=1}^{p} x_i m_i,$$
(4.2)

with an equivalent expression in the y-direction:

$$Y_{com} = \frac{1}{M} \sum_{i=1}^{q} y_i m_i,$$
(4.3)

where the COM is calculated over a ROI that has dimensions (p, q).

Handles typically have bright centres and dark edges, and are set against a background that has an intermediate intensity. The Matlab function *im2bw* is used to convert the default image into a binary image, whereby all pixels with intensities less than a chosen value are given a value of 0, while pixels with values higher than this are set to 1. This "chosen value" is known as the threshold value, and is set such that the bright central features of the handles will appear as bright spots on a black background. In reality there will be areas which "pass" this first thresholding condition which are not part of the handles; typically they are small areas of a few pixels. These unwanted regions cannot be removed through intensity thresholding alone as their intensities are so close to those of the handles. Furthermore, finer-scale intensity thresholding is not possible as a margin of error must be incorporated into the procedure to deal with variations in pixel intensity between video frames.
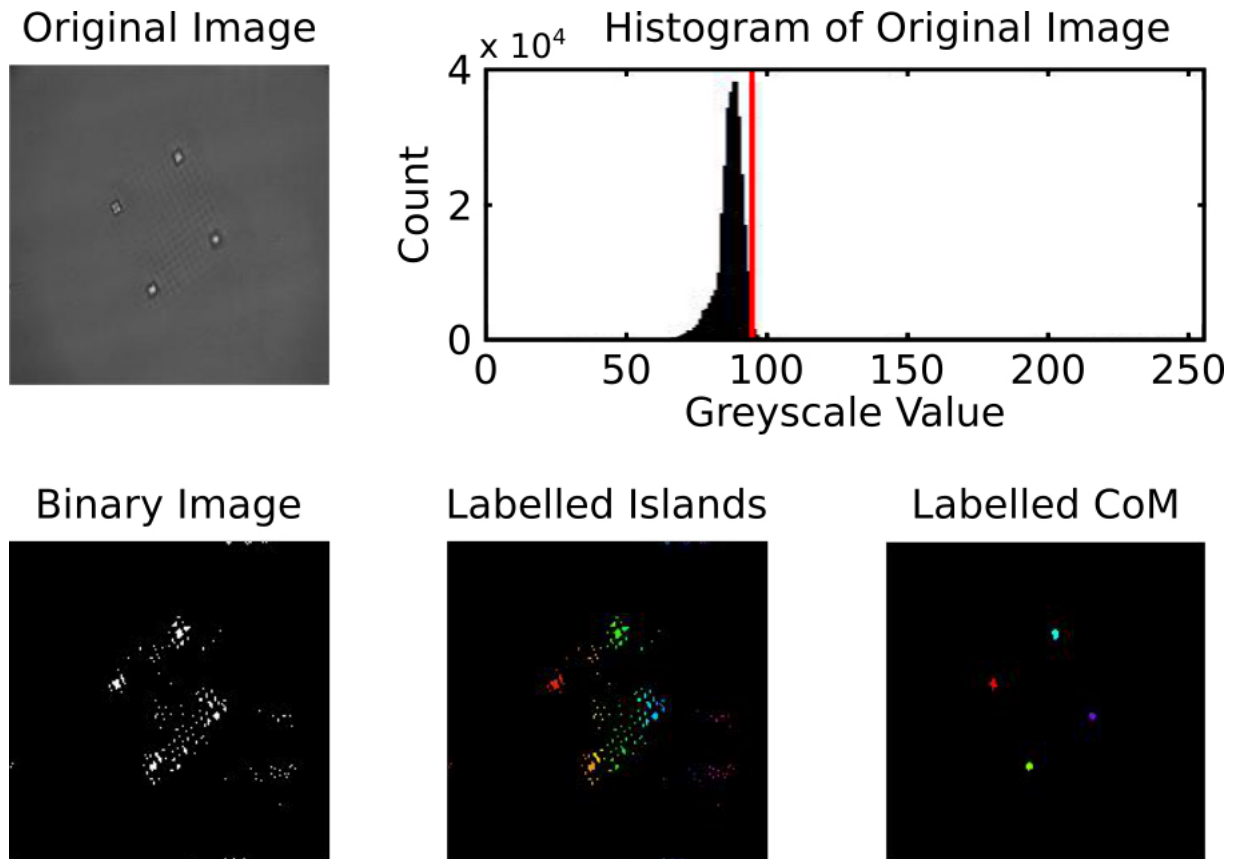
Figure 4.8: Screenshot of the custom-built Matlab programme used to track particles and membranes, based on a centre of mass tracking algorithm. The panels show the various stages of intensity and size thresholding necessary to extract the position of membrane handles.

To further distinguish handles from stray regions size thresholding is used. All areas which pass the initial intensity thresholding stage will have a particular size. As mentioned previously, the size of stray areas is far less than that for the handles and so by removing areas which are deemed to be too small one can successfully extract the positions of the four handles. Figure 4.8 shows the various stages of the thresholding procedure used to identify membrane handles.

The second approach to handle tracking was used when the centre of the membrane handles did not appear as a single bright region, but rather as a array of bright squares (as can occur when the focussing conditions of the handle are not optimal), the COM algorithm would fail because these bright squares were not large enough to pass the second thresholding condition. When this happened a second approach was used; one which detected edges in the image. The Matlab function *edge* was applied to each frame, and returned an image consisting of a series of lines representing the edges in the original image. These lines could either be open or closed. As only closed edges could define the boundary of the handles, all pixels belonging to open edges were discarded. Closed edges were then infilled to form solid areas such that the COM algorithm could then be applied to them.

Determining the position of handles using this approach was not as robust as the COM method, and so generally care was taken to ensure the focal conditions of all handles were such that they appeared as single bright spots. That being said, the reliability of the edge detection method could be increased by using multiple edges per handles, i.e. and inner and outer closed edge could be

found for most handles. Both of these could be in-filled, and there COM calculated. The eventual COM value used was then the average of the edges used.

4.3.2 Analysis of membrane dynamics

Once the handles of a PM have been identified, the membrane can then be tracked, and its behaviour calibrated [149], [150]. Tracking of trapped objects allows for characteristic quantities such as trap stiffness to be extracted from the system [151]–[153]. Additionally, it can allow force and positional feedback [154] to be added to the system which greatly improves their performance and applicability [155]–[157].

To ascertain how stably the membranes are trapped, the COM of each of their handles is recorded through all the frames in the video and histograms are generated of their position against time (see figure 4.9). The x-axis in the histograms represents the pixel number where the COM is located, and the y-axis gives the count of how many frames the COM appears at that position. Because any variations in handle position are caused by Brownian motion, a random process, the histogram data is fitted to a Gaussian distribution. The standard deviation of the Gaussian fit is related to the trap stiffness via

$$k = \frac{k_b T}{\sigma^2},$$
(4.4)

where k is the trap stiffness (typically quoted in units of $pN/\mu m$), k_b is Boltzman's constant, T is the temperature in the medium, and σ^2 is the standard deviation of the fit.

Occasionally during analysis, the histograms would not fit well to a Gaussian distribution. This was usually caused by sub-optimal thresholding during the tracking procedure which led to the extracted COM "hopping" between two values. This can be seen in some of the histograms in figure 4.9 as two distinct peaks. This has the effect of broadening the Gaussian distribution, which is no longer representative of the true behaviour of the system. To negate the affect of these stray occurrences, all histograms were subject to a goodness-of-fit test. Put simply, the data was analysed to see how Gaussian it really was, with a value of 1 representing a distribution which was perfectly Gaussian while a value of 0 represented completely random data. This test was not able to discern whether or not a particle was trapped (both trapped and non-trapped particles would generate Gaussian-like histograms), rather it could only discern whether or not the tracking algorithm was behaving "correctly". Any data which returned a value of less than 0.85 was discarded.

4.4 Summary

A HOT system was built from scratch, and controlled via a custom-built LabView programme. It allows membranes to be trapped and manipulated either manually or as part of a pre-defined sequence of movements. It addition to translating membranes, the system also grants control over the membrane's pitch, roll, and yaw.

Matlab was used to analyse the dynamics of trapped membranes using the equipartition model. This first involved designing a reliable method to extract the positions of the membrane's handles, which was demonstrated using both COM and edge-detection procedures. The extracted handle positions were plotted in histograms, with trap stiffnesses being extracted from the Gaussian distributions fitted to this data. Improvements could be made by pursuing a more robust form of membrane-tracking algorithm such as auto-correlation-based methods. These would be invariant to changes in the lighting conditions of the membrane due to sub-optimal focal conditions.
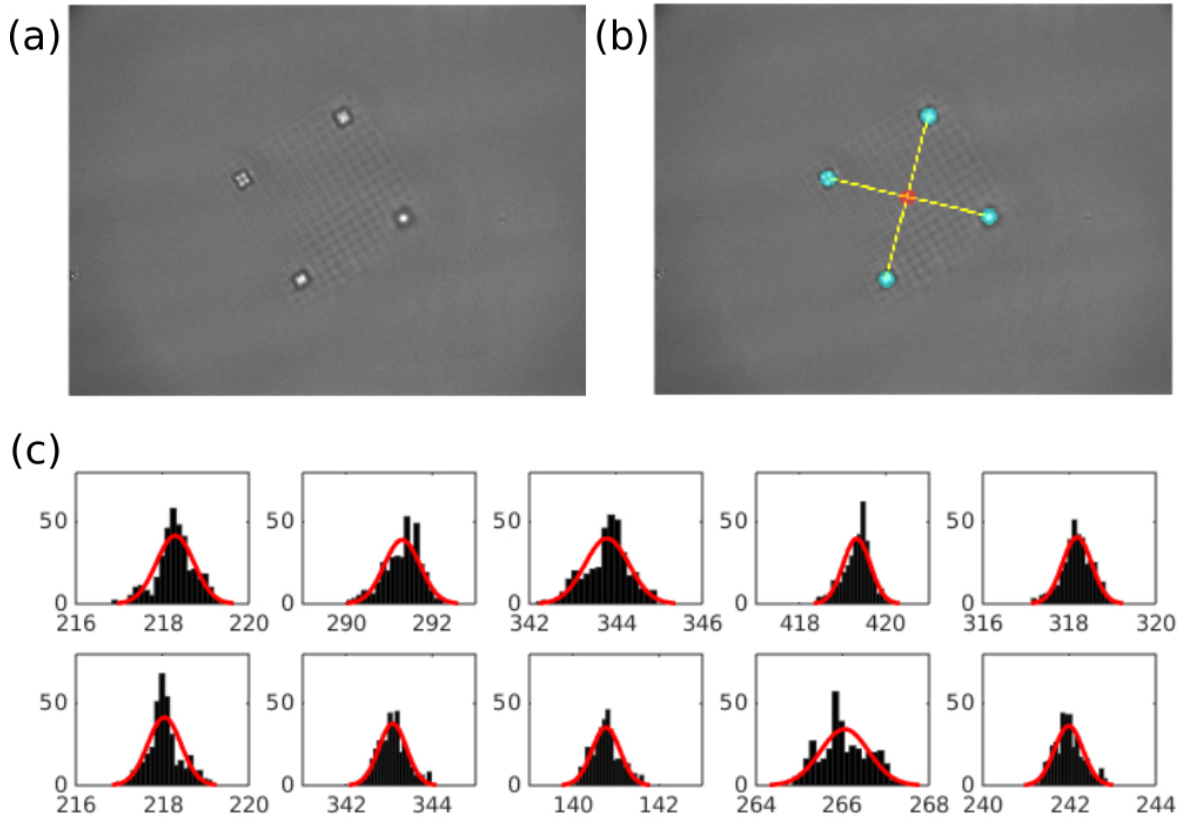
Figure 4.9: Screenshot of the custom-built Matlab programme used extract their trap stiffness of membranes and particles. The COM of the handles are tracked over all video frames, with histograms plotted of their position over time. This histograms were fitted to Gaussian distributions from which the trap stiffness of the optical tweezers was determined. Histograms which did not pass a goodness-of-fit test comparing them to an ideal Gaussian distribution were discarded.

Contributions

The HOT system outlined here was built and refined with the advice and expertise of Tomas Čižmár and Martin Ploschner.

All-optical manipulation of photonic membranes

This chapter demonstrates the optical manipulation of PMs through the use of HOT. The PMs discussed here are fabricated as outlined in chapter 3, and measure 90 nm in thickness and 15 μm to 20 μm in side length.

We begin with a discussion on why there is a need for this kind of optical-manipulation protocol, before moving on to report the capabilities of the system itself. Firstly, it is demonstrated that PMs are manoeuvrable with 6DOF control. Secondly, the performance of the system is determined by extracting values for the trap stiffness of a trapped PM. Finally, modifications in PM design are discussed. These come in the form of "fishnet" membranes which are more flexible than the standard PM.

The chapter concludes with a discussion of the impact of this work on the field of optical manipulation, particularly as it relates to the fields of microfludics, microrobotics, and biophotonics.

5.1 Introduction

The growing trend in optical manipulation is to take an holistic approach to optical trapping systems. With this approach the light and the particle are viewed as two sides of the one coin, both of which must be addressed if optical trapping is to be optimised. This shift in perspective has seen a great deal of emphasis placed on the design of the trapping object, as historically the properties of the particle have been overlooked in favour of those of the light. As a consequence, there has been an explosion of newly developed microscopic tools and particles which seek to extend the impact of optical manipulation in microfluidic environments. This work furthers this trend by considering the optical manipulation of PM.

5.1.1 Motivation

The driving force for this work is to exploit the versatile optical properties of PM in a microfludic environment. PM can have near-arbitrary optical functions, allowing them to act as any number of optical elements and devices. Their use at the macroscopic scale has been well documented, where their flexibility and robustness allow them to function as reusable, conformable, and robust filters and sensors. Their extension to the microscopic scale would enable the realisation of a whole family of *in situ* optical elements. Furthermore, because they are flexible, PM conform well to external objects when wrapped around them. This provides a pathway for PM to effectively transfer their photonic properties to other objects with the need to alter the object directly. One can imagine a PM being
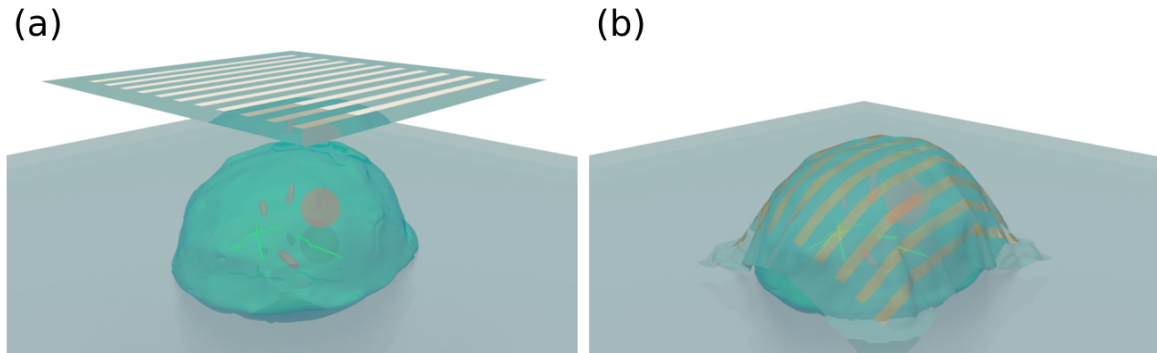
Figure 5.1: Sketch of a PM applied to cell in order to take a chemical readout from it. (a) A PM is lowered onto the cell and (b) conforms to its shape. The flexibility of the PM insures that contact between it and the cell is maximised.

wrapped around a cell and taking a chemical reading from it via, for example, surface-enhanced Raman spectroscopy (figure 5.1).

5.1.2 The need for optical tweezers

One restriction placed upon PM is that they must be positioned as closely as possible to the target object in order to perform effectively. This requirement stems from the evanescent nature of plasmon interactions - the basis upon which PM operate. Furthermore, one of the advantages of PM is their ability to spatially discriminate between various objects in a microfluidic environment. In order to take full advantage of this ability, a highly accurate positioning technique is needed. Optical tweezers were chosen to manipulate the PM because they offer extremely precise control over objects in microfluidic systems. Thus, in principle, they provide the accuracy required to apply the functionality of a PM to an external object, such as a cell.

As discussed in chapters 2 and 3, structure-mediated design is used in order to make PM amenable to manipulation via optical tweezers. Cubic handles (1 µm in side length), placed at its corners, allow the PM to be manipulated. This is accomplished by generating four trapping beams such that each beam traps one of the handles. These traps are then controlled parametrically to give the desired control over the PM.

5.2 Results

To demonstrate the capabilities of the developed optical manipulation protocol several different PM designs were made (figure 5.2). Generic membranes (figure 5.2(a)) were studied, as were PM that supported additional features such as rings or gratings (figure 5.2(a–b) respectively). It was found that the PM could be handled just as readily when they had these additional features as when they did not. In contrast, PM that had been made with a meshed design (5.2(d)) could be manipulated in a fundamentally different way to their solid counterparts. This stemmed from the fact that they were more flexible and could therefore be bent. In this section we look first at the degree of control one has over solid PM (with or without features), followed by an analysis of how effectively these PM are trapped. The section concludes with a discussion on the flexibility of meshed PM.
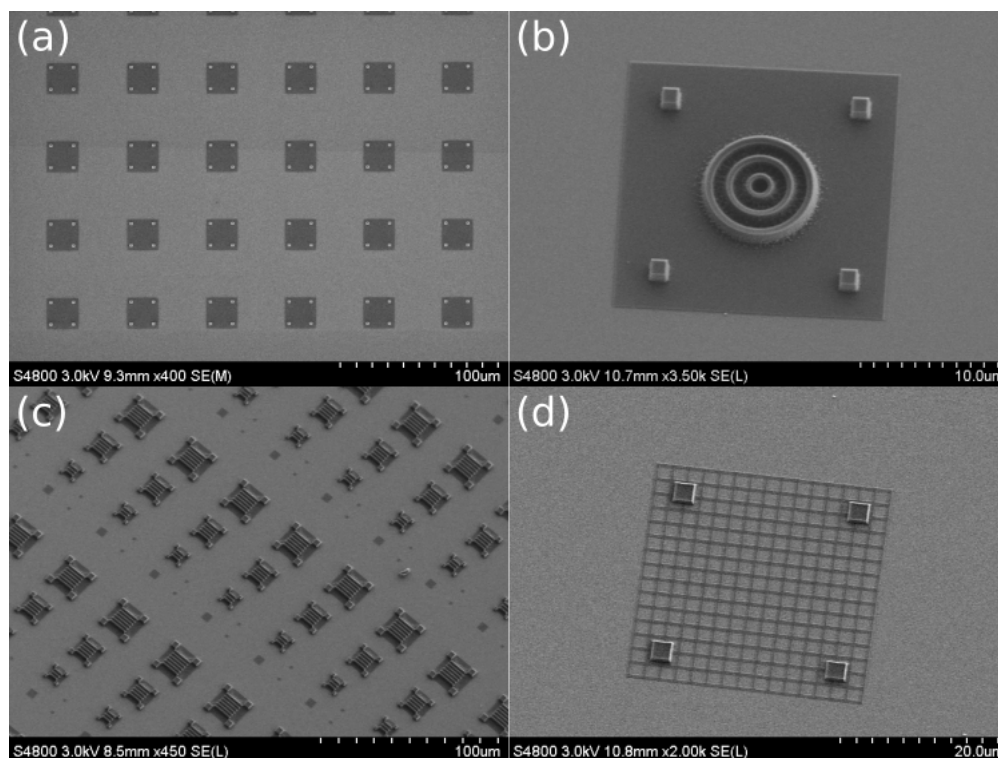
Figure 5.2: Scanning electron microscope images of the structures discussed in this chapter. Note the handle structures at the membrane corners. (a) An array of generic PM, and (b–c) PM with additional features (rings and gratings, respectively). (d) PM with meshed structure.

5.2.1 Optical manipulation of photonic membrane

PM like the ones shown in figure 5.2 (c) were trapped using the HOT system described in chapter 4. Four trapping beams were generated, with each one being placed at one of the handles on the PM. The optical power in the laser was kept low until the individual traps were all positioned correctly, after which point the power could be increased. If instead one created four full-power traps first, and tried to place them in turn, the system would not be stable. Typically the first handle which was trapped first would be pushed downstream slightly by the beam, resulting in the PM rotating in the sample. As a consequence of this trapping the other three handles became much more difficult. By generating and placing four very weak traps first, the membrane handles all responded to the increased beam power simultaneously.

Once a PM is trapped the arrangement of traps is "locked", with any subsequent movements of the traps affecting the structure as a whole. In this way the position and orientation of the PM is fully characterised by a unit-vector in three-dimensions. The origin of the vector is taken to the current position of the centre-of-mass of the PM, while the direction of the vector specifies the PM's orientation. Defining the PM's position in this way is very convenient as it reduces all movements of the PM to simple mathematical vector operations. This formalism gave the user had complete control over the translation, pitch, yaw, and roll of the PM

For the majority of the time PM were manipulated manually by altering the values of various controls on the LabView GUI. However, due to the precise nature with which the membrane could be controlled, functionality was added to the programme to allow the PM to be controlled via an
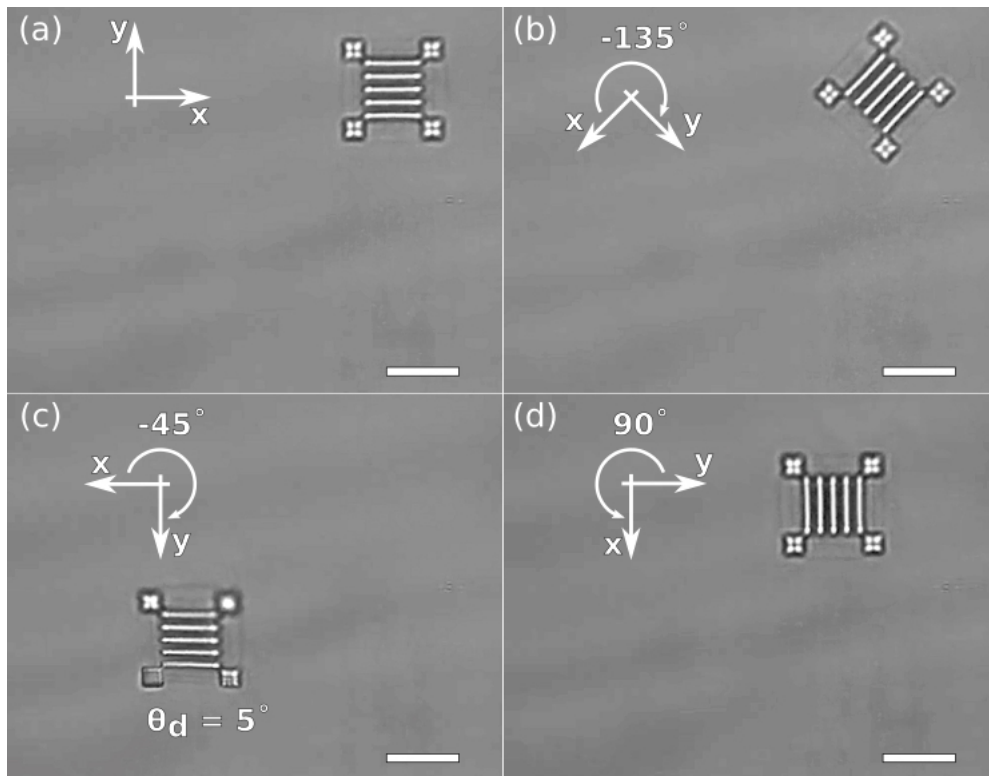
Figure 5.3: Key frames from a movement sequence of a photonic membrane. (a) Membrane starts with a default orientation, before (b) being rotated through 135°. (c) The membrane is then translated and tilted out of the focal plane of the microscope. This orientation is maintained while the membrane is rotated through a further 45°. (d) The membrane is returned to its default orientation and translated and rotated simultaneously.

automated sequence of instructions. Key frames from such a sequence are shown in figure 5.3. Panel 5.3 (a) shows the default position of a membrane which is subsequently (b) rotated on the spot through 135°. From here it is translated through the sample where (c) it is tilted out of focal-plane by approximately 5°, and held in this orientation as it is rotated in the focal-plane through a further 45°. Finally, (d) it is returned to a "flat" orientation, translated through the sample once more, and rotated by 90°.

5.2.2 Performance of optical tweezers system

To determine how well trapped an object is in an optical tweezers trap, the most commonly used metric is trap stiffness.

Initially the trap stiffness of the system was found by using a COM tracking algorithm, in conjunction with the equipartition model method, as detailed in chapter 4. By tracking the motion of each of the PM handles over hundreds of video frames, one can build up statistics on their behaviour in the form of histograms. These histograms are fitted to a Gaussian distribution, with the variance in the Gaussian fit being related to the trap stiffness of the trap. The trap stiffness of the handles is then averaged to give a single trap stiffness, with the trap stiffnesses in the x- and y-directions also being averaged over. This is repeated at several laser powers, and a resultant plot of power versus trap stiffness should reveal a straight-line dependence between the two.

(a)

(b)
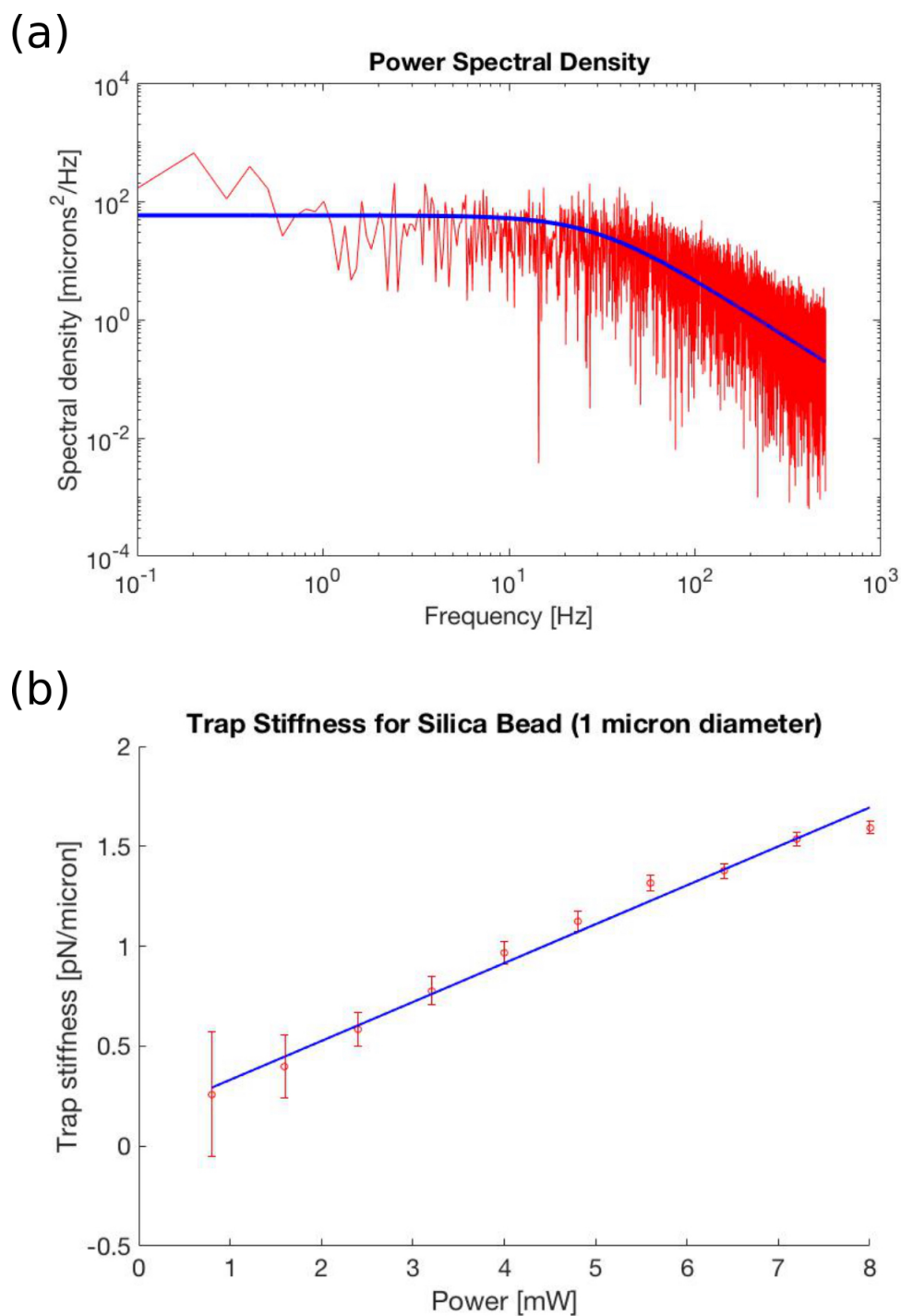
Figure 5.4: Performance of the optical trapping system. (a) Typical plot of the power spectral density of a trapped silica bead (diameter 1 µm). The data is fitted to a one-sided Lorentzian, shown in blue, with trap stiffness being calculated from the corner frequency of the fit. (b) Trap stiffness for the same bead, as a function of trapping power.

However, this approach suffered due to the susceptibility of the tracking algorithm to changes in the scattering from the trapped membrane. Because the algorithm is based on finding the COM of the trapped handles, small changes in the lighting conditions can be interpreted as movements in the membrane. This effect is most prominent when the lighting conditions on the handles are very close to the intensity thresholding values described in chapter 4. Fluctuations in the light intensity can cause the algorithm to recalculate the COM of a handle up to 2 µm away from where it actually is, and when the behaviour of the COM is analysed it seems as though it has been moving large distances. The algorithm assumes this motion to be part of the expected oscillatory behaviour of a trapped particle, and so it attributes a trap stiffness value to that handle that is lower than it realistically should be.

If this approach to tracking is chosen, then the importance of using appropriate lighting conditions must be taken into account. Although the tracking algorithm does allow the user to perform thresholding procedures, it is greatly beneficial to optimise the experimental conditions before any data is acquired.

An alternate method of retrieving the trap stiffness, employed later in my PhD, was to calculate the power spectrum of the object being trapped, as outlined in chapter 4. Figure 5.4(a) shows a typical power spectrum (shown in red) for the case of a 1 µm diameter bead. The power spectrum is level up until the corner frequency, f_c, where it then falls off as f^{-2}. The corner frequency can be ascertained by fitting a one-sided Lornetzian (blue) to the data. From the retrieved values of the corner frequency, one can then calculate the trap stiffness as $k = 2\pi\gamma f_c$, where γ is the viscous drag coefficient for the bead. Figure 5.4(b) shows a plot of trap stiffness versus power for the 1 µm diameter bead, where the data has been fitted to a straight line.

The trap stiffness for trapped bead was $(0.24 \pm 0.03)\,\text{pN}\,\text{µm}^{-1}\,\text{mW}^{-1}$. Trap stiffnesses on this order of magnitude are generally expected, making this system comparable to most state-of-the-art systems.

By adhering the same sort of bead onto the middle of a PM, and using it as a tracker, it was also possible to accurately record the movement of a trapped PM. However, it is not possible to determine a trap stiffness value for the PM as it lies beneath the detection limit of our system. Instead, our approach is to characterise its behaviour via its Brownian motion. This is part of an ongoing study, and is being written-up for publication.

5.2.3 Flexibility of photonic membrane

As outlined above, the properties of PM were probed further by studying their flexibility. While PM made on the macroscopic scale are highly flexible, microscopic PM are difficult to bend. This is in part due to the way the physical properties of a PM scale with size, and in part due to the limited forces one can exert on an object when light is used for actuation.

To understand this difference in behaviour it is helpful to consider the flexural rigidity, D, of a membrane:

$$D = \frac{Eh_e^3}{12(1 - \nu^2)},$$ (5.1)

where E is the Young's modulus of the material, h_e is the elastic thickness of the membrane, and ν is the material's Poisson ratio. The flexural rigidity of a membrane is defined as the force-pair needed in order to bend the membrane to a unit curvature. In other words, it indicates how resistant a membrane is to bending. Equation (5.1) indicates that the thinner a membrane is, the more flexible it becomes. Also, the lower the Young's modulus of the membrane is, the more flexible the membrane will be.

Because the PM used here were 90 nm thin, making them thinner is challenging from a fabricational perspective. For this reason, increasing PM flexibility by altering membrane thickness was
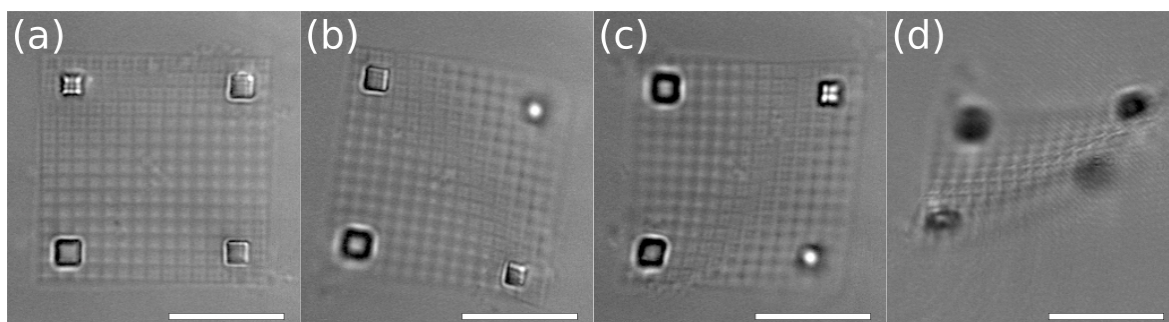
Figure 5.5: Flexibility of a meshed PM. (a) PM held level, with all traps in the same focal plane. (b–d) Deformations can be induced in the PM by altering the focal depth of the various trapped handles. Scale bars represent distance of 10 μm.

ruled out. In contrast, the alternative approach of reducing the Young's modulus of the PM seems to suggest a change in material is required (Young's modulus strictly being a property of the material used). Although PM could be made from other materials, SU-8 is an ideal choice for our fabrication protocol. The solution to this problem was to alter the PM structure itself, by patterning it as a mesh rather than a solid membrane. This reduced the *effective* Young's modulus of the membrane, as there was less material in the membrane that had to be bent.

To test the flexibility of these meshed PM they were trapped and then twisted by displacing the membrane handles in the z-direction by different amounts (figure 5.5). Various surface deformations could be imparted onto the PM in this fashion, although the output was not particularly controllable. The most extreme deformations were induced when two opposite handles were trapped, while a third beam was scanned across the surface of the PM between the two remaining corners. In addition to making the PM more flexible, the meshed structure also meant that deformations were easier to see.

5.3 Discussion

The fine control over the position and orientation of PM demonstrated here represents a significant advancement in the field of optical manipulation. Although other membrane-like structures have been manipulated via optical tweezers (most notably perhaps by Oehrlein [90]), the manipulation of a PM has additional value in that they can be used as extremely versatile tools. The fact that the trapping handles are directly defined within the PM means that control of the membrane is more responsive and precise than would be the case if spherical beads were adhered to the membrane via DNA tethers, for example. It is this finer level of control that allows more complex movements to be performed reliably - a notable example being the out-of-plane rotations demonstrated in figure 5.3 (c).

Having complete 6DOF control over structures is an increasingly important capability for an optical tweezers system to have, particularly because of the increasing number of microscopic tools being developed at the moment. Combining 6DOF control with an automated control routine is extremely powerful, particularly in light of the growing interest in microrobotics. The capabilities of the system could easily be expanded to incorporate elements of machine vision, for example. One can imagine the impact such a system could have in the area of biophotonics. Given a sample with an array of particles in it, particle positions could be automatically extracted and fed into a "flight path" for a PM. A PM could then be trapped and made to follow this flight path, stopping over each particle for a predefined amount of time. While stationary over a particle, certain diagnoses could

be made, e.g. Raman spectra could be taken from the particle with the PM giving enhancement in the optical signal. There is similarly no reason why "swarms" of PM could not be operated simultaneously, the only practical limitation being the available optical power in the trapping beams.

Some fundamental limitations of the system cannot be avoided, however. The range of depths over which one can generate two distinct traps is limited by the objective lens. Specifically, the higher the NA of the lens, the shallower this focal range is. If one tries to trap beyond this limit, the spherical aberrations introduced into the beam degrade the trap quality so much that trapping becomes impossible. One solution is to use a lens with a lower NA, but this has the draw back that lower NA lenses make weaker optical traps. One potential circumvention of this problem could be to use a counter-propagating-beam geometry for the trapping system. This relaxes the condition of needing high NA lenses for stable trapping, and yet offers a larger range or depths over which trapping can occur. This would, however, require a remodelling of experimental apparatus. An alternative approach is to combat the problem through structure-mediated design. By replacing cubic handles with rod-like handles one can cause PM to flip orientation via 90° when the handles are trapped. The most versatile PM designs would likely include both cubic and cylindrical handles.

Handle design could also be useful in improving the stability with which PM are trapped too. Ultimately optical trapping is a scattering problem, with the forces imparted onto the particle from the light being dependant on the shape of particle and the condition of the light. The cubic handles shown in this thesis are probably sub-optimal, even when one takes into account the fabricational limitations of EBL. Optical manipulation of PM would benefit greatly from a study of how trapping strength varied as a function of particle size and shape. This could be achieved by calculating the T-matrix [158]–[160] of various shapes of particle and modelling their behaviour in the optical trap one was using. Genetic algorithms may be useful in this regard, as a starting set of handle designs could be defined which would improve with each iteration of the programme. Addressing the particle properties as well as the properties of the beam is also in line with contemporary "holistic" approaches to optical trapping.

Outside of handle optimisation (see appendix A), the performance of the HOT system also could be improved. The most straightforward approach is to use the SLM to correct spherical aberrations in the system. This procedure is outlined in full in section 4, and can lead to a threefold increase in the trap stiffness. This work was largely a proof-of-principle study, and so maximising trap stiffness was not of primary concern. The data shown in figure 5.4 presents the trap stiffness for PM and polystyrene (PS) beads, measured on the same system, so that their performances may be directly compared. With that being said, improved trap stiffness (in absolute terms) would be beneficial as it allows greater forces to be imparted onto a PM before it falls out of the traps. This is particularly important in relation to the studies on membrane flexibility, which are currently limited by the bending force we can apply to the PM.

Control over the flexibility of PM is crucially important for any application that involves wrapping the PM around a target object (figure 5.1). At present the control one can exert over a membrane's flexibility is rather limited. Although it possible to impart deformations into the PM, this relies on using the scattering force of a scanned beam to impart "kicks" onto different points on its surface. Far more useful would be the ability to hold a PM by its four handles and impart quantifiable deformations through the application of constant forces. Two approaches to obtaining this level of control would be to either focus on improving the trap stiffness, or to focus on making PM more flexible.

The former approach has largely been discussed already and would involve things like wavefront correction of the trapping beam, increasing the laser power. Two simple alterations to PM design can be made that make them more amenable to bending. The first one is simply to make them larger in their lateral dimension. This increases the distance between adjacent handles which generates a larger force couple on the PM for a given pair of optical forces, as the forces are applied a greater

distance apart (cf equation (5.1)). The second design alteration, outlined above, is to use a meshed membrane rather than a solid one. Not only does this reduce the effective Young's modulus of the PM, but it also reduces the drag force acting on the membrane as it begins to bend.

With precise translational and rotational control over PM having been achieved, the next step in the development of this protocol should be to focus on increased control over the membrane deformability.

5.4 Conclusion

In this chapter we have seen that precise translational and rotational control over PM is achievable, despite PM having aspect ratios in excess of 200. Structure-mediated design, in the form of cubic handles, not only allows the PM to be manipulated in this way but also results in them being trapped with trap stiffness several times higher than are achievable with PS beads. This paves the way toward using PM-based filters or sensors in a microfluidic environment *in situ*. This holds particular interest in the case of cellular SERS, where one can now imagine a PM functionalised to act as a SERS sensor, taking Raman spectra from individual cells. Through the use of automated movements routines this capability can easily be extended, with PM taking a series of such readings across a large ensemble of cells.

The field of microfluidics is particularly exciting at the moment, with sub-fields such as microrobotics starting to gain momentum. Microscopic tools are being developed at an accelerating rate, with the number of proposed applications growing similarly. PM are highly versatile tools, having been used in a range of applications at the macroscopic scale. With the development of a fabrication and manipulation protocol that allows PM to be deployed in a microfluidic environment, they too can now lend their services to this rich and burgeoning field.

Surface enhanced Raman spectroscopy

This chapter outlines the development and application of rigid and flexible substrates used to identify the chemical constituents of a material via SERS. By patterning these substrates with sub-wavelength gold fishnet designs, we are able to acquire quantitative SERS readings; in contrast to most SERS methods which provide only qualitative information. We further show that flexible SERS substrates are capable of taking Raman spectra from materials which have non-planar topologies. This is demonstrated by first creating a "phantom" sample patterned with a "hills and valleys" topology, where the valleys are stained with Rd6G dye. A flexible SERS substrate placed on the phantom is able to detect the Rd6G in the valleys because it can conform to the undulating surface.

The chapter begins with the history and underlying physics of Raman spectroscopy and SERS before outlining the fabrication procedure for rigid and flexible substrates. Typical SERS spectra collected with the rigid substrate are shown, followed by the key result of the chapter: using a flexible substrate to acquire the SERS spectrum of Rd6G from an object that has non-planar topology.

The chapter concludes with a discussion on the impact of this work has to the field of Raman spectroscopy, and biophotonics more generally.

6.1 Introduction

Raman spectroscopy is a powerful, label-free, optical technique used to identify molecules by measuring their vibrational spectra [161], [162]. Surface-enhanced Raman spectroscopy increases the utility of Raman spectroscopy by introducing metallic particles or objects into the system being measured. Plasmonic resonances in the metal lead to an enhancement of Raman signal, thereby reducing the time required to take a spectrum. Being label-free techniques, both Raman spectroscopy and SERS are used extensively in biological environments, however they are somewhat limited by their qualitative nature.

This work is driven by the desire to make Raman spectroscopy more quantitative. Obtaining quantitative information on a material's chemical make-up would enable more studies, e.g. to track the concentration of a chemical with time, or to assess how the relative abundance of multi-component mixtures affects cellular function. Furthermore, by making SERS substrates flexible we move closer to the ultimate goal of this research: to wrap a SERS substrate around a cell and take quantitative chemical readings from it.

6.1.1 Raman spectroscopy

When light interacts with a molecule, the photons can either pass through unchanged, or be either absorbed or scattered from it. In these latter two cases, information about the molecule can be gained
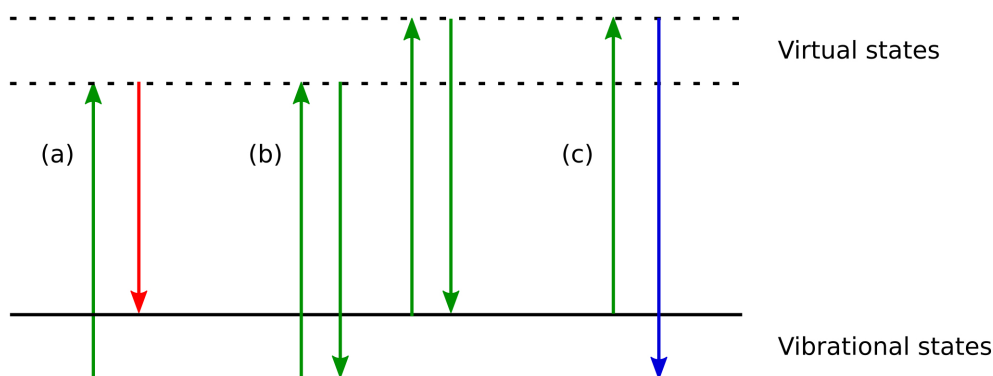
Figure 6.1: Jablonski diagram showing three fundamental scattering processes, namely (a) Stokes scattering, (b) Rayleigh scattering, and (c) anti-Stokes scattering. Rayleigh scattering is bar far the most dominant, and is elastic in nature, while both Stokes and anti-Stokes are inelastic scattering processes. In Stokes scattering the scattered photon has less energy than the incident photon, while in anti-Stokes scattering the opposite is true. In this thesis, Raman spectroscopy was performed using the Stokes scattered photons.

by capturing these scattered photons. Spectroscopic techniques which achieve this are, respectively, IR absorption spectroscopy and Raman spectroscopy. Both of these techniques aim to determine the structure of a molecule by detecting its vibrational modes, yet the underlying physics is different in each case. These two techniques are viewed as being complementary, and are often utilised in parallel.

In IR absorption spectroscopy, a broad range of wavelengths passes through a molecule and is subsequently collected by a spectrometer. Any photons in the beam that carry an energy equal to a vibrational transition in the molecule can be absorbed, and this absorption is observed as a dip in the collected spectrum. In contrast, Raman spectroscopy uses a single wavelength of light and it is photons which are scattered from the molecule that are measured. These scattered photons undergo a change in energy equal to one vibrational unit of energy.

Choice of spectroscopy technique is dictated by the specific molecules one wishes to detect. Most vibrational modes that give a strong signal with one of these techniques will give low-to-no signal using the other. Raman spectroscopy was chosen for this work as it lends itself well to plasmonic enhancement, in addition to the fact that the molecules of interest to us give strong Raman signals. Below is a short review of the underlying physical processes at work in Raman spectroscopy.

6.1.1.1 Scattering processes

We can gain a good understanding of Raman spectroscopy by considering how photons from an incident laser are scattered by a molecule. The incident light polarises the electron cloud surrounding the nuclei in the molecule, forming a short-lived "virtual state". Virtual states are unstable, and so the process of photon absorption and re-emission is almost instantaneous. This process is commonly described as "scattering".

Because electrons are so light, very little energy is required to distort (polarise) the electron cloud. As a result, photons typically experience negligible changes in energy (and frequency) as they are scattered, i.e. they are scattered *elastically*. Elastic scattering, or Rayleigh scattering, is the dominant scattering pathway for photons incident on a molecule. In some instances nuclear motion can be

induced by incident light in which case energy is exchanged between the photon and and molecule. This *inelastic* scattering is known as "Stokes scattering", and was first postulated by Smekal in 1923 [163] and subsequently observed experimentally by Raman and Krishan in 1928 [164]. It is these Stokes scattered photons which are measured in Raman spectroscopy.

Each of these scattering processes can be represented in a Jablonski diagram, as shown in figure 6.1. Figure 6.1(b) shows two Rayleigh scattering processes, whereby the electron before and after scattering resides in the same vibrational state. When photons are scattered inelastically, the electron can end up in a higher energy state (6.1(a)) or a lower energy state (6.1(c)) than the state it started in. These photons are known as Stokes scattered and anti-Stokes scattered, respectively.

Although both Stokes and anti-Stokes scattering are possible, Stokes scattering occurs far more frequently than anti-Stokes. This is because anti-Stokes scattered photons need to interact with electrons that are in excited energy states. It is clear from a thermodynamical perspective that these excited electrons occur far less frequently than electrons residing in the energetically preferred ground state. This thesis considers only Stokes-scattering-based Raman spectroscopy and, as is common, uses the terms "Stokes scattering" and "Raman scattering" interchangeably.

6.1.1.2 Molecular vibrations

Figure 6.2 shows a typical Raman spectrum for ethanol. Each peak in the spectrum is attributable to a particular molecular vibration of the ethanol molecule, with these peaks being superimposed on a background signal that is mainly due to fluorescence. The y-axis values used are somewhat arbitrary, as the only important quantity is the photon count i.e. how many photons at each wavelength are incident on the detector. It is standard in spectroscopy to identify photons by their wavenumber, $\bar{\nu}$, rather than their wavelength, λ. This is largely due to convention, since wavenumber, with units of cm^{-1}, can be a convenient choice as it is directly proportional to the energy of each photon. Wavelength and wave number are of course related by:

$$\bar{\nu} = \frac{1}{\lambda} \tag{6.1}$$

The values of wavenumber that are quoted in a Raman spectrum are not usually the absolute values of the collected photons. Instead they represent the shift in wavenumber of the scattered photons, i.e. the difference in wavenumber between the incident photon and the photon after it has been scattered from the molecule.

To interpret a Raman spectrum a spectroscopist notes which peaks are present (often the relative height of certain peaks are taken into account also) and attempts to attribute them to a particular vibrational mode. This is usually done with the aide of look-up tables. Certain wavenumber ranges are known to be "home" to certain families of vibrations [165], some of which are outlined in table 6.1. The fingerprint region is so-named because the Raman spectrum in this region is primarily used to identify the molecule. The band assignment for ethanol, in the fingerprint region, is shown in table 6.2.

Band [cm^{-1}]	Assignment	Examples
< 1500	Fingerprint region	Complex C - C , C - N vibrations
1500 - 2000	Double-bond region	- C = O
2000 - 2500	Multiple-bond region	- N = C = O
2500 - 4000	Single-bond region	X - H

Table 6.1: Raman bands for typical molecular bonds.
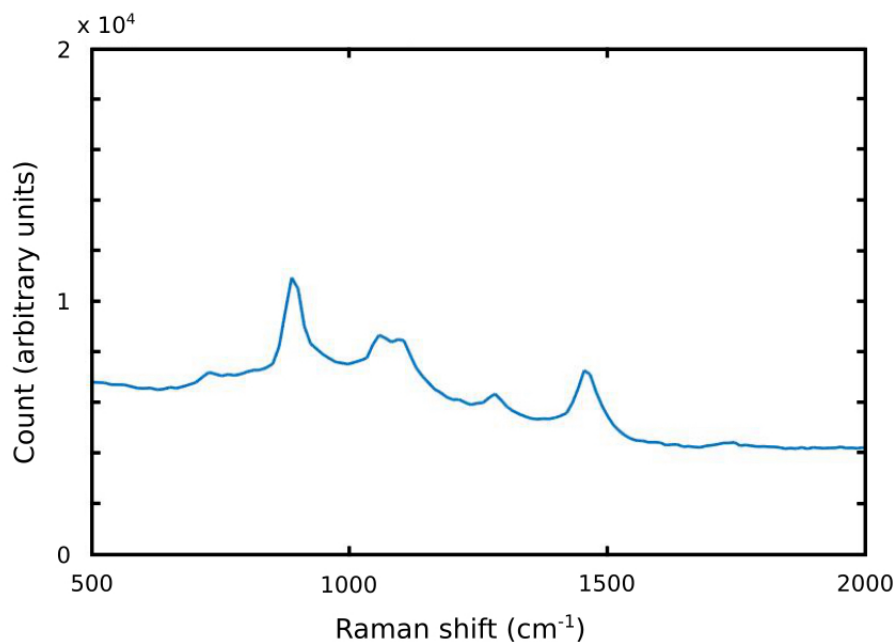
Figure 6.2: Raman spectrum for ethanol. Raman spectra are acquired by counting the number of photons that arrive at the detector with a particular wavenumber shift compared to the exciting beam. A relatively simple molecule, ethanol was used to calibrate the SERS system.

6.1.2 Surface-enhanced Raman spectroscopy

One of the disadvantages of Raman spectroscopy is that Stokes scattering is a spontaneous process, whereby only one in every 10^6 - 10^8 photons scattering this way. As a result, the Raman-scattering cross-section of molecules is incredibly small - between $10^{-25}\,cm^2$ and $10^{-30}\,cm^2$. This means that Raman signals are very weak (especially when compared to the light that is Rayleigh-scattered), and can often be obscured by background fluorescence. One solution to this issue is to collect photons over a longer period of time (acquisition time), giving the detector a chance to register enough Raman-scattered photons to build-up a representative Raman spectrum. When the technique was first used, acquisition times in excess of 100 h were needed in order to obtain a single spectrum [162]. Increasing the signal obtained during Raman spectroscopy has been a major driver of research in the field.

Band [cm^{-1}]	Assignment	Bond structure
886	C-C stretch	
1056	C-O stretch	
1116	CH_3 rock	H H
1280	CH_2 torsion	H – C – C – O – H
1456	CH_3 and CH_2 bend	
1486	CH_3 bend	H H

Table 6.2: The Raman band assignment of ethanol [166], [167].

The power of the Raman-scattered photons, S_R, for a particular wavelength, λ_{ex}, varies as

$$S_R(\lambda_{Raman}) \propto N\sigma_R I(\lambda_{ex}), \tag{6.2}$$

where N is the number of molecules in the sample, σ_R is the Raman cross-section of the molecule, and $I(\lambda_{ex})$ is the wavelength-dependant intensity of the excitation laser.

To increase the signal one could in principle either try to increase N, σ_R, or I. However, there are practical limitations which limit the enhancement in signal one can achieve in this manner. N is typically set by the condition of the chemical or analyte one wishes to identify, and is therefore not a variable the user can typically change. Conversely, I can easily be increased, but will potentially lead to sample degradation before appreciable increases in S_R can be achieved. The only viable option is to increase the Raman cross-section, σ_R.

One can model the Raman cross-section as an incident photon which creates a phonon and a secondary, less energetic photon [168], [169]. The Raman cross-section is then given by:

$$\sigma_R = \left(\frac{1}{\lambda}\right)^4 \times f(T) \times L \times R(\lambda_{ex}, \lambda_{Raman}), \tag{6.3}$$

where $f(T)$ is the probability that the molecule is in a particular state, L is the local electric field factor, and $R(\lambda_{ex}, \lambda_{Raman})$ are matrix elements defining the overlaps in a Hamiltonian, and the initial and potential end states.

In this thesis, the Raman cross-section was improved by using SERS to increase the local field factor, L. This effect was discovered by accident when it was observed that the signal for pyridine was greatly enhanced when the pyridine was first adsorbed onto the surface of a roughened silver electrode [170].

The local field factor is given by:

$$L = |\mathbf{E}(\lambda_{ex})|^2 |\mathbf{E}(\lambda_{Raman})|^2, \tag{6.4}$$

where the electric fields $\mathbf{E}(\lambda_{ex})$ and $\mathbf{E}(\lambda_{Raman})$ are taken at the location of the scattering molecule.

Provided one has a broad enough resonance for enhancement with a small Raman shift, i.e $\lambda_{Raman} \approx \lambda_{ex}$, one can assume that the local field factor scales with the forth power of the electric field:

$$L = |\mathbf{E}|^4, \tag{6.5}$$

showing the potential massive potential for optical enhancement.

A more rigorous treatment accounts for the fact that the SERS enhancement factor, G, defined as the ratio of the signal in a SERS experiment to the signal obtained in a Raman measurement where no enhancement from metals was present, is attributable to two factors [171]:

$$G = EF(\lambda_{ex}) \times EF(\lambda_{Raman}) = \frac{|\mathbf{E}_{struct}(\lambda_{ex})|^2 |\mathbf{E}_{struct}(\lambda_{Raman})|^2}{|\mathbf{E}_i(\lambda_{ex})|^2 |\mathbf{E}_i(\lambda_{Raman})|^2}. \tag{6.6}$$

These two SERS enhancement factors are known as the local field factor, also known as the EM effect, and the chemical effect. The chemical effect arises from the electrochemical bonding of the molecule to the surface of the metal, and typically grants an enhancement factor of no more than 100 [172]. In addition, it can have the adverse affect of shifting the relative heights of the Raman peaks [173]. In contrast, the EM effect is capable of providing enhancement that is many orders of magnitude higher than this, and although SERS enhancement cannot be solely contributed to the EM effect, it does seem to provide the dominant contribution [174].

In this thesis any enhancement of the Raman signal is assumed to have originated from the EM effect. Typical SERS enhancement factors are on the order of 1×10^4 to 1×10^8 [175] although higher values are possible. Enhancement factors as high as 1×10^{15}, have been achieved, allowing SERS signals to be collected from single molecules [176].

6.1.3 Motivation - flexible SERS

Most substrates made for SERS are rigid, however some flexible SERS substrates are beginning to come into use, with early examples were structures fabricated onto polydimethylsiloxane (PDMS) blocks or on aluminium foil [177]–[180]. In these cases the flexibility of the substrates was not actually utilised, as the focus of the work was on making cheap, disposable SERS substrates.

There have been several demonstrations of flexible SERS substrates which do capitalise on their flexibility. Microfluidic SERS systems can benefit from flexible substrates as they make delivery of molecules to the SERS sensor easier [181]. At the other end of the scale, sandpaper covered in silver can act as simple and cheap flexible SERS substrate. These are durable enough to swab and detect pesticides directly from fruit [182]. Another advantage of flexible substrates is their tunability, whereby the plasmonic resonance of the substrate can be altered simply be stretching it [183], [184].

The interest in SERS in this thesis is to create a flexible SERS substrate capable of being wrapped around an object with near-arbitrary topology. The motivation for this is to allow SERS readings to be taken directly from individual particles or cells either *in vitro* or *in vivo*. With such a substrate, the aim is then to generate a spatially-resolved map of the cell or particle's chemistry.

An intermediate step toward the cell-wrapping concept was performed, in which a polymeric "phantom" was created to act as a stand-in for a genuine biological sample. The phantom was patterned with ridges which were doped with Rd6G, and a flexible SERS substrate was used to see if the doped regions could be detected. Having previously designed the phantom, it was then possible to compare the results of the SERS reading to see how well the doped regions had been mapped.

6.2 Methods

This section gives a brief outline of the fabrication of rigid and flexible SERS substrates, as well as the biological phantoms. The optical system used is also discussed.

6.2.1 SERS substrates

Using the same fabrication procedure outlined in chapter 3, flexible SERS substrates were made using an SU-8 photoresist to both define the membrane itself, and to act as a mask for the patterning of the gold fishnet pattern. The membranes discussed in this chapter are 1 μm thick, making them both flexible and robust. Using membranes of this thickness also helped to reduce fluorescence from the SU-8. The flexible SERS membranes were approximately 5 cm in side length, and were patterned with a gold fishnet design that was 7 mm by 7 mm in size. The fishnet period was 400 nm, with wire widths of 90 nm. The thickness of the gold was 40 nm.

The fishnet pattern was employed because it is a simple, repeating pattern with four-fold rotational symmetry. The high regularity in the design grants reproducibility in the SERS signal gathered, both in terms of measurements made at the same point at different times and also across different locations on the membrane's surface. This reproducibility is further enhanced when one considers that the simplicity of the design minimises any machine errors in reproducing it many times. The rotational symmetry of the fishnet allows it to operate irrespective of the polarisation of the light, which allows the membranes to utilise all of the light from the unpolarised excitation source used in the SERS experiments. The detection limit of such substrates is concentrations on the order of 10 nM [105].

Rigid SERS substrates were also fabricated, based on the same gold fishnet design outlined above. These substrates were made from glass, and instead of having a single fishnet covering a large area they had nine smaller fishnet areas, spaced in a 3×3 grid.
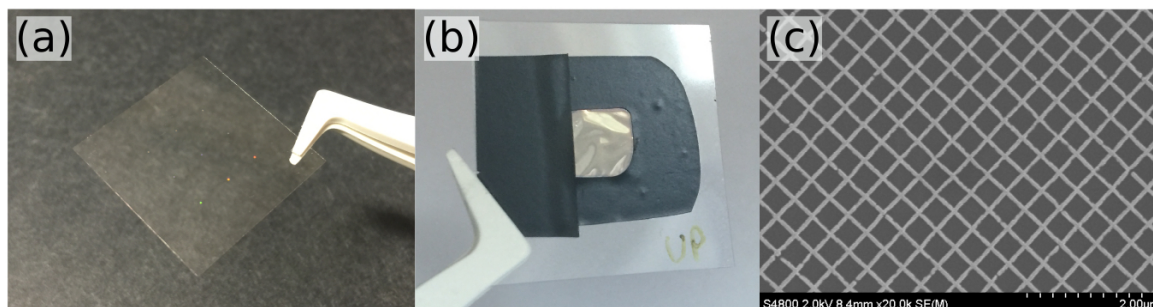
Figure 6.3: SERS substrates used in this work. (a) Solid SERS substrates were patterned with nine gold fishnet pads, while (b) flexible SERS substrates were completely covered in the gold fishnet. (c) SEM image of the fishnet design used in both cases.

6.2.2 Optical setup and calibration

The optical setup used for the SERS experiments consisted of an excitation laser (a Gem 532 from Laser Quantum), operating at 532 nm, integrated into a standard optical microscope (a Nikon Ti-Eclipse), see figure 6.4. The laser entered the microscope through one of the rear ports where it was directed upwards and focussed onto the sample by the objective lens. A wavelength of 532 nm was chosen over longer wavelength choices because the Raman cross-section scales as $1/\lambda^4$. The laser had a narrow bandwidth, on the order of 0.1 nm, which allowed high-precision measurements to be taken. Narrow bandwidth sources are important for Raman spectroscopy, as the width of the measured peaks is a convolution of their true width and the line width of the source used.

A variable neutral density (ND) filter placed immediately after the output of the laser allowed the power of the excitation beam to be controlled. This could be used to perform low intensity measurements without the need to reduce laser currents to potentially unstable levels.

The sample was illuminated from above using the microscope's integrated white-light source, and imaged onto the camera by the same objective lens used for focussing the Raman laser. This allows the user to see where SERS measurements are being taken from, although the illumination source must be turned off during the SERS acquisition itself.

Two different objective lenses were used depending on the particular experiment being carried out. In general, higher NA objectives are desirable as they will confine the light to a smaller focal volume and lead to a higher SERS signal. When rigid SERS substrates were used, a Nikon 100× oil-immersion objective with a NA of 1.3 was utilised. Conversely, when flexible SERS substrates were used, a Mitutoyo 100× objective with a NA of 0.7 had to be chosen. This change in objective lens was necessary because high-NA objectives are constrained by incredibly short working distances (The Nikon objective used in this thesis had a working distance of 0.16 mm compared to 6 mm for the Mitutoyo). For flexible substrates, which are designed to follow the surface structure of the objects they are placed on, it is important to use an objective lens that has a long working distance and a large depth of field in order to insure that the whole membrane stays in focus.

The Raman signal was collected by a 200 μm diameter multimode fibre and passed on to an Andor spectrometer. Immediately prior to entering the spectrometer the light was passed through a notch filter which transmitted the signal but reflected the 532 nm pump light. This meant that the pump light could not drown out the (much weaker) Raman signal. The CCD embedded in the spectrometer was cooled to −70 °C to reduce the noise which arises from the dark current, i.e. the current which flows in the CCD when there is no light present.

The set-up was typically calibrated by taking the Raman spectrum of ethanol (fig. 6.2). Acquisition
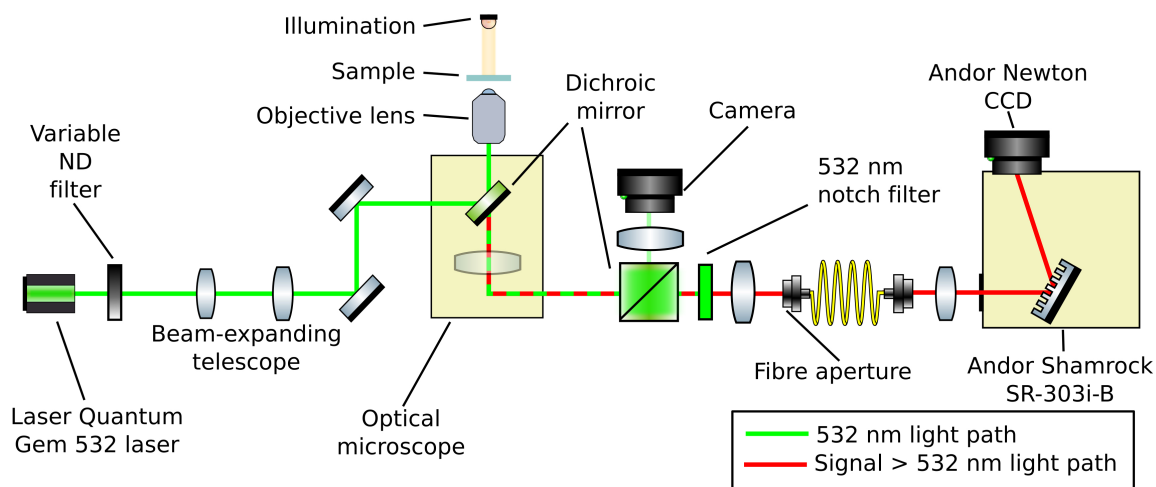
Figure 6.4: The SERS system used in this thesis. A 532 nm laser is focussed onto the sample using a high NA objective lens. The scattered Raman signal is collected by via an optical fibre and sent to the spectrometer. The addition of a dichroic mirror and a camera allows the user to image the sample to see if the Raman laser is being focussed onto the desired area. Image adapted from one by Peter Reader-Harris, using ComponentLibrary [124].

of a recognisable spectrum was taken as an indication that the setup was working well. If no such spectrum was obtained, or the strength seemed low, the set-up was realigned as required.

6.2.3 Continuous wavelet transformation method

Typical Raman spectra appear as Raman peaks superimposed upon a fluorescent background. In order to extract the Raman peaks, we use a continuous wavelet transform (CWT) method which involves measuring the cross-correlation between the spectrum and a chosen wavelet at all spectral positions in the Raman signal [185], [186]. This method is effective because Raman peaks are typically very sharp, whereas background fluorescence is a relatively flat and slowly-varying signal. CWT also has the advantage that no information about the sample is needed. This is not the case, for example, if the background is removed by subtracting a pre-recorded baseline correction. Using baseline corrections is appropriate when one has a reference sample to work with, however, the unknown surface curvature of a flexible SERS substrate would make obtaining such a reference sample effectively impossible.

The CWT can be defined mathematically as:

$$C(a,b) = \frac{1}{\sqrt{a}} \int_{-\infty}^{\infty} x(t)\psi^*\left(\frac{t-b}{a}\right) \, dt, \tag{6.7}$$

where $x(t)$ is the Raman signal, a is a scale parameter, b is the index parameter, and ψ^* is the complex conjugate of a wavelet function. $C(a,b)$ is then the cross-correlation between the Raman signal and the chosen wavelet, where the wavelet has been scaled by the factor a and displaced along the Raman signal by an amount dictated by b.

The most common choice of wavelet is the "Mexican hat wavelet", depicted in figure 6.5, defined as:

$$\psi(t) = \left(\frac{2}{\sqrt{3}}\pi^{-1/4}\right)\left(1 - t^2\right)e^{-t^2/2}. \tag{6.8}$$
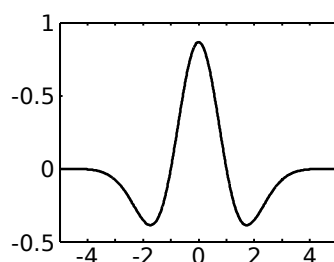
Figure 6.5: Pictorial representation of the "Mexican hat" function which was used for CWT of Raman spectra.

The Mexican hat wavelet is chosen because its Gaussian-like peak correlates well with Raman peaks, while its negative side-bands ensure correlation will be near-zero in regions that are slowly varying, e.g. the background fluorescence signal.

The CWT method was employed in MATLAB, using the `cwtft` command. MATLAB returns a 2-dimensional matrix of CWT coefficients, C, which dimensions (a, b), where a and b are the number of scales and spectral positions over which the cross-correlation is performed. By choosing those CWT coefficients which correspond to the lowest scaling factor (sharpest wavelet peak), one can then extract the spectral positions of the peaks. Alternative methods of locating peaks, such as those that use first and second derivatives of the signal [187], [188], can often alter the positions of some peaks relative to others. The CWT method does not suffer from these disadvantages, and in general does not require any human input regarding additional smoothing or fitting.

6.2.4 Sample preparation

Sample preparation falls into two distinct categories, depending on whether the SERS readings were being taken with a rigid or flexible substrate. The main difference between the two is that with the rigid substrates the analyte is placed on the substrate and allowed to dry, while with the flexible substrates the analyte is present on an object onto which the substrate is then placed.

For rigid substrates, a 2 μl volume of analyte is dropped onto the centre of SERS pads, enough to cover them completely. Because the water is a polar solvent, and because the substrate is hydrophobic, the edges of the droplet become pinned to the substrate and the size of the droplet remains the same as it dries [189]. This is known as the coffee ring effect, and results in a uniform layer of analyte being deposited on the pad while an increased concentration of precipitate is found at the edges of the drop [190]. In these situations the analyte is left to dry for a minimum of 1 h at room temperature prior to a SERS experiment being carried out.

For flexible substrates Rd6G was pipetted into the grooves in the phantom, and the flexible substrate was placed on top. This was then allowed to dry at room temperature for over 1 h after which time the phantom was be placed on the sample holder of the microscope.

6.2.5 Fabrication of biological phantom

The basic design of the phantom was a periodic hills-and-valleys pattern along one direction, surrounded on all sides by an additional ridge. Rd6G was pipetted into the valley sections of the phantom, with the outer ridge preventing any of escaping. Ethanol was used as a solvent as it evaporates much fast than water, allowing experiments to be carried out more quickly.

The first generation of phantoms were made by depositing SU-8 onto a glass substrate. SU-8 2050 was spin-coated to a thickness of 40 μm and baked at 100° for 23 min. The baking temperature was
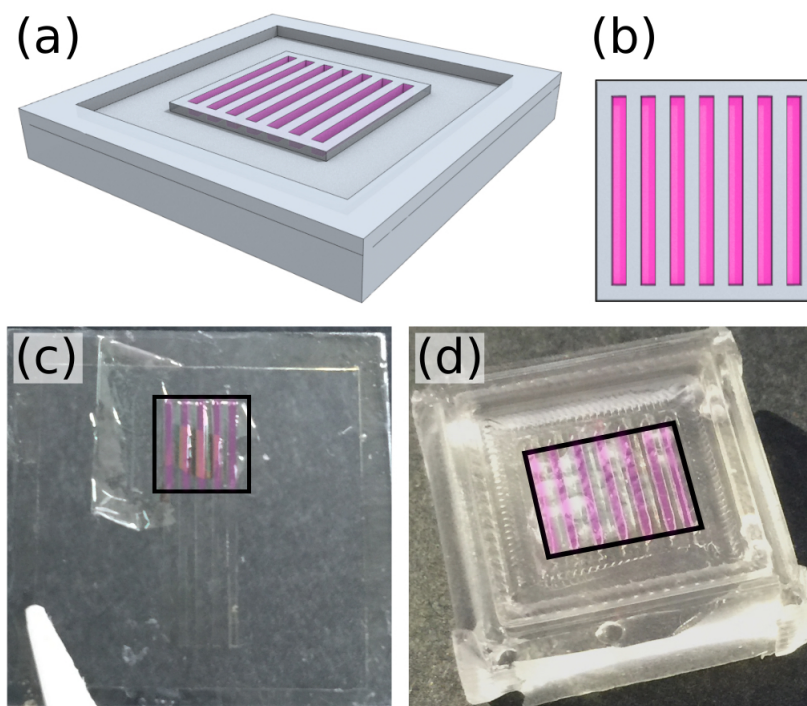
Figure 6.6: (a) Sketch of biological sample used in this thesis, showing the central "hills and valleys" region, doped with Rd6G (shown in pink). (b) Bird's eye view of doped region. (c - d) Typical phantom samples with flexible SERS substrates applied to them. Black square and pink lines added to highlight the doped area. Both (c) glass and SU-8 phantoms and (d) PDMS phantoms were made.

ramped from $65°$ to $100°$ over the first 5 min of baking to ensure that bubbles did not form inside the phantom. A patterning mask, made of Rubylith photo-resistant film (Ulano Corporation), was cut to shape using a Graphtec CE6000-40 cutting plotter. The mask had four rectangular channels cut out of it, each 500 µm wide and spaced by 500 µm. The length of each channel was typically between 6 mm and 8 mm. The sample was then placed in a mask-aligner and exposed with UV light for 12 min, after which the mask was peeled off and the sample was subjected to a post-exposure bake at 100 °C for 25 min. Areas of unexposed SU-8 were developed in EC solvent for 45 s.

Second generation phantoms were made entirely from PDMS, using a SU-8-on-glass stamp. The stamp was made using the same procedure outlined above, the only difference being that the SU-8 was deposited onto the glass as the inverse of the desired hill-and-valleys pattern. The completed stamp was placed into the bottom of a 3-D printed mould, onto which PDMS was poured. PDMS comes in two separate components (base and reagent) which begin to set once they are mixed together. The mixed PDMS (mixing ratio of 5:1 by weight) was poured into the mould and allowed to set overnight at room temperature. To prevent bubbles from forming in the PDMS, the phantom was housed in a desiccator for the duration of the setting process.
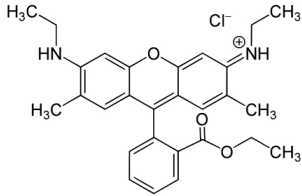
Raman peak [cm^{-1}]	Band assignment	Bond structure
613	in plane and out plane XR deformations	
775	out plane C-H bend; in plane XR deformation	
1184	in plane XR deformation; C-H bend; N-H bend	
1312	in plane XR breathe N-H bend; CH$_2$ wag	
1364	XR stretch; in plane C-H bend	
1512	XR stretch; C-N stretch; C-H bend; N-H bend	
1577	XR stretch; in plane N-H bend	
1651	XR stretch; in plane C-H bend	

Table 6.3: The band assignment for the molecule Rd6G [191].

6.3 Results

To demonstrate that a flexible SERS substrate could conform to an object and provide a map of the chemical compounds found on it, a biological phantom was stained with Rd6G dye. Rd6G was pipetted into the valley regions of the phantom, leaving the hill regions free from dye. A flexible SERS substrate was placed on it, with the Raman signal from the substrate being collected at different points along a linescan.

6.3.1 SERS Spectra of a Macroscopically Curved Material

The glass and SU-8 phantom was prepared by pipetting Rd6G at a concentration of 100 mM into the grooves between the SU-8 ridges. The hydrophobic nature of glass insured that Rd6G spread out quickly and evenly along the length of the channels. The flexible SERS substrate was applied to the sample while the Rd6G was still wet, and the sample was allowed to dry before the readings were taken. The concentration of Rd6G used was not high enough for any Raman signal to be gathered by the system. This meant that Raman peaks could only be detected in areas that had gold in them, their SERS enhancement being large enough to make the signal observable.

The excitation laser was operated at a power of 100 μW, and focussed onto the sample using a Mitutoyo 100× objective lens. Two spectra were taken at 5 μm intervals along the sample, with the laser focus adjusted manually at each point in order to keep the surface of the membrane in focus. The mean of these spectra was the used for analysis. An integration time of 2 s was used.

Figure 6.7 shows the spectra collected at two particular positions on the phantom. The top panel corresponds to a raised section of SU-8, while the bottom panel corresponds to one of the valley regions doped with Rd6G. The colour pink was added to indicate that the spectrum is taken from a doped region. From figure 6.7 one can see that a Raman signal is only obtained in the doped regions, confirming the presence of Rd6G. The green line in both panels marks the location of the Raman peak at 1651 cm^{-1}. The height of this peak was used to indicate the strength of the Raman signal.

The linescan data was analysed using a CWT method which was robust to the highly variable background fluorescent signal from the phantom. Figure 6.8 shows the magnitude of the CWT coefficient corresponding to the 1651 cm^{-1} Raman peak plotted at the sampling points along the linescan. The noise in the measurement was taken to be the standard deviation of the CWT spectrum where no Raman peaks were found, i.e. at wavenumbers in excess of 1800 cm^{-1}. This noise is represented by the error bars shown.

The distinct feature of figure 6.8 is the variation in the height of the 1651 cm^{-1} peak depending on whether it was measured at a peak or valley of the phantom. In valley sections, the peak has an
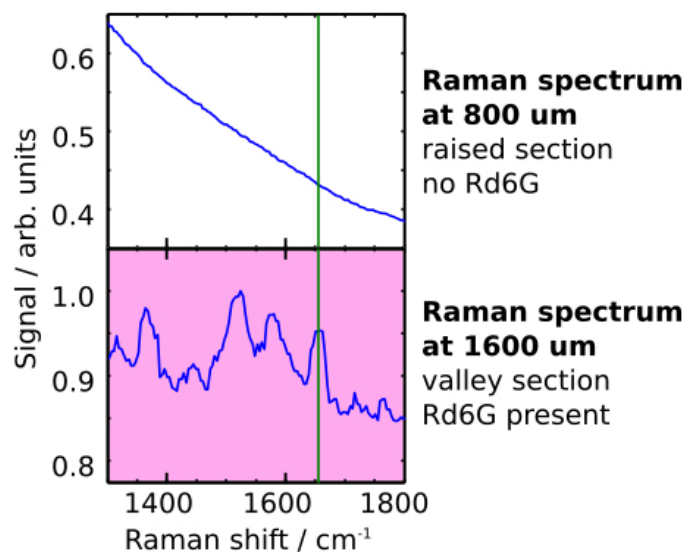
Figure 6.7: Raman spectra acquired during a 2.5 mm linescan of phantom doped with Rd6G. The top panel shows the Raman spectrum of one the SU-8 ridges, while the bottom panel shows the Raman spectrum taken from one of the doped valleys. The Raman peak at $1651\,\mathrm{cm}^{-1}$ (marked by the green line) was taken as an indication of the overall strength in the Raman signal. Pink areas highlight regions where Rd6G is detected.

average value of 45, with a minimal associated error bar. In contrast, the average of the peak size taken from the SU-8 ridges is averaged around 0, and is considerably noisier. This demonstrates that Rd6G was indeed detected to be present in the valleys of the phantom, but not on the ridges.

6.4 Discussion

6.4.1 Data acquisition

A large fluorescent signal is registered from both the SU-8 and the glass substrate. Although the fluorescence was useful as an indicator of where ridges and valleys were located, it is primarily a source of noise in Raman and SERS experiments. To this end, new phantom samples have been made entirely from PDMS, a substance that doesn't exhibit fluorescence. Repeating the linescan experiment with these new phantoms is of great interest, as greater signal-to-noise (SNR) could surely be achieved.

That being said, the fact that these flexible SERS sensors still perform well in the presence of fluorescence is very encouraging. This will likely become evident once they are applied to genuine biological samples, many of which are likely to produce fluorescence. The PDMS phantoms themselves also offer some challenges, most notably in terms of how Rd6G disperses inside the channels. The SU-8 phantoms benefitted from being directly defined on glass - a hydrophobic substrate. This meant that the Rd6G quickly and evenly distributes itself along the length of the channel as it is pipetted in. With PDMS phantoms Rd6G is more inclined to form individual droplets inside the channels, meaning more care has to taken during the pipetting process.

The linescans presented in this thesis were performed at speeds of approximately $1\,\mathrm{\mu m\,s}^{-1}$, meaning that a single series of measurements like those shown in figure 6.8 take on the order of
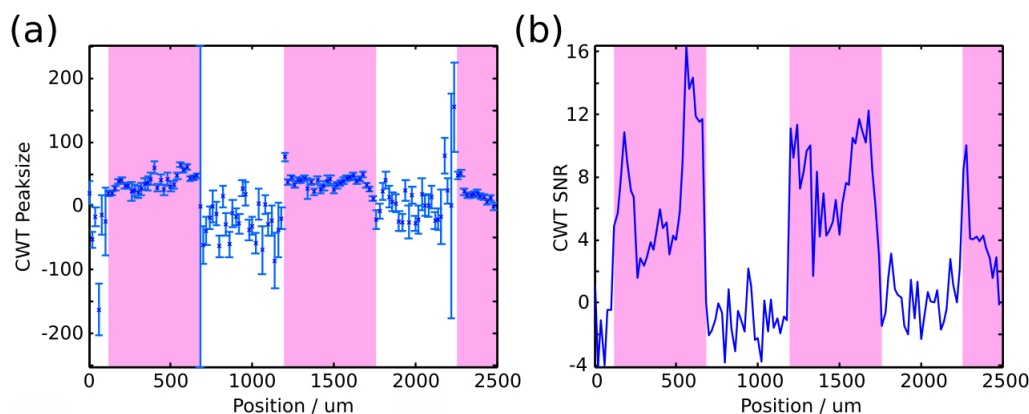
Figure 6.8: (a) The magnitude of the CWT coefficient corresponding to the $1651\,\mathrm{cm}^{-1}$ Raman peak plotted as a function of distance along the linescan. The error bars indicate the variation in spectrum where there are no Raman peaks. Alongside (b) the SNR of the processed spectrum, this indicates Rd6G is successfully identified by the PM. The colour pink is again used to mark the doped valleys.

1 h to acquire. This is particularly time consuming when one considers that the user must remain with the system while measurements are being taken in order to manually optimise the microscope focus at each sampling position. After the stage had moved the 5 µm increment to the next sampling position, the system would wait for 2 s to give the user time for this readjustment. Reducing this waiting time could in principle speed up the process, but at the cost of potentially adversely affecting the quality of the measurements. Alternatively, one could decrease the integration time taken for each measurement. This would involve increasing the laser power to maintain a good signal level, which may lead to damage of the sample. The only other alternative to increase the measurement speed is to sample the object with lower spatial resolution i.e., increase the separation between sampling positions. A larger sampling separation could successfully have been used in our linescan, where the surface being mapped was known in advance to feature relatively large (500 µm) features. However, when this technique is applied to samples with unknown topologies, one would want the sampling resolution to be fine enough to sufficiently probe the surface.

The most significant improvement which could be made to the system would be to use a microscope stage which had auto-focussing capabilities. This would serve to make the entire measuring process automated, although it may also improve measurement speed as less time is needed for refocussing. With an automated system, one would be able to set up a sample, provide the system with a path to take scans along, and let it run. This would be particularly advantageous when it came to generating 2-D maps as opposed to 1-D linescans. Such 2-D mappings would be expected to take many hours to complete.

6.4.2 Data analysis

CWT was used to analyse collected spectra primarily because of its simplicity. It was able to extract peak positions from spectra that had fluorescence backgrounds without requiring any knowledge of the sample's condition. That being said, if one wanted to fully recreate the spectra, minus the background fluorescence, further processing steps would likely be required.

While CWT using a Mexican hat wavelet is good at identifying the positions of peaks, it can often misrepresent peak width. One promising pathway to reproducing faithful spectra would be to

perform a CWT with the Mexican hat wavelet to extract peak positions, and to store these positions. CWT could then be performed again, at spectral positions where peaks are now known to be, using an alternative wavelet. If a Haar wavelet (or similar) is chosen as the second wavelet, one could also determine peak width [185]. By combining the information from both CWT runs, a complete spectrum can be generated.

For the purposes of this thesis, precisely recreating the width of Raman peaks was not a priority. What was important was that peak positions were correctly represented, and that the heights of CWT coefficients were directly linked to the Raman signal strength.

6.5 Conclusion

This chapter has outlined the work I have done with SERS, having used both rigid and flexible substrates. This work has been driven by the desire to use flexible SERS substrates in a biophotonic setting, making use of their conformability to take readings from non-planar objects. As intermediate step towards this goal, we have demonstrated that flexible SERS substrates are capable of obtaining Raman spectra from objects that have curved topologies, using a fabricated "phantom" as a stand in for a genuine biological system.

The next steps for this work should be to apply the current flexible SERS substrates to a biological system, which I can see progressing along two fronts. The first of these would some form of "macroscopic" application, for example the mapping of a fingerprint [192], [193]. SERS has already been used to identify the chemicals present in a fingerprint, but with our technique it would be possible to simultaneously map the fingerprint itself. The second front is microscopic in nature, and would involve incorporating this work with the optical manipulation work outlined in chapter 5. One can imagine using optical tweezers to wrap a flexible SERS substrate around a cell, for example. A Raman spectrum for the cell can be acquired *in vitro*, with the SERS substrate then free to be transported to other cells where further spectra can be collected. Performing experiments on the single-cell level in an *in vitro*, and perhaps eventually an *in vivo*, environment extends the applicability of our substrates into a region which is rich in interest.

Contributions

The SERS system described in this chapter was already available in my group. I analysed the collected spectra using techniques which had previously been used by my group also. I made all the SERS substrates and biological phantoms in the thesis. These samples confirmed and completed the preliminary data that were acquired before I became involved with this project. I am currently writing up a paper for publication in this area.

Further applications: microscopic tools for biophotonics

This chapter outlines several projects which have not yet been brought to firm conclusions. They all fall under the area of "microscopic tools".

The first project I will discus is optically actuated mechanical tweezers. These are made by following a similar fabrication procedure as the PM outlined above, and make use of novel "handle" designs. Their proposed application is for particle sorting in a microfluidic environment.

The second project involves manipulating a PM via optical tweezers, with a view to applying it to a microfluidic environment also. This specific demonstration involves patterning the PM as an optical filter and positioning it over cells or particles. The device is then seen to act as an *in situ* optical filter, and could be used, for example, to quench the fluorescence signal from a cell.

The final project I will be discussing involves the handles that are used in an optical trapping experiment. As mentioned above, we are able to trap PM, and other microtools, through structure-mediated design. That is to say, through informed fabrication protocols which incorporate handles into our design. These handles are either cubic or cuboidal in our applications, although in most of the literature they are spherical. The challenge lies in finding the optimal handle design. To this end, we discuss the use of a genetic algorithm, coupled with the optical tweezers toolbox software by Nieminen et al [194], to deduce which handle geometries provide the greatest trap stiffness based on the T-matrix method. This is outlined in appendix A.

These separate projects all tie in to the same theme and act to strengthen the platform for novel optical manipulation that has been developed in this thesis.

7.1 Microtweezers

Optical sorting has benefited greatly from optical tweezers technology. A range of particles and cells have been manipulated successfully, covering a large range of size and shapes. There are, however, limits to the direct application of optical tweezers to particle sorting.

There are several reasons why optical tweezers may not be an effective technology for particle sorting. These reasons fall into one of two categories: either optical tweezers are not able to trap the particle in question, or they can, but in doing so they would risk damaging the particle.

In the first instance, a particle may not be trappable if its size, shape, or refractive index do not conform with the particular specs of the tweezers system. This is the case for certain refractive indices and shapes, where large enough gradient forces are simply not generated (see figure 7.1). One finds that small particles (where particle diameter is less than $\lambda/4$) are trappable for a large range of refractive indices. As one increases the size of the particle, only those with lower refractive indices
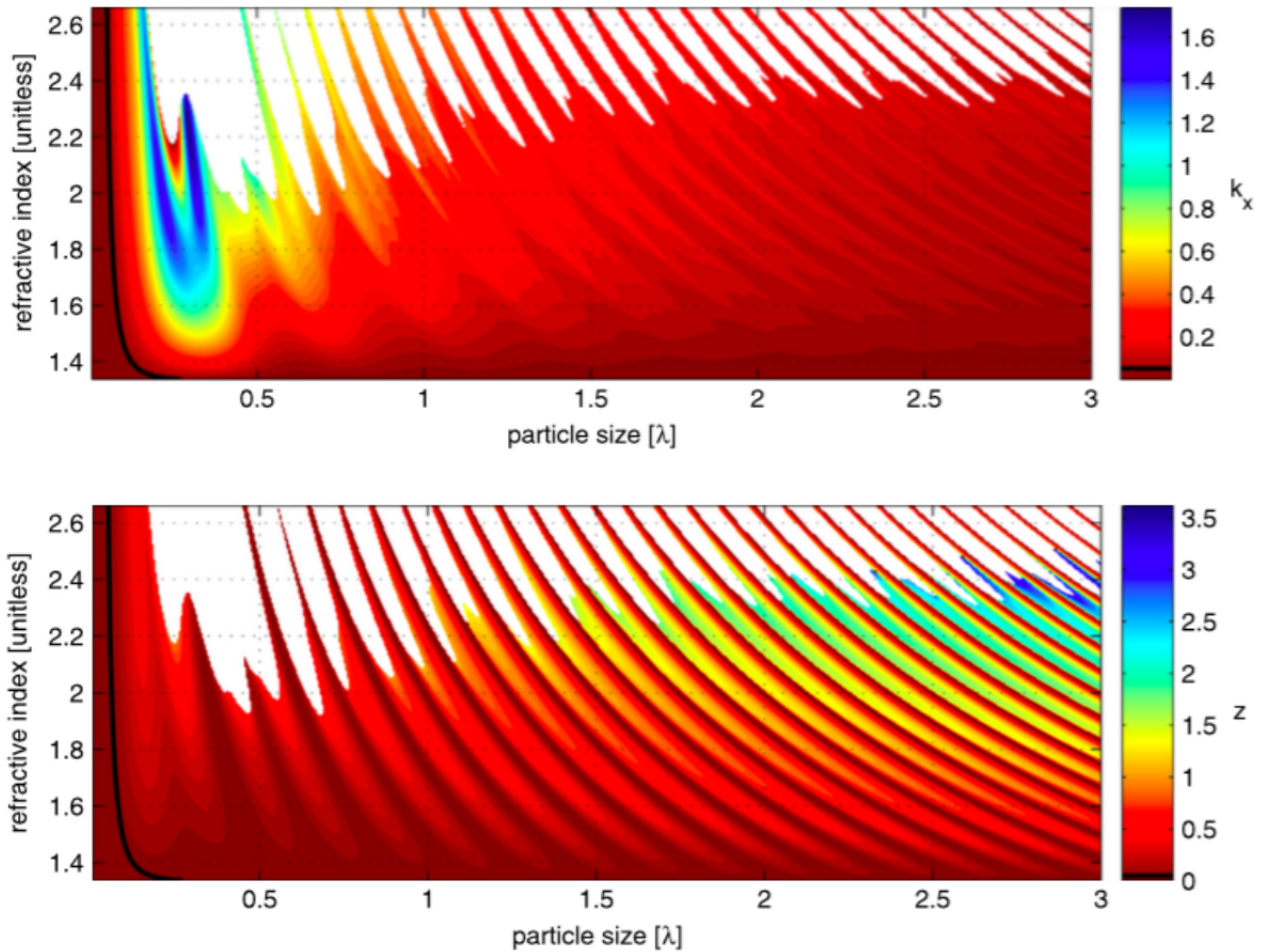
Figure 7.1: The effect that refractive index and particle size have on trap stiffness and trapping position. The top panel shows the lateral trap stiffness, while the bottom panel shows the depth at which equilibrium positions occur (white areas show that there are no equilibrium positions i.e. trapping is not possible for these particles). Trapping was modelled for particles in water, with particles sign given relative to wavelength of the trapping beam in vacuum. Edited, with permission, from [195].

are reliably trapped. For high refractive-index particles a band-like structure becomes apparent, with only particles of certain sizes being trappable.

Even when an object is capable of being trapped by an optical tweezers system, it may not be desirable to do so. The primary reason for this is to avoid damaging the object with the optical power in the beam. Ashkin himself was familiar with this phenomenon, which he dubbed "photocution", whereby microscopic organisms killed by the optical radiation from the trapping beam. As the scattering of such an object was being observed, it was found that there was a sudden, massive increase in scattering from the organism after which only very minimal scattering occurred. This subsequent low-level scattering came from the outer shell of the dead organism. Less extreme forms of photodamage can also occur, or trapping beams can simply lead to quenching in the signal from a particle which want to be avoided. Even if photodamage is not a major concern, it may still be
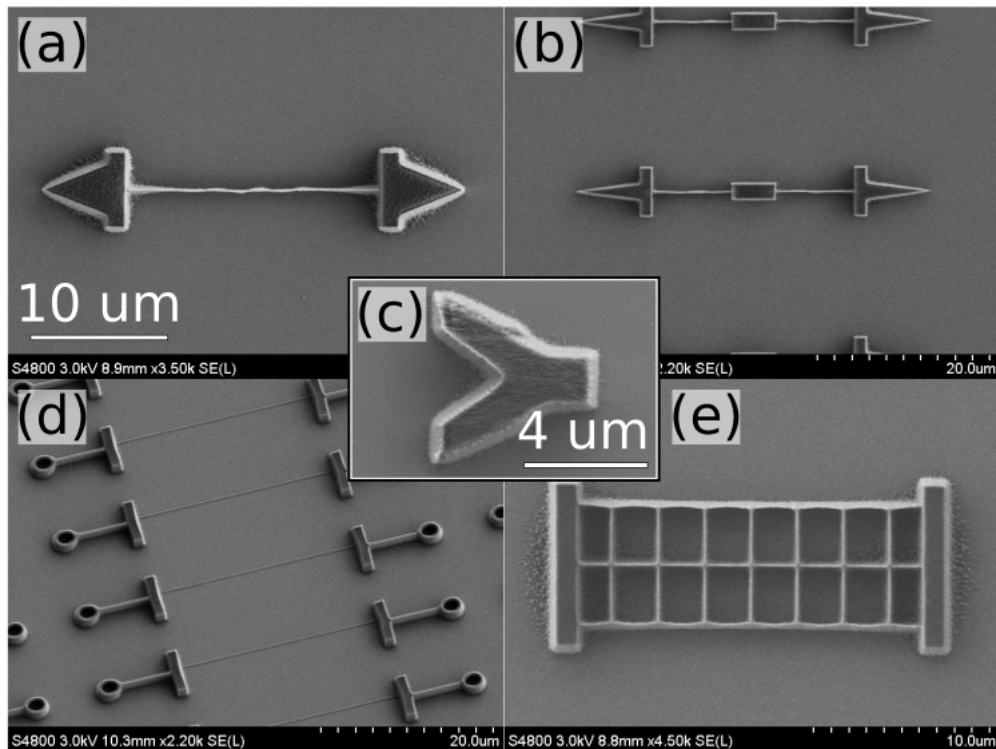
Figure 7.2: SEM image showing some the various microtools which can be made using the presented fabrication protocol. (a), (b), and (d) show various designs for microscopic tweezers that can be used to sort novel particles like those shown in (c). (e) Microscopic filters can also be made that will be moved through a solution of mixed particles, allowing small particles to pass through them while collecting larger particles.

desirable to not have the light from a trapping beam interact with the particle. This may be for the simple reason that the presence of light alters the state of the particle in some unknown way, and to properly study the particle's behaviour it must be observed in an unaltered state.

The purpose of this work is to create a class of microscopic tools which we know can be trapped is a predictable way, without any concern for their degradation. These microtools can then be used to actuate particles in a microfluidic environment. This allows these particles to be manipulated and sorted without them ever having the "see" the trapping beam. Furthermore, particles which are not conformable to optical manipulation can still be conformable to the mechanical sorting outlined here.

7.1.1 Methods

The microtools discussed here were fabricated using the same protocol outlined in chapter 3, the only difference being that where the thin layer were used to define the membrane features they now define fine features such as threads, with the thicker layer still defining the handles of the object, in addition to defining any large features in the microtools. Figure 7.2 shows a collection of the some of the devices made using this protocol.

Figure 7.2 (a),(b), and (d) show three variations on a microtweezer design. These were made for particle sorting applications, with novel particles also being fabricated which couldn't be trapped
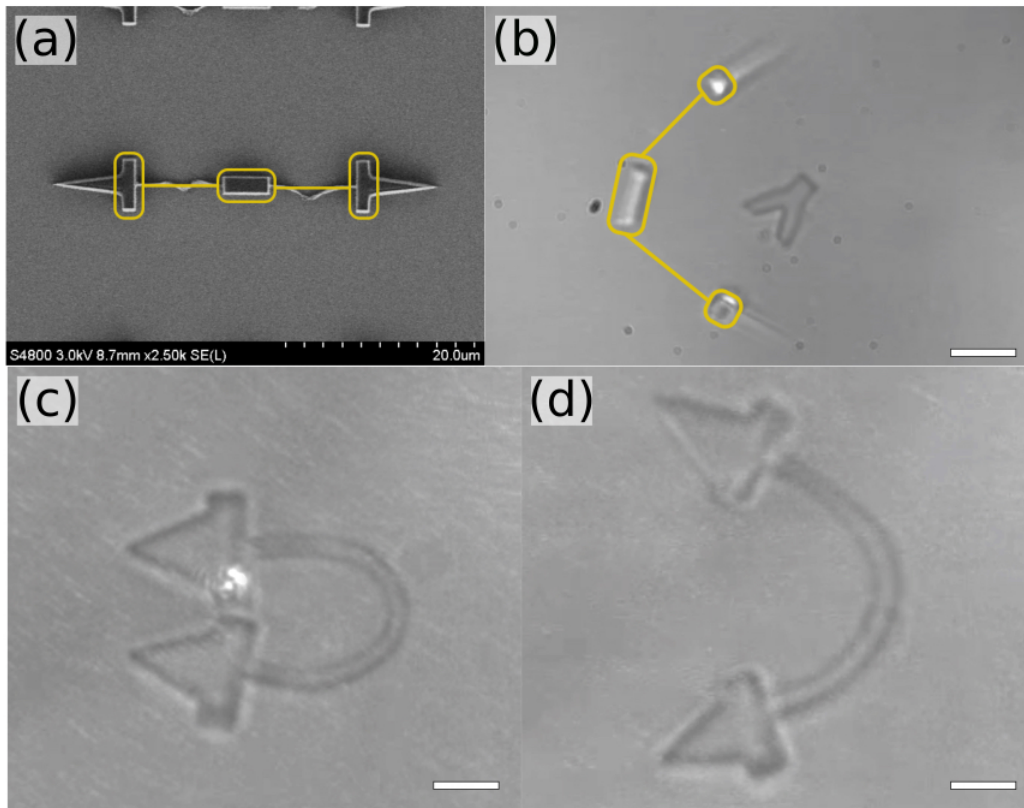
Figure 7.3: Performance of microscopic tweezers. (a) SEM image of microtweezers which are then (b–d) deployed into a microfluidic environment. (c–d) show the ability of such devices to bend to a great extent. Sclae bars are 5 µm.

directly (figure 7.2(c)). The other class of tools that were made were for particle filtering applications, and can be seen in figure 7.2(e). This were designed to be trapped, and moved through the microfluidic environment, where they would sort particles by allowing small particles to pass through them while larger particles became trapped by them.

When introduced to an optical trapping environment, these devices all become trapped via their handles. All of the handles used in these designs were rod-like in nature, meaning the the tools reoriented themselves once they were trapped such that the long axis of the rods aligned itself with the optical axis. This reorientation behaviour is demonstrated in figure 7.3(a–b).

Once in this altered orientation, they are trapped stably and can be manoeuvred through the sample with a high degree of control. By moving the two handles towards each other in a pinsing motion, the tweezers can be opened and closed, with the thread section becoming increasingly bent (figure 7.3(c)).

7.1.2 Results

A sample was made up from novel-shaped particles (7.2(c)) and microtweezers (7.2(b)). The first stage of the experiment was to try and manipulate the particles directly. It was found that the

particles would either be kicked away by the optical trapping beam, or would sometimes become trapped very loosely. Trapping would only occur when the particles had reorientated themselves such that one of their diagonals was aligned with the optical axis. In this configuration they could be moved through the sample if the movement speed was kept very slow, however they would eventually fall out of the traps and be kicked away from the beam.

By contrast, the microtweezers were trapped stably and reliably. They would reorient themselves as described above, and could then be manoeuvred through the sample towards one of the particles. By approaching a particle in an open configuration and then closing the tweezers around it, the object could be "trapped". This was accomplished without the particle feeling the influence of the trapping beams at all. With the tweezers closed around the particle, they could be moved through the microfluidic environment, transporting the trapped particle with them.

A demonstration of this sort of particle transport is depicted in figure 7.4. These still frames from a typical video of the sorting process show first, 7.4 (a) the tweezers approaching the particle in an opened configuration, before, (b) closing themselves around the particle and (c) transporting it through the sample. Key features of this sort of particle transport is that the particle itself does not interact with the trapping beams, and that, additionally, it maintains a "flat" orientation i.e. its longest axis lies inside the focal plane for the duration of the transportation process.

7.1.3 Discussion

Particle transportation is already something that is achieved at a high level, with many particles capable of being sorted and transported simultaneously. However, there is always the issue that these particles have to be directly exposed to the light-beam (assuming light-based transport and sorting). This carries with it its own problems, namely photodamage or other forms of alteration of the particle. In many situations, direct manipulation of particles is not even possible.

Our demonstration of particle transport using lithographically defined microtweezers circumvents both of these concerns. We have shown that microtweezers can be used to manipulate particles which themselves cannot by trapped, and that they can do so without exposing the particle to the trapping light directly. These tools, alongside those with complimentary designs (such as filters) can offer great impact to the field of microfluidics.

The tools demonstrated here went through only a few simply stages of design iteration. The basic features of the microtweezers are the cuboidal handles which allow them to be trapped, and which cause them to reorientate themselves as shown above, and the heads of the tweezers which directly interact with the target particle. Neither of these aspects of the tweezer design have been optimised.

The handles were designed such that their short axes were approximately comparable to the beam waist of the trapping beam. This condition was chosen as it is typically particles with these diameters that are trapped most strongly in an optical trap. The length of the trapping handles was to a large extent somewhat arbitrary. In order to aid with future simulations, no handles were made that had aspect ratios in excess of 4:1. This was because 4:1 is the largest aspect ratio of particle which can faithfully have its T-matrix calculated using the optical tweezers toolbox software. The subject of handle optimisation is left for appendix A.

The tweezer heads were first made as relatively large triangles. Tweezers design quickly moved away from this when it was found that tweezer heads of that size created a lot of drag when the tweezers were moved. This was particularly problematic when it came to closing the tweezers around an object, as this high drag force would often cause the tweezers to fall out of the traps. In those cases where they did not fall out of the traps, they would not close in an upright orientation. Instead, the drag would force them to turn slightly as they were closed. This was a problem as it reduced the finesse with which they could interact with particles. To counteract this problem, subsequent iterations all made use of smaller tweezer heads which experienced far less drag. Often the issue at
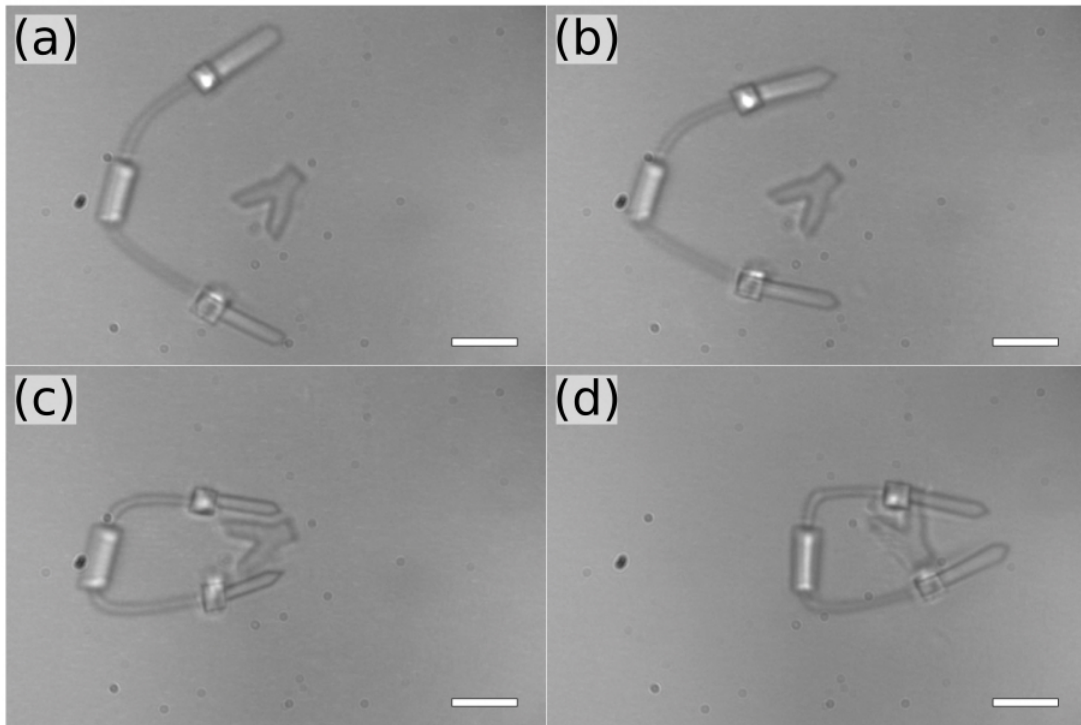
Figure 7.4: Stills of microscopic tweezers being used to transport a novel particle through the sample. (a) Tweezers are trapped, and held in an open configuration before (b–c) being brough toward the particle and closed around it. (d) Once the tweezers are closed around the particle it can then be transported through the sample. Scale bars are 5 μm.

this stage was that the tweezer heads were too small. Although they did not experience crippling levels of drag force, they were so small that it was difficult to grab anything with them. The most recent design strike a balance between these two extremes: the tweezer heads are very slim until the tip, at which point they become larger again, taking the form of a ring (7.2 (e)). This design allows a convenient margin of error in the handling of particles while also ensuring that the tweezer heads do not become unwieldy due to excessive drag forces.

Another aspect to the microtweezer design is the thread that joins the two heads together. At first these threads were simply made in the same stage as the tweezer heads, and as a result they were quite thick. After that, the two-stage approach was taken, with the threads being made from much thinner SU-8. This helped to make them more flexible, although there were still problems regarding how the tweezers opened and closed. The basic issue was that the tweezers would close at extreme angles to each other, making precise manipulation difficult. This was counteracted by adding a thick section in the middle of the thread such that the closing motion happened about two joints. These joints were the points where the thin threads met the thicker sections. By incorporating a thicker, more rigid, central section on the thread, the tweezer heads closed together with a more desirable orientation. This made it far easier to hold and manipulate things in the sample.

Although there are limits to the technique shown here, in particular there are faster and more efficient methods for sorting large number of particles in parallel. The goal of this work is not to create a technology that supersedes all other techniques for particle transport and sorting. Rather, this work should be seen to fill a particular niche. That niche is optical transport and sorting of

particles that fall into certain a parameter space that would have traditionally meant they could not be addressed optically. The form of mechanical actuation shown here is capable of venturing into these forbidden regions of parameter space for us, and we simply use optical tweezers as the enabling technology. The other consideration to make is that these microscopic tools would probably only be implemented in scenarios where highly directed, specific sorting was required, at most addressing a few particles at a time. This is certainly not a problem in of itself. There are many areas of research where such tools would find great use - studies on the single-cell level being just one of them.

I am currently writing a paper on this topic, which will be finalised upon the conclusion of a thorough study into the trap stiffness of handles depends upon their size and shape. The importance of this study is outlined in appendix A.

7.2 In-situ photonic membrane filters

As has already been discussed, PM have been demonstrated to act in various situations owing to the fact that they can exhibit the properties of a vast spectrum of optical elements. This broad scope of applicability stems from their ability to act as a host material for a flexible metasurface. By engineering the structure and periodicity of the MS, bespoke PM can be made that are targeted for specific applications. PM can inherit the properties of any number of devices, and because of their flexible nature they can pass these properties on to external objects simply by conforming to them physically.

PM have been demonstrated that act as optical filters [23]. They have been used to filter the output of optical fibres without the need to pattern the fibre facet in any way. The PM is simply wrapped around the end facet of the fibre and the light is filtered. The PM can be easily removed, and reapplied repeatedly, leaving the fibre unaltered. Similarly functionalised PM can function as lenses, sensors, and axicons, amongst other things.

PM are versatile and precise tools, but they have yet to be utilised in a microfluidic setting. In this section we discuss their application to *in situ* filtering, whereby a PM is trapped and manipulated via optical tweezers with the aim of filtering the optical output of a collection of fluorescent particles. The PM discussed in this section are 20 µm in size. The filtering area that is patterned on them can cover the PM entirely, or be smaller than 1 µm square, depending on the desires of the user. Once trapped and positioned over a cell or particle, they have the potential to filter a particle's output in a highly localised manner. Additional applications of PM in microfluidic environments are discussed in section 7.2.2, such as using PM that have been functionalised to act as gratings or lenses.

7.2.1 Outline of experiment

Figure 7.5 depicts what such an experiment might look like. A microscope slide is prepared by first mixing together two distinct fluorescent-particle solutions. Both species of particle could be pumped with blue light, with one species fluorescing with red light and the other with green light. This solution is then applied to the microscope slide and allowed to dry. A sample is then prepared using a solution of PM filters, but instead of using a blank microscope slide to seal the sample, the slide with beads adhered to it is used instead. The PM are then freely suspended against a stationary background of fluorescent beads (see top panel, figure 7.5).

If one was to pump the sample with blue light, and measured the transmitted light with a spectrometer, one would expect to obtain a fluorescent signal that was approximately half green and half red. The addition of an adjustable aperture would allow one to measure the spectrum from a reduced section of the sample instead of the sample as a whole. Because the optical trapping laser enters the sample from the opposite side, the adhered particles do not scatter any of the beam and
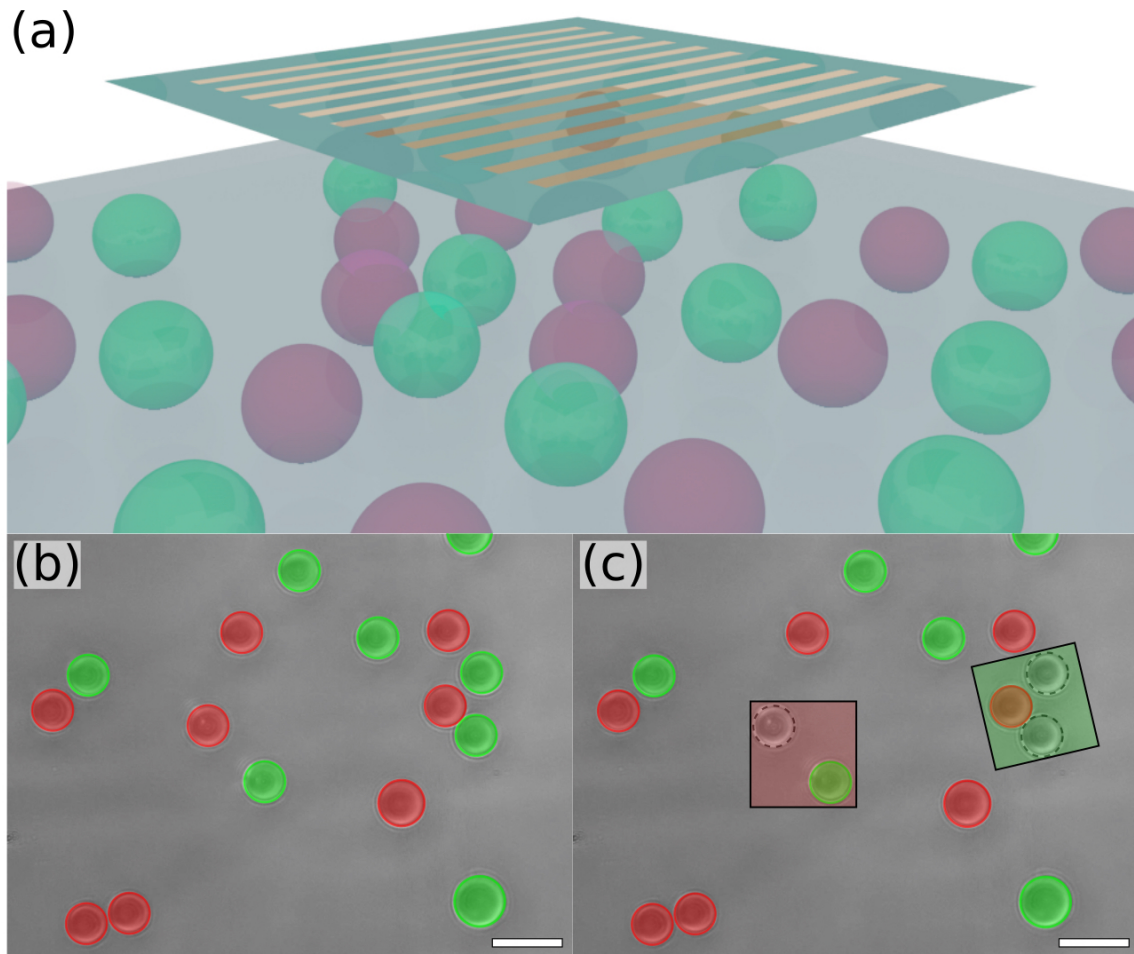
Figure 7.5: Images depicting the application of *in situ* filters to a microfluidic environment Top panel shows a sketch of what such an experiment would look like, with a PM being trapped and positioned above two species of fluorescent particles; one emitting in the red and the other in green. Bottom panels show a mock-up of such a sample as seen through microscope, with the particles being false-coloured to show what type of fluorescence they exhibit. When the appropriate membrane is used the fluorescence from that particle is blocked will other particles are unaffected. Scale bars are 10 μm.

therefore do not affect the quality of the traps. This allows PM to be trapped in the sample and positioned between the layer of fluorescent particles and the objective lens. That is to say, if a PM filter is placed above a bead, the fluorescent signal from the bead must first pass through the PM before it is detected by the spectrometer.

One can envisage two types of PM filters being made, one that filtered out the green fluorescence and one that filtered out the red fluorescence. Figure 7.5(b–c) show a mock-up of a what such a sample might look like. In figure 7.5(b) a random population of red- and green-fluorescent particles are observable. The particles have been colour-coded depending on the type of fluorescence they emit. Figure 7.5(c) shows the effect of introducing the PM filters, represented by the coloured squares. Positioning a red filter over a red-fluorescing particle, or a green filter over a green-fluorescent

particle, would block the fluorescence from that particle, while placing a non-matching filter over a particle would have no effect. The particular filtering function attributable to a PM could be easily ascertained by incorporating markers into the membrane design, making them easily identifiable.

In this way, fluorescence could be selectively turned on or off simply by applying the correct PM to the particle in question. Alternatively, with polarisation-sensitive filters, one can probe the polarisation state of the fluorescence simply by rotating the PM using the optical tweezers.

7.2.2 Discussion

The ability to filter the output of objects in a microfluidic environment holds promise for the field of microfludics and biophotonics. One can imagine the impact this could have in an experiment where, for example, one was faced a large collection of cells, each prone to fluorescence. Cells could be addressed in turn, their optical characteristics being determined in the absence of fluorescent signals which typical obfuscate data of interest. Clearly a combination of filters can be used to generate a customised filtering landscape, allowing the user to optimise certain conditions for their particular application. This could allow one to strip back the various layers of optical output in order to understand the interplay between the fluorescence of two neighbouring particles, for example.

As mentioned above, PM are not limited only to function as filters, but rather can assume the role of a range of optical elements. One can imagine incorporating PM into a number of microfluidic experiments, each of which would benefit from their versatile properties. One example could be the application of PM to optical fibres in a microfluidic channel. Spherical beads have been used in these systems to influence the coupling between two optical fibres. The bead deflects the light coming from the input fibre and therefor determines the out-coupling of the light into the second fibre [196]. The role of the spherical bead in this situation could easily be replaced by a PM that has been functionalised to act as a blazed grating, for example. The advantage of the PM is that it could be patterned to function as a superposition of any number of gratings, thereby coupling light out to a desired selection of the output fibres.

As a further example, the controllable microscopic objective lens demonstrated by Sasaki et al. [6] could also be extended through the use of PM. PM made to act as lenses could provide this same function without the considerable spherical aberrations that affect spherical objectives. In addition to this, one can imagine having a range of PM-base optical elements all controllable in the same way that the lens would be, and each performing with a high level of precision. Successful deployment of PM-based filter is the first, exciting, step towards realising this vision.

7.3 Conclusion

This chapter has addressed several avenues of exploration which were not able to be investigated fully. That being said, they are all important and fit into the theme of microscopic tools in a microfluidic environment. As we have already seen, this field is expanding at the moment and has the potential to provide some nice applications to fields such as particle sorting, in situ, single-cell sensing and filtering, etc. These technologies rely on optical tweezers as an actuation method, and yet for optical tweezers to be used most effectively the system with which they are interacting with must be optimised for them.

Here we have shown the potential uses of two types of microtools: a PM-based filter, and a microtweezer tool. Using the same manipulation procedure that was outlined in chapter 5, the PM filter could be positioned over cells or particles and filter their fluorescent output - or perhaps even shelter them from the exciting radiation in the first place. We have shown that the microtweezer tools are capable of transporting novel objects through a microfluidic environment, most usefully when these objects cannot themselves be trapped directly. Methods of particle manipulation based

on this same concept are of great potential impact. They allow new classes of particles to be sorted using optical tweezers, and also they allow objects to be transported without having to expose them directly to the laser beam that is doing the trapping. This latter aspect could be particularly interesting to those working with systems where phototoxicity is a concern.

Finally, the question of finding the optimum handle geometry with which to trap PM is addressed. This is of chief concern to the experimenter, as it is through the handles that the PM and the optical tweezers interact. To ensure that one is using optical tweezers technology to its fullest potential, the highest possible trap stiffness must be achieved. The method outlined here of using a genetic algorithm to find the optimum handle shape via T-matrix calculation is the proposed solution to this problem.

The next steps with the work in this chapter are rather straightforward. In the case of the PM filters, the proposed experiment should simply be carried out. For the case of the optical microtweezers, a more advanced application of their use could be envisaged. Although they have been shown to be able to transport objects which themselves cannot be manipulated, a more convincing demonstration of the power of optical microtweezers might involve the sorting of a large collection of various novel-shaped particles. It would first be demonstrated that no individual particle could be trapped directly, and then through the use of the microtweezers, these particles could all be moved such that they were sorted into separated clusters, based on the type of particle they were. Finally, the work concerning the modelling of optimum handles for PM and related microtools could be carried out. A good framework for calculating the T-matrix of various shapes already exists in the MATLAB environment created by Nieminen, the only additional complication would be to embed these calculations into a genetic algorithm.

Achieving these goals gives a fuller and more complete treatment of what is a rich and exciting field. As this field continues to grow, tools with more and more novel designs will no doubt appear. Understanding the role that the tools presented here can play in such an environment is a good thing to be able to do, and developing a method to find the best handles is something that will never not be relevant to the problem of trapping structures in a microfluidic environment.

Conclusion

8.1 Thesis Summary

In this thesis I have presented a fabrication and optical manipulation protocol that enables PM to be trapped via optical tweezers. PM are versatile and robust devices which can be used for sensing and filtering applications, amongst other things. At the heart of the PM design is the inclusion of handle-like features. These handles make the PM receptive to optical tweezers technology, where they otherwise would not be.

The motivation for this work, as outlined in chapters 1 and 2, comes from transferring the PM from a macroscopic, in-air, environment to a microfluidic environment. PM have been shown to be useful at macroscopic scales, where they have been wrapped around the end facet of an optical fibre and filtered its output. The versatility of PM means that they can exhibit the optical functionality of any arbitrary optical element - this could be a lens, filter, grating, or axicon, for example.

Also outlined in chapters 1 and 2 were some of the challenges associated with such an endeavour. Typically extended objects (such as PM) are not compliant with manipulation via optical tweezers. This is due to their extreme aspect ratios, and lack of features which substantially refract the light from the trapping beam. As a result, extended objects will usually just be pushed away by the beam as the optical scattering force that acts on them greatly outweighs the gradient force needed to form a stable trapping position. In the cases where stable trapping is possible, the object will usually reorient itself in the trap such that its longest axis lies along the beam axis.

A popular way of bypassing these issues, and making extended objects controllable via optical tweezers, is structure-mediated design. With a structure-mediated design approach, one incorporates additional features into the object either during or post-fabrication. These additional features themselves are compatible with optical tweezers technology, and can be used as "handles". This is approach is part of a larger trend in optical manipulation which seeks a more holistic approach to optical trapping. It is recognised that both the trapping beam and trapped particle play an equal role in the trapping experiment, and attention is paid to both of them.

Structure-mediated design was utilised in this thesis, and was discussed in chapters 3 and 4. Chapter 3 explained the modifications made to the PM, namely the inclusion of cuboidal handles. Also discussed here were modifications to the structure of the PM in order to make them more flexible. In chapter 4 the other aspect to this holistic approach - the trapping beam - was addressed.

The applications of PM and microtools were outlined in chapters 5 through 7. In chapter 5 I demonstrated that PM can be manipulated via optical tweezers, with full 6DOF control. In chapter 6 I showed that flexible SERS substrates, based on PM, are capable of taking SERS readings from an object that has an undulating surface structure. Because the PM is flexible it can take readings even from the deep valley sections of the object, simply by conforming to the object's surface. In

chapter 7 I gave an outline of how our applications to microfluidcs and microrobotics might progress. I outlined an experiment which can be performed using PM to act as optical filters in a microfluidic environment. I also showed that microscopic tools such as microtweezers can find use in this area, as a means of manipulating and transporting novel objects. Finally, I discussed how handle design might be optimised through the use of T-matrix calculations embedded in a genetic algorithm.

8.2 Outlook

The primary goal of this thesis - manipulating a PM with optical tweezers - was achieved. The fabrication and manipulation protocol reported here offers a great improvement on our ability to trap extended objects. This improvement comes not just from the precision with which movements can be made, but also from the range of motions that are possible. Nevertheless, a number of areas still remain that can be investigated or improved on. In this section I will highlight a few of these areas and outline the research steps that I feel should be taken next.

8.2.1 Optical manipulation of PM

While the control over PM demonstrated in this thesis is notable, there are certain fundamental limits on its performance. One example is the extent to which PM can be rotated out of the focal plane. This originates from the limited depth of focus of the objective lens, and the deterioration in the beam's wavefront as the focus is pushed deeper into the sample. As a result, if one attempts to rotate a PM out of the focal plane too far the handles eventually fall out of the traps.

One simple counter to this is to make further use of structure-mediated design. Similar to the design for the microtweezers, one can imagine patterning PM with rod-like handles to allow them to be controlled at 90°. By combining these two types of handles one could then have access to a greater range of rotations, using cubic handles when small rotations are required and rod-like handles when full 90° rotation is desired.

8.2.2 SERS

The SERS readings reported above demonstrate that flexible SERS substrates can be used to take spectra from curved objects, however the choice of phantom did lead to problems with fluorescence. The first step towards advancing this work is perform a rerun of the described experiment, but with the newer PDMS phantoms taking the place of the SU-8 and glass ones. This will reduce the fluorescence greatly and give a better indication of how are membranes are really working.

After that, the next logical step is to remove the phantom samples altogether and apply the flexible SERS substrates to genuine biological systems. As a first example, the SERS substrates could be used to detect the chemicals present in a fingerprint. Not only would the substrates be able to identify which chemicals were present, but they could also be used to generate a surface profile of the fingerprint itself. At the same time, SERS substrates should also be introduced into the microfluidic environment. Here they would be trapped by optical tweezers as demonstrated for the plain PM, and used to take SERS readings directly form particles or cells.

8.2.3 Optically-controlled microtools

The work on microtools which has been presented in this thesis is novel, and adds value to a rapidly growing field. To further strengthen our contribution in this area, I can see this work progressing along two fronts.

Firstly, the proposed experiment of using PM as optical filters in a microfluidic environment should be carried out. This would involve an additional fabrication step in which gold was deposited

and patterned onto the PM, but otherwise there are no new steps which need to be taken. Secondly, the applications of microtweezers should be explored in more detail. So far they have been used to transport novel particles through a microfluidic environment, however more involved demonstrations should be attempted. The most likely candidate would be a demonstration of optical sorting where several classes of novel particle were organised according to their form. At the same time it would be good to encourage development of other microscopic tools, such as the filters shown above while also developing entirely new devices for new applications.

8.2.4 Optimisation of handle design

As has been mentioned already, the basis for this work relies on structure-mediated design to make optical trapping of PM realisable. The way that light interacts with the PM is through the patterned handles, and therefore it is crucial to devote time to investigate how they can be improved.

Taking this work further I would like to employ the algorithm outlined above. Generating a family of handle shapes and calculating the trap stiffness with which they would be trapped using the T-matrix method seems to be the best approach. By incorporating this into a genetic algorithm whereby the handle shapes that perform best are propagated into the next generation of solutions, an optimum handle shape should eventually be reached after several iterations. Handle designs would then be tested experimentally to see if they performed as predicted.

Developing a reliable method of obtaining optimised handles could potentially be one of the most crucial aspects of this work.

Handle optimisation for photonic membranes

As has been outlined already, the handles used in the various PM and micro-tools were designed with a few basic criteria in mind. The ultimate goal of any handle feature, used in line with structure-mediated design, is to provide the object with a stable trapping position, with that trapping being accomplished with as high a trap stiffness value as possible. For both the case of the PM and the microtool, there exists at least one optimum design which satisfies these criteria. As of yet, neither of these classes of handle have been optimised to best achieve their objective.

In this section we discuss how this optimisation process might be done. The optical tweezer toolbox, developed in MATLAB [194], is proposed as a means to calculate the trap stiffness with which various shaped particles would be trapped by our system. By scanning for the best particle shape using a genetic algorithm, the optimum design of handles could be found.

A.1   Outline of experiment

To ascertain the size and shape of handle which offers the best trap stiffness, the T-matrix of the handles must first be calculated. This is in general, quite complicated for an arbitrary object, and so it is typically calculated computationally. The optical tweezer toolbox, available in MATLAB, is used for this purpose. The T-matrix itself relates the light that is incident on a trapped particle to the light that is scattered from the object, and is unique to the object in question. It does not depend on the condition of the trapping beam, and so it is a beneficial approach in that the T-matrix needs only to be calculated once.

The toolbox calculates the T-matrix using several assumptions, of course, and one of the conditions which must be met in order for the calculation to be valid is that aspect ratios of the shapes considered must not exceed four. The programme will calculate the T-matrix of a given shape, which can be defined by a super-ellipsoid, for example, and from the T-matrix it can deduce the trap stiffness with which that handle will be trapped. The remaining aspect of the algorithm is to scan across a number of handle shapes and record the trap stiffness for each of them, eventually returning the best.

To achieve this, I propose the use of a genetic algorithm. The basis of a genetic algorithm is that one is trying to solve some form of optimisation problem. One starts with a population of cases, each of which is tested to see how well it performs. Those that perform best "survive" while the others do not. Typically the survival rate is around 50 percent. The surviving cases then go on to be parents of the next generation by breeding and forming new cases. These children are tested and again the best are kept while the worst are removed from the pool. After several generations the results well converge unto a single best value, and it is this value that is obtained.
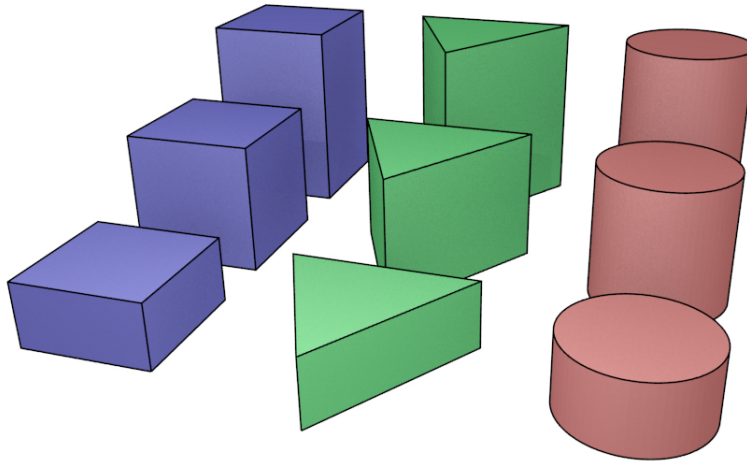
Figure A.1: Various classes of handle which could be used with PM. Square-based (blue), triangle-based (green), and circle-based (red) handles are shown, all of which could be fabricated with different heights.

In the context of this work, the initial population would be roughly ten different shaped handles. One can imagine a cube, cuboid, ellipsoid, pyramid, etc (figure A.1). The T-matrix for each of these is calculated, the best shapes are kept and bred, and the process continues in this way. Once the results of the calculation all begin to converge the associated handle shape is then made.

To test if the results of the simulation are correct various handles in the population sample (across generations) would be fabricated and trapped. Trap stiffness values could then be taken and compared to the simulated results. This would either be done just by trapping the handles directly, or by trapping membranes which used handles of these forms.

A.2 Discussion

The technologies of microtools and PM are limited by the precision with which they can be manipulated. This in turn is limited by how strongly trapped these objects are, which in the case of the objects outlined here means how well trapped their handle-like features are trapped. It is clear then that to maximise the utility of microtools and PM, a proper understanding and treatment of the best choice of handle for trapping is key.

When considering the characteristics of the handles themselves, there are clearly certain limits placed upon them. For example, it is quite likely that handles based on spherical, or partially spherical shapes would perform quite well in a genetic algorithm. However, it would be quite useless to allow such solutions to the trap stiffness problem to permeate through the system - for the simple reason that they could not be made. The fabricational apparatus used is limited to an inherently two-dimensional design, and under-hanging features, like those needed to make spheres, are simply not possible. On the flip side of this, there are things which are not a problem from a fabricational perspective, but which could not be modelled using the algorithim. Perhaps the most notable is the limit placed on the aspect ratio of handles, in that it cannot exceed 4:1. It may well be that the shapes which give the best trapping characteristics have aspect ratios larger than this.

One can go somewhere towards making sure that the parameter space that has been explored really is the best one. One take a look at what shapes perform the best, and simply make some

additional handles which share this same shape and yet have mush larger aspect ratios. By trapping these particles and comparing them to their less-extreme relations, it could be inferred that trap stiffness drops off rapidly if aspect ratio is increased to much, or indeed it could be confirmed that stronger trapping can be obtained in these cases. If it was found that stronger trapping occurs for handles with more extreme aspect ratios then a new programme might need to be used for modelling. Alternatively, the same system can be used, but used with the understanding that the results obtained would carry with them a larger degree of uncertainty that with the case of the shorter handles. There is also a potential issue with the validity of modelling the behaviour of the handles as isolated particles when in reality they are fixed to a large, effectively immovable, membrane.

Bibliography

[1] E. F. Nichols and G. F. Hull, 'A preliminary communication on the pressure of heat and light radiation', *Phys. Rev.*, vol. 13, pp. 307–320, 1901.

[2] P. N. Lebedev, 'Experimental examination of light pressure', *Ann. Phys.*, vol. 6, pp. 433–358, 1901.

[3] A. Ashkin, 'History of optical trapping and manipulation of small-neutral particle, atoms, and molecules', vol. 6, no. 6, pp. 841–856, 2000. DOI: 10.1109/2944.902132.

[4] A. Ashkin, J. M. Dziedzic, J. E. Bjorkholm and S. Chu, 'Observation of a single-beam gradient force optical trap for dielectric particles', *Opt. Lett.*, vol. 11, no. 5, pp. 288–290, 1986.

[5] S. Mohanty, 'Optically-actuated translational and rotational motion at the microscale for microfluidic manipulation and characterization', *Lab Chip*, vol. 12, no. 19, pp. 3624–3636, 2012. DOI: 10.1039/C2LC40538E.

[6] M. Sasaki, T. Kurosawa and K. Hane, 'Micro-objective manipulated with optical tweezers', *Appl. Phys. Lett.*, vol. 70, no. 6, p. 785, 1997. DOI: 10.1063/1.118260.

[7] J. Leach, H. Mushfique, R. Di Leonardo, M. J. Padgett and J. Cooper, 'An optically driven pump for microfluidics', *Lab Chip*, vol. 6, pp. 735–739, 2006.

[8] D. Preece, 'Optical tweezers: wideband microrheology', *J. Opt.*, vol. 13, p. 044 022, 2011.

[9] M. Dao, C. Lim and S. Suresh, 'Mechanics of the human red blood cell deformed by optical tweezers', *J. Mech. Phys. Solids*, vol. 51, no. 11-12, pp. 2259–2280, 2003. DOI: 10.1016/j.jmps.2003.09.019.

[10] K. Svoboda, C. F. Schmidt, B. J. Schnapp and S. M. Block, 'Direct observation of kinesin stepping by optical trapping interferometry', *Nature*, vol. 365, pp. 721–727, 1993.

[11] S. M. Block, D. F. Blair and H. C. Berg, 'Compliance of bacterial flagella measured with optical tweezers', *Nature*, vol. 338, no. 6215, pp. 514 –518, 1989.

[12] D. E. Smith, S. J. Tans, S. B. Smith, S. Grimes, D. L. Anderson and C. Bustamante, 'The bacteriophage straight phi29 portal motor can package dna against a large internal force', *Nature*, vol. 413, no. 6857, pp. 748–752, 2001.

[13] M. Soltani, J. Lin, R. A. Forties, J. T. Inman, S. N. Saraf, R. M. Fulbright, M. Lipson and M. D. Wang, 'Nanophotonic trapping for precise manipulation of biomolecular arrays', *Nat. Nano*, vol. 9, no. 6, pp. 448–452, 2014.

[14] P. P. Calmettes and M. W. Berns, 'Laser-induced multiphoton processes in living cells', *Proc. Natl. Acad. Sci. U.S.A.*, vol. 80, pp. 7197–7199, 1983.

[15] J. Guck, R. Ananthakrishnan, H. Mahmood, T. J. Moon, C. C. Cunningham and J. Käs, 'The Optical Stretcher: A Novel Laser Tool to Micromanipulate Cells', *Biophys. J.*, vol. 81, no. 2, pp. 767–784, 2016. DOI: 10.1016/S0006-3495(01)75740-2.

[16] K. O. Greulich, *Micromanipulation by Light in Biology and Medicine*. Birkhauser Verlag, Germany, 1999.

[17] C. Xie, D. Chen and Y.-q. Li, 'Raman sorting and identification of single living micro-organisms with optical tweezers', *Optics Letters*, vol. 30, no. 14, pp. 1800–1802, 2005. DOI: 10.1364/OL.30.001800.

[18] J. Gluckstad, 'Optical manipulation: Sculpting the object', *Nat. Photon.*, vol. 5, no. 1, pp. 7–8, 2011.

[19] T. Čižmár, M. Mazilu and K. Dholakia, 'In situ wavefront correction and its application to micromanipulation', *Nat. Photon.*, vol. 4, no. May, pp. 388 –394, 2010. DOI: 10.1038/NPHOTON.2010.85.

[20] D McGloin and K Dholakia, 'Bessel beams: Diffraction in a new light', *Contemp. Phys.*, vol. 46, no. 1, pp. 15–28, 2005. DOI: 10.1080/0010751042000275259.

[21] A. Jannasch, A. F. Demirörs, P. D. J. van Oostrum, A. van Blaaderen and E. Schäffer, 'Nanonewton optical force trap employing anti-reflection coated, high-refractive-index titania microspheres', *Nat. Photon.*, vol. 6, no. 7, pp. 469–473, 2012. DOI: 10.1038/nphoton.2012.140.

[22] F. Aieta, P. Genevet, A. M. Kats, N. Yu, R. Blanchard, Z. Gaburro and F. Capasso, 'Aberration-free ultrathin flat lenses and axicons at telecom wavelengths based on plasmonic metasurfaces', *Nano Lett.*, vol. 12, no. 9, pp. 4932–4936, 2012.

[23] A. Di Falco, Y. Zhao and A. Alú, 'Optical metasurfaces with robust angular response on flexible substrates', *Appl. Phys. Lett.*, vol. 99, no. 16, p. 163 110, 2011. DOI: 10.1063/1.3655332.

[24] C. H. Townes, *How the laser happened*. Oxford University Press, 1999.

[25] A. Ashkin, 'Acceleration and trapping of particles by radiation pressure', *Phys. Rev. Lett.*, vol. 24, no. 4, pp. 24–27, 1970.

[26] A Ashkin and J. M. Dziedzic, 'Observation of radiation-pressure trapping of particles by alternating light beams', *Phys. Rev. Lett.*, vol. 54, no. 12, pp. 1245–1248, 1985. DOI: 10.1103/PhysRevLett.54.1245.

[27] A. Ashkin and J. P. Gordon, 'Stability of radiation-pressure particle traps: an optical Earnshaw theorem', *Opt. Lett.*, vol. 8, no. 10, pp. 511–513, 1983. DOI: 10.1364/OL.8.000511.

[28] A. Ashkin, 'Optical Levitation by Radiation Pressure', *Appl. Phys. Lett.*, vol. 19, no. 8, p. 283, 1971. DOI: 10.1063/1.1653919.

[29] M. Wautelet, 'Scaling laws in the macro-, micro- and nanoworlds', *Eur. J. Phys.*, vol. 22, no. 6, pp. 601–611, 2001. DOI: 10.1088/0143-0807/22/6/305.

[30] O. M. Maragò, P. G. Gucciardi and P. H. Jones, *Photonic force microscopy: from femtonewton force sensing to ultra-sensitive spectroscopy*, B. Bushan, Ed. Springer, 2010.

[31] R. N. C. Pfeifer, T. A. Nieminen, N. R. Heckenberg and H. Rubinsztein-Dunlop, 'Colloquium : Momentum of an electromagnetic wave in dielectric media', *Rev. Mod. Phys.*, vol. 79, no. 4, pp. 1197–1216, 2007. DOI: 10.1103/RevModPhys.79.1197.

[32] S. Albaladejo, M. I. Marqués, M. Laroche and J. J. Sáenz, 'Scattering forces from the curl of the spin angular momentum of a light field', *Phys. Rev. Lett.*, no. 102, p. 113 602, 2009.

[33] Y. Harada and T. Asakura, 'Radiation forces on a dielectric sphere in the Rayleigh scattering regime', *Opt. Commun.*, vol. 124, no. 5–6, pp. 529–541, 1996. DOI: http://dx.doi.org/10.1016/0030-4018(95)00753-9.

[34] L. Novotny and B. Hecht, *Principles of Nano-Optics*. Cambridge University Press, 2006.

[35] Y. Roichman, B. Sun, A. Stolarski and D. G. Grier, 'Influence of non-conservative optical forces on the dynamics of optically trapped colloidal spheres: the fountain of probability', *Phys. Rev. Lett.*, vol. 101, p. 128 301, 2008.

[36] G. Pesce, G. Volpe, A. C. De Luca, G. Rusciano and G. Volpe, 'Quantitative assessment of non-conservative radiation forces in an optical trap', *EPL*, vol. 86, no. 3, 2009.

[37] B. T. Draine and J. Goodman, 'Beyond clausius-mossotti: wave propagation on a polarizable point lattice and the discrete dipole approximation', *Astrophys. J.*, vol. 405, pp. 685–697, 1993.

[38] S. E. Skelton, M. Sergides, G. Memoli, O. M. Maragò and P. H. Jones, 'Trapping and deformation of microbubbles in a dual-beam fibre-optic trap', *J. Opt.*, vol. 14, p. 075 706, 2012.

[39] K. Dholakia, P. Reece and M. Gu, 'Optical micromanipulation', *Chem. Soc. Rev.*, vol. 37, no. 1, pp. 42–55, 2008. DOI: 10.1039/B512471A.

[40] K. Svoboda and S. M. Block, 'Biological Applications of Optical Forces', *Annu. Rev. Biophys. Biomol. Struct.*, vol. 23, no. 1, pp. 247–285, 1994. DOI: 10.1146/annurev.bb.23.060194.001335.

[41] M. W. Allersma, F. Gittes, M. J. deCastro, R. J. Stewart and C. F. Schmidt, 'Two-dimensional tracking of ncd motility by back focal plane interferometry', *Biophysical Journal*, vol. 74, no. 2, pp. 1074–1085, DOI: 10.1016/S0006-3495(98)74031-7.

[42] K. Sasaki, M. Koshioka, N. Kitamura and H. Masuhara, 'Laser-scanning micromanipulation and spatial filtering of fine particles', *Jpn. J. Appl. Phys.*, vol. 30, pp. L907–L909, 1991.

[43] K. Visscher, S. P. Gross and S. M. Block, 'Construction of multiple-beam optical traps with nanometer-resolution position sensing', vol. 2, no. 4, pp. 1066–1076, 1996. DOI: 10.1109/2944.577338.

[44] H. He, M. E. J. Friese, N. R. Heckenberg and H. Rubinsztein-Dunlop, 'Direct observation of transfer of angular momentum to absorptive particles from a laser beam with a phase singularity', *Phys. Rev. Lett.*, vol. 75, pp. 826–829, 5 1995. DOI: 10.1103/PhysRevLett.75.826.

[45] M. P. MacDonald, L. Paterson, K. Volke-Sepulveda, J. Arlt, W. Sibbett and K. Dholakia, 'Creation and Manipulation of Three-Dimensional Optically Trapped Structures', *Science*, vol. 296, no. 5570, pp. 1101–1103, 2002. DOI: 10.1126/science.1069571.

[46] M. E. J. Friese, T. A. Nieminen, N. R. Heckenberg and H. Rubinsztein-Dunlop, 'Optical alignment and spinning of laser-trapped microscopic particles', *Nature*, vol. 394, no. 6691, pp. 348–350, 1998.

[47] Y. Arita, M. Mazilu and K. Dholakia, 'Laser-induced rotation and cooling of a trapped microgyroscope in vacuum', *Nat. Commun.*, vol. 4, p. 2374, 2013.

[48] A. O'Neil, I. MacVicar, L. Allen and M. J. Padgett, 'Intrinsic and extrinsic nature of the orbital angular momentum of a light beam', *Phys. Rev. Lett.*, vol. 88, p. 053 601, 2002.

[49] A. I. Bishop, T. A. Nieminen, N. R. Heckenberg and H. Rubinsztein-Dunlop, 'Optical microrheology using rotating laser-trapped particles', *Phys. Rev. Lett.*, vol. 92, p. 198 104, 2004.

[50] Z. Cheng and T. Mason, 'Rotational dissusion microrheology', *Phys. Rev. Lett.*, vol. 90, p. 018 304, 2003.

[51] R. M. Lorenz, J. S. Edgar, G. D. M. Jeffries, Y. Zhao, D. McGloin and D. T. Chiu, 'Vortex-trap-induced fusion of femtoliter-volume aqueous droplets', *Anal. Chem.*, vol. 79, pp. 224–228, 2007.

[52] M. Michihata, T. Hayashi and Y. Takaya, 'Measurement of axial and transverse trapping stiffness of optical tweezers in air using a radially polarized beam', *Appl. Opt.*, vol. 48, no. 32, pp. 6143–6151, 2009. DOI: 10.1364/AO.48.006143.

[53] J. Durnin, J. J. Miceli and J. H. Eberly, 'Diffraction-free beams', *Phys. Rev. E*, vol. 58, pp. 1499–1501, 1987.

[54] M. V. Berry and N. L. Balazs, 'Nonspreading wave packets', *Am. J. Phys.*, vol. 47, pp. 264–267, 1979.

[55] J. Gutiérrez-Vega, M. Iturbe-Castillo and S. Cháavez-Cerda, 'Alternative formulation for invariant optical fields: mathieu beams', *Opt. Lett.*, vol. 25, pp. 1493–1495, 2000.

[56] J. Baumgartl, M. Mazilu and K. Dholakia, 'Optically mediated particle clearing using airy wavepackets', *Nature Photon.*, vol. 2, pp. 675–678, 2008.

[57] J. Baumgartl, G. M. Hannappel, D. J. Stevenson, M. Day D. Gu and K. Dholakia, 'Optical redistribution of microparticles and cells between microwells', *Lab Chip*, vol. 9, pp. 1334–1336, 2009.

[58] C. Alpmann, R. Bowman, M. Woerdemann, M. J. Padgett and C. Denz, 'Mathieu beams as versatile light moulds for 3d micro particle assemblies', *Opt. Express*, vol. 18, pp. 26 084–26 091, 2010.

[59] T. Čižmár, V. Garcés-Chavez, K. Dholakia and P. Zemánek, 'Optical conveyor belt for delivery of submicron objects', *Appl. Phys. Lett.*, vol. 86, p. 174 101, 2005.

[60] V. Karásek, T. Čižmár, O. Brzobohatý, P. Zemánek, V. Garcés-Chavez and K. Dholakia, 'Long-range one-dimensional longitudinal optical binding', *Phys. Rev. Lett.*, vol. 101, p. 143 601, 2008.

[61] A. Chowdhury, B. J. Ackerson and N. A. Clark, 'Laser-induced freezing', *Phys. Rev. Lett.*, vol. 55, pp. 833–836, 1985.

[62] M. Brunner and C. Bechinger, 'Phase behaviour of colloidal molecular crystals on triangular light lattices', *Phys. Rev. Lett.*, vol. 88, p. 248 302, 2002.

[63] J. J. Abbott, Z. Nagy, F. Beyeler and B. J. Nelson, *Robotics in the Small, Part I: Microbotics*, 2007. DOI: 10.1109/MRA.2007.380641.

[64] T. Harada and K. Yoshikawa, 'Mode switching of an optical motor', *Appl. Phys. Lett.*, vol. 81, p. 4850, 2002.

[65] H. Ukita and H. Kawashima, 'Optical rotor capable of controlling clockwise and counter-clockwise rotation in optical tweezers by displacing the trapping position', *Appl. Opt.*, vol. 49, pp. 1991–1996, 2010.

[66] P. Galajda and P. Ormos, 'Rotors produced and driven in laser tweezers with reversed direction of rotation', *Appl. Phys. Lett.*, vol. 80, p. 4653, 2002.

[67] S. Maruo, A. Takaura and Y. Saito, 'Optically driven micropump with a twin spiral microrotor', *Opt. Express*, vol. 17, p. 18 525, 2009.

[68] S. Matsuo, S. Kiyama, Y. Shichijo, T. Tomita, S. Hashimoto, Y. Hosokawa and H. Masuhara, 'Laser microfabrication and rotation of ship-in-a-bottle optical rotators', *Appl. Phys. Lett.*, vol. 93, p. 051 107, 2008.

[69] C.-L. Lin, G. Vitrant, M. Bouriau, R. Casalegno and P. L. Baldeck, 'Optically driven archimedes microscrews for micropump application', *Opt. Express*, vol. 19, p. 8267, 2011.

[70] T. Wu, T. A. Nieminen, S. Mohanty, J. Miotke, R. L. Meyer, H. Rubinsztein-Dunlop and M. W. Berns, 'A photon-driven microrotor can direct nerve fibre growth', *Nat. Photon.*, vol. 6, pp. 62–67, 2012.

[71] S. J. W. Parkin, G. Knöner, T. A. Nieminen, N. R. Heckenberg and H. Rubinsztein-Dunlop, 'Picoliter viscometry using optically rotated particles', *Phys. Rev. E*, vol. 76, p. 041 507, 2007.

[72] E. M. Furst, 'Applications of laser tweezers in complex fluid rheology', *Current Opinion in Colloidal and Interface Science*, vol. 10, no. 79, 2005.

[73] A. Curran, A. Yao, G. Gibson, R. Bowman, J. Cooper and M. J. Padgett, 'Real time characterization of hydrodynamics in optically trapped networks of microparticles', *J. Biophoton.*, vol. 3, pp. 244–251, 2010.

[74] C. Guzmán, H. Flyvbjerg, R. Köszali, C. Ecoffet, L. Forró and S. Jeney, 'In situ viscometry by optical trapping interferometry', *Appl. Phys. Lett.*, vol. 93, p. 184 102, 2008.

[75] S. Juodkazis, V. Mizeikis, S. Matsuo, K. Ueno and H. Misawa, 'Three-dimensional micro- and nano-structuring of materials by tightly focussed laser radiation', *Bull. Chem. Soc. Jpn.*, vol. 81, no. 411–448, 2008.

[76] S. R. Marder, J. L. Bredas and J. W. Perry, 'Materials for multiphoton 3d microfabrication', *MRS Bull.*, vol. 32, pp. 561–565, 2007.

[77] M. Farsari, M. Vamvakaki and B. N. Chichkov, 'Multi-photon polymerization of hybrid materials', *J. Opt.*, vol. 12, no. 12, p. 124 001, 2010.

[78] C. R. Mendonca, D. S. Correa, F. Marlow, T. Voss, P. Tayalia and E. Mazur, 'Three-dimensional fabrication of optically active microstructures containing an electroluminescent polymer', *Appl. Phys. Lett.*, vol. 95, no. 11, p. 113 309, 2009.

[79] J. W. Perry, 'Two beams squeeze feature sizes in optical lithography', *Science*, vol. 324, pp. 892–893, 2009.

[80] M. Stocker, L. Li, R. R. Gattass and J. T. Fourkas, 'Multiphoton photoresists giving nanoscale resolution that is inversely dependent on exposure time', *Nat. Chem.*, vol. 3, no. 3, pp. 223–227, 2011.

[81] J. Fischer and M. Wegener, 'Ultrafast polymerization inhibition by stimulated emission depletion for three-dimensional nanolithography', *Adv. Mater.*, vol. 24, no. 10, OP65–OP69, 2012.

[82] A. Bañas, D. Palima and J. Glückstad, 'Matched-filtering generalized phase contrast using lcos pico-projectors for beam-forming', *Opt. Express*, vol. 20, pp. 9705–9712, 2012.

[83] J.-I. Kato, N. Takeyasu and Y. A. H.-B. Sun, 'Multiple-spot parallel processing for laser micronanofabrication', *Appl. Phys. Lett.*, vol. 86, p. 044 102, 2005.

[84] E. T. Ritschdorff, R. Nielson and J. B. Shear, 'Multi-focal mulitphoton lithography', *Lab Chip*, vol. 12, no. 5, pp. 867–871, 2012.

[85] A. Ovsianikov, Z. Li, J. Torgersen, J. Stampfl and R. Liska, 'Selective functionalizationof 3d matrices via mulitphoton grafting and subsequent click chemistry', *Adv. Funct. Mater.*, vol. 22, pp. 3429–3433, 2012.

[86] E. Stulz, 'DNA architectronics: towards the next generation of bio-inspired materials', *Chemistry*, vol. 18, no. 15, pp. 446–4469, 2012.

[87] K. C. Neuman and A. Nagy, 'Single-molecule force spectroscopy: optical tweezers, magnetic tweezers and atomic force microscopy', *Nat. Methods*, vol. 5, no. 6, pp. 491–505, 2008.

[88] *Topology Optimization: Theory, Models, and Applications*. Springer, 2013.

[89] P. J. Rodrigo, L. Kelemen, C. A. Alonzo, I. R. Perch-Nielsen, J. S. Dam, P. Ormos and J. Glückstad, '2D optical manipulation and assembly of shape-complementary planar microstructures', *Opt. Express*, vol. 15, no. 14, pp. 9009–9014, 2007. DOI: 10.1364/OE.15.009009.

[90] S. M. Oehrlein, J. R. Sanchez-Perez, R. Jacobson, F. S. Flack, R. J. Kershner and M. G. Lagally, 'Translation and manipulation of silicon nanomembranes using holographic optical tweezers', *Nanoscale Res. Lett.*, vol. 6, p. 507, 2011. DOI: 10.1186/1556-276X-6-507.

[91]   M. Villangca, A. Bañas, D. Palima and J. Glückstad, 'Dynamic diffraction-limited light-coupling of 3D-maneuvered wave-guided optical waveguides', *Opt. Express*, vol. 22, no. 15, pp. 17 880–17 889, 2014. DOI: 10.1364/OE.22.017880.

[92]   D. M. Carberry, S. H. Simpson, J. A. Grieve, Y. Wang, H. Schäfer, M. Steinhart, R. Bowman, G. Gibson, M. J. Padgett and S. Hanna, 'Calibration of optically trapped nanotools', *Nanotechnology*, vol. 21, p. 175 501, 2010.

[93]   L. Ikin, D. M. Carberry, G. M. Gibson, M. J. Padgett and M. J. Miles, 'Assembly and force measurement with spm-like probes in holographic optical tweezers', *New J. Phys.*, vol. 11, p. 023 012, 2009.

[94]   D. B. Phillips, J. A. Grieve, S. N. Olof, S. J. Kocher, R Bowman, M. J. Padgett, M. J. Miles and D. M. Carberry, 'Surface imaging using holographic optical tweezers', *Nanotechnology*, vol. 22, no. 28, p. 285 503, 2011.

[95]   M. R. Pollard, S. W. Botchway, B. Chichkov, E. Freeman, R. N. J. Halsall, D. W. K. Jenkins, I. Loader, A. Ovsianikov, A. W. Parker and R. Stevens, 'Optically trapped probes with nanometer-scale tips for femto-newton force measurement', *New J. Phys.*, vol. 12, p. 113 056, 2010.

[96]   D. Palima, A. Bañas, G. Vizsnyiczai, L. Kelemen, P. Ormos and J. Glückstad, 'Wave-guided optical waveguides', *Opt. Express*, vol. 20, pp. 2004–2014, 2012.

[97]   M. J. Villangca, D. Palima, A. R. Banas and J. Gluckstad, *Light-driven micro-tool equipped with a syringe function*, 2016.

[98]   A. Bañas, D. Palima, S. Tauro and J. Glückstad, 'Optimizing light-matter interaction on the biophotonics workstation', *Opt. Photonics News*, vol. 20, no. 12, p. 39, 2010.

[99]   A. Di Falco, M. Ploschner and T. F. Krauss, 'Flexible metamaterials at visible wavelengths', *New J. Phys.*, vol. 12, no. 11, p. 113 006, 2010. DOI: 10.1088/1367-2630/12/11/113006.

[100] I. Bergmair, B. Dastmalchi, M. Bergmair, A. Saeed, W. Hilber, G. Hesser, C. Helgert, E. Pshenay-Severin, T. Pertsch, E. B. Kley, U. Hübner, N. H. Shen, R. Penciu, M. Kafesaki, C. M. Soukoulis, K. Hingerl, M. Muehlberger and R. Schoeftner, 'Single and multilayer metamaterials fabricated by nanoimprint lithography.', *Nanotechnology*, vol. 22, no. 32, p. 325 301, 2011. DOI: 10.1088/0957-4484/22/32/325301.

[101] D. Chanda, K. Shigeta, S. Gupta, T. Cain, A. Carlson, A. Mihi, A. J. Baca, G. R. Bogart, P. Braun and J. A. Rogers, 'Large-area flexible 3D optical negative index metamaterial formed by nanotransfer printing', *Nat. Nanotechnol.*, vol. 6, no. 7, pp. 402–407, 2011. DOI: 10.1038/nnano.2011.82.

[102] I. M. Pryce, K. Aydin, Y. A. Kelaita, R. M. Briggs and H. A. Atwater, 'Highly strained compliant optical metamaterials with large frequency tunability.', *Nano Lett.*, vol. 10, no. 10, pp. 4222–7, 2010. DOI: 10.1021/nl102684x.

[103] X. G. Peralta, M. C. Wanke, C. L. Arrington, J. D. Williams, I. Brener, A. Strikwerda, R. D. Averitt, W. J. Padilla, E. Smirnova, A. J. Taylor and J. F. O'Hara, 'Large-area metamaterials on thin membranes for multilayer and curved applications at terahertz and higher frequencies', *Appl. Phys. Lett.*, vol. 94, no. 16, p. 161 113, 2009. DOI: 10.1063/1.3114416.

[104] J.-B. Brückner, J. L. Rouzo, L. Escoubas, G. Berginc, O. Calvo-Perez, N. Vukadinovic and F. Flory, 'Metamaterial filters at optical-infrared frequencies', *Opt. Express*, vol. 21, no. 14, pp. 16 992–17 006, 2013. DOI: 10.1364/OE.21.016992.

[105] A. C. De Luca, P. Reader-Harris, M. Mazilu, S. Mariggiò, D. Corda and A. Di Falco, 'Reproducible surface-enhanced Raman quantification of biomarkers in multicomponent mixtures', *ACS nano*, vol. 8, no. 3, pp. 2575–2583, 2014.

[106] N. Yu, P. Genevet, A. M. Kats, F. Aieta, J.-P. Tetienne, F. Capasso and Z. Gaburro, 'Light propagation with phase discontinuities: generalized laws of reflection and refraction', *Science*, vol. 334, pp. 333–337, 2011.

[107] P. Reader-Harris and A. Di Falco, 'Nanoplasmonic filters for hollow core photonic crystal fibers', *ACS Photonics*, vol. 1, pp. 985–989, 2014.

[108] Microchem Corp., 'SU-8 2000 Permanent Epoxy Negative Photoresist', *Datasheet*, 2000.

[109] H. Lorenz, M. Despont, N. Fahrni, N. LaBianca, P. Renaud and P. Vettiger, *SU-8: a low-cost negative resist for MEMS*, 1997. DOI: 10.1088/0960-1317/7/3/010.

[110] C. J. Robin, A. Vishnoi and K. N. Jonnalagadda, 'Mechanical Behavior and Anisotropy of Spin-Coated SU-8 Thin Films for MEMS', *J. Microelectromechanical Syst.*, vol. 23, no. 1, pp. 168–180, 2014. DOI: 10.1109/JMEMS.2013.2264341.

[111] A. Del Campo and C. Greiner, 'SU-8: a photoresist for high-aspect-ratio and 3D submicron lithography', *J. Micromech. Microeng.*, vol. 17, no. 6, R81–R95, 2007.

[112] R. Martinez-Duarte and M. Madou, 'SU-8 Photolithography and Its Impact on Microfluidics', in *Microfluidics and Nanofluidics Handbook*, CRC Press, 2011, pp. 231–268. DOI: 10.1201/b11188-11.

[113] K. V. Nemani, K. L. Moodie, J. B. Brennick, A. Su and B. Gimi, '{In vitro and in vivo evaluation of SU-8 biocompatibility}', *Mater. Sci. Eng. C*, vol. 33, no. 7, pp. 4453–4459, 2013. DOI: 10.1016/j.msec.2013.07.001.

[114] A. N. Broers, A. C. F. Hoole and J. M. Ryan, 'Electron beam lithography—Resolution limits', *Microelectronic Engineering*, vol. 32, no. 1, pp. 131–142, 1996. DOI: http://dx.doi.org/10.1016/0167-9317(95)00368-1.

[115] K. W. Lee, S. M. Yoon, S. C. Lee, W. Lee, I.-M. Kim, C. E. Lee and D. H. Kim, 'Secondary electron generation in electron-beam-irradiated solids: resolution limits to nanolithography', *J. Korean Phys. Soc.*, vol. 55, no. 4, pp. 1720–1723, 2009. DOI: 10.3938/jkps.55.1720.

[116] M. Hatzakis, 'Recent developments in electron-resist evaluation techniques', *J. Vac. Sci. Technol.*, vol. 12, no. 6, pp. 1271–1275, 1975.

[117] D. F. Kyser and N. S. Viswanathan, 'Monte Carlo simulation of spatially distributed beams in electron-beam lithography', *J. Vac. Sci. Technol.*, vol. 12, no. 6, p. 1305, 1975. DOI: 10.1116/1.568524.

[118] T. H. P. Chang, 'Proximity effect in electron beam lithography', *J. Vac. Sci. Technol.*, vol. 12, pp. 1271–1275, 1975.

[119] G. Brewer, *Electron-beam Technology in Microelectronic Fabrication*. Academic Press, 1980.

[120] P. Rai-Choudhury, *Handbook of Microlithography, Micromachining, and Microfabrication*, Volume 1: SPIE Press, 1997.

[121] M Nordström, A. Johansson, E. S. Nogueron, B. Clausen, M. Calleja and A. Boisen, 'Investigation of the bond strength between the photo-sensitive polymer SU-8 and gold', *Microelectron. Eng.*, vol. 78–79, no. 1–4, pp. 152–157, 2005.

[122] G. Voskerician, M. S. Shive, R. S. Shawgo, H. Von Recum, J. M. Anderson, M. J. Cima and R. Langer, 'Biocompatibility and biofouling of MEMS drug delivery devices', *Biomaterials*, vol. 24, no. 11, pp. 1959–1967, 2003. DOI: 10.1016/S0142-9612(02)002565-3.

[123] E. Martin-Badosa, M. Montes-Usategui, A. Carnicer, J. Andilla, E. Pleguezuelos and I. Juvells, 'Design strategies for optimizing holographic optical tweezers setups', *J. Opt. A: Pure Appl. Opt.*, vol. 267, p. 16, 2007. DOI: 10.1088/1464-4258/9/8/S22.

[124] *The optical set up diagrams were produced using ComponentLibrary, `http://www.gwoptics. org/ComponentLibrary/`. ComponentLibrary by Alexander Franzen is licensed under a Creative Commons Attribution-NonCommercial 3.0 Unported License.*

[125] C. Hammond, 'A symmetrical representation of the geometrical optics of the light microscope', *J. Microsc.*, vol. 192, no. 1, pp. 63–68, 1998. DOI: `10.1046/j.1365-2818.1998.00408.x`.

[126] S. Block, 'Making light work with optical tweezers', *Nature*, 1992.

[127] S. N. S. Reihani and L. B. Oddershede, 'Optimizing immersion media refractive index improves optical trapping by compensating spherical aberrations', *Opt. Lett.*, vol. 32, no. 14, pp. 1998–2000, 2007. DOI: `10.1364/OL.32.001998`.

[128] M. Reicherter, T. Haist, E. U. Wagemann and H. J. Tiziani, 'Optical particle trapping with computer-generated holograms written on a liquid-crystal display.', *Opt. Lett.*, vol. 24, no. 9, pp. 608–10, 1999.

[129] A. Jesacher, S. Fürhapter, S. Bernet and M. Ritsch-Marte, 'Diffractive optical tweezers in the Fresnel regime', *Opt. Express*, vol. 12, no. 10, pp. 2243–2250, 2004. DOI: `10.1364/OPEX.12.002243`.

[130] B. E. A. Saleh and K. Lu, 'Theory and design of the liquid crystal TV as an optical spatial phase modulator', *Optical Engineering*, vol. 29, no. 3, pp. 240–246, 1990. DOI: `10.1117/12.55584`.

[131] G. Sinclair, P. Jordan, J. Leach and M. Padgett, 'Defining the limits of holographic optical tweezers', *J. Mod. Opt.*, vol. 51, no. 3, pp. 409–414, 2004.

[132] N. Fukuchi, Y. Biqing, Y. Igasaki, N. Yoshida, Y. Kobayashi and T. Hara, 'Oblique-Incidence Characteristics of a Parallel-Aligned Nematic-Liquid-Crystal Spatial Light Modulator', *Opt. Rev.*, vol. 12, no. 5, pp. 372–377, 2005. DOI: `10.1007/s10043-005-0372-8`.

[133] J. E. Curtis, B. A. Koss and D. G. Grier, 'Dynamic holographic optical tweezers', *Opt. Commun.*, vol. 207, no. June, pp. 169–175, 2002.

[134] R. W. Gerchberg and W. O. Saxton, 'A Practical Algorithm for the Determination of Phase from Image and Diffraction Plane Pictures', *Optik*, vol. 35, no. 2, pp. 237–246, 1972.

[135] E. R. Dufresne, G. C. Spalding, M. T. Dearing, S. A. Sheets and D. G. Grier, 'Computer-generated holographic optical tweezer arrays', *Rev. Sci. Instrum.*, vol. 72, no. 3, pp. 1810–1816, 2001. DOI: `10.1063/1.1344176`.

[136] R. Di Leonardo, F. Ianni and G. Ruocco, 'Computer generation of optimal holograms for optical trap arrays', *Opt. Express*, vol. 15, no. 4, pp. 1913–1922, 2007. DOI: `10.1364/OE.15.001913`.

[137] J. Leach, K. Wulff, G. Sinclair, P. Jordan, J. Courtial, L. Thomson, G. Gibson, K. Karunwi, J. Cooper, Z. J. Laczik and M. Padgett, 'Interactive approach to optical tweezers control', *Appl. Opt.*, vol. 45, no. 5, pp. 897–903, 2006. DOI: `10.1364/AO.45.000897`.

[138] G. Gibson, L. Barron, F. Beck, G. Whyte and M. Padgett, 'Optically controlled grippers for manipulating micron-sized particles', *New J. Phys.*, vol. 9, no. 1, pp. 14–14, 2007. DOI: `10.1088/1367-2630/9/1/014`.

[139] C. Pacoret, R. Bowman, G. Gibson, S. Haliyo, D. Carberry, A. Bergander, S. Régnier and M. Padgett, 'Touching the microworld with force-feedback optical tweezers', *Opt. Express*, vol. 17, no. 12, pp. 10 259–10 264, 2009. DOI: `10.1364/OE.17.010259`.

[140] R. W. Bowman, G. Gibson, D. Carberry, L. Picco, M. Miles and M. J. Padgett, 'iTweezers: optical micromanipulation controlled by an Apple iPad', *J. Opt.*, vol. 13, no. 4, p. 044 002, 2011. DOI: `10.1088/2040-8978/13/4/044002`.

[141] G. Whyte, G. Gibson, J. Leach, M. Padgett, D. Robert and M. Miles, 'An optical trapped microhand for manipulating micron-sized objects.', *Opt. Express*, vol. 14, no. 25, pp. 12 497–502, 2006.

[142] K. Seunarine, D. W. Calton, I. Underwood, J. T. M. Stevenson, A. M. Gundlach and M. Begbie, 'Techniques to improve the flatness of reflective micro-optical arrays', *Sensor. Actuat. A: Phys.*, vol. 78, no. 1, pp. 18–27, 1999. DOI: http://dx.doi.org/10.1016/S0924-4247(99)00199-5.

[143] Y. Roichman, A. Waldron, E. Gardel and D. G. Grier, 'Optical traps with geometric aberrations', *Appl. Opt.*, vol. 45, no. 15, pp. 3425–3429, 2006. DOI: 10.1364/AO.45.003425.

[144] C. López-Quesada, J. Andilla and E. Martín-Badosa, 'Correction of aberration in holographic optical tweezers using a Shack-Hartmann sensor', *Appl. Opt.*, vol. 48, no. 6, pp. 1084–1090, 2009. DOI: 10.1364/AO.48.001084.

[145] R. W. Bowman, A. J. Wright and M. J. Padgett, 'An SLM-based Shack–Hartmann wavefront sensor for aberration correction in optical tweezers', *J. Opt.*, vol. 12, no. 12, p. 124 004, 2010. DOI: 10.1088/2040-8978/12/12/124004.

[146] R. J. Noll, 'Zernike polynomials and atmospheric turbulence.', *Journal of the Optical Society of America*, vol. 66, no. 3, pp. 207–211, 1976. DOI: 10.1364/JOSAA.24.000139.

[147] K. D. Wulff, D. G. Cole, R. L. Clark, R. Di Leonardo, J. Leach, J. Cooper, G. Gibson and M. J. Padgett, 'Aberration correction in holographic optical tweezers.', *Opt. Express*, vol. 14, no. 9, pp. 4170–5, 2006.

[148] M. Mazilu, 'Spin angular momentum operators and their conservation', *J. Opt. A: Pure Appl. Opt.*, vol. 11, p. 094 005, 2009.

[149] N. B. Viana, A. Mazolli, P. A. Maia Neto, H. M. Nussenzveig, M. S. Rocha and O. N. Mesquita, 'Absolute calibration of optical tweezers', *Appl. Phys. Lett.*, vol. 88, no. 13, 2006. DOI: http://dx.doi.org/10.1063/1.2189148.

[150] N. B. Viana, M. S. Rocha, O. N. Mesquita, A. Mazolli, P. A. Maia Neto and H. M. Nussenzveig, 'Towards absolute calibration of optical tweezers', *Phys. Rev. E*, vol. 75, no. 2, p. 21 914, 2007. DOI: 10.1103/PhysRevE.75.021914.

[151] A. Pralle, M. Prummer, E.-L. Florin, E. H. K. Stelzer and J. K. H. Hörber, 'Three-dimensional high-resolution particle tracking for optical tweezers by forward scattered light', *Microsc. Res. Tech.*, vol. 44, no. 5, pp. 378–386, 1999. DOI: 10.1002/(SICI)1097-0029(19990301)44:5<378::AID-JEMT10>3.0.CO;2-Z.

[152] A. J. Wright, T. A. Wood, M. R. Dickinson, H. F. Gleeson and T. Mullin, 'The transverse trapping force of an optical trap: Factors affecting its measurement', *J. Mod. Opt.*, vol. 50, no. 10, pp. 1521–1532, 2003. DOI: 10.1080/09500340308235226.

[153] P. M. Hansen, I. M. Tolić-Nørrelykke, H. Flyvbjerg and K. Berg-Sørensen, 'tweezercalib 2.0: Faster version of MatLab package for precise calibration of optical tweezers', *Comput. Phys. Commun.*, vol. 174, no. 6, pp. 518–520, 2006. DOI: http://dx.doi.org/10.1016/j.cpc.2005.11.007.

[154] K. Visscher and S. M. Block, 'Versatile optical traps with feedback control', in *Method. Enzymol.* Ser. Methods in Enzymology, vol. 298, Academic Press, 1998, pp. 460–489. DOI: http://dx.doi.org/10.1016/S0076-6879(98)98040-5.

[155] A. Buosciolo, G. Pesce and A. Sasso, 'New calibration method for position detector for simultaneous measurements of force constants and local viscosity in optical tweezers', *Opt. Commun.*, vol. 230, no. 4–6, pp. 357–368, 2004. DOI: http://dx.doi.org/10.1016/j.optcom.2003.11.062.

[156] G. Sinclair, P. Jordan, J. Courtial, M. Padgett, J. Cooper and Z. Laczik, 'Assembly of 3-dimensional structures using programmable holographic optical tweezers.', *Opt. Express*, vol. 12, no. 22, pp. 5475–80, 2004.

[157] A. Rohrbach, 'Stiffness of Optical Traps: Quantitative Agreement between Experiment and Electromagnetic Theory', *Phys. Rev. Lett.*, vol. 95, no. 16, p. 168 102, 2005. DOI: 10.1103/PhysRevLett.95.168102.

[158] M. Mishchenko, L. Travis and D. Mackowski, 'T-matrix computations of light scattering by nonspherical particles: A review', *J. Quant. Spectrosc. Radiat. Transfer*, vol. 55, no. 5, pp. 535 –575, 1996. DOI: 0022-4073/96.

[159] T. A. Nieminen, H. Rubinsztein-Dunlop and N. R. Heckenberg, 'Calculation of the T-matrix: general considerations and application of the point-matching method', *J. Quant. Spectrosc. Radiat. Transfer*, vol. 79-80, pp. 1019–1029, 2003. DOI: 10.1016/S0022-4073(02)00336-9.

[160] X. Qi, T. A. Nieminen, A. B. Stilgoe, V. L. Y. Loke and H. Rubinsztein-Dunlop, 'Comparison of T-matrix calculation methods for scattering by cylinders in optical tweezers', *Opt. Lett.*, vol. 39, no. 16, pp. 4827–4830, 2014. DOI: 10.1364/OL.39.004827.

[161] C. V. Raman, 'A new radiation', *Proc. Indian Acad. Sci. - Sect. A*, vol. 37, no. 3, pp. 333–341, 1953. DOI: 10.1007/BF03052651.

[162] R. Singh, 'C. V. Raman and the Discovery of the Raman Effect', *Phys. Perspect.*, vol. 4, no. 4, pp. 399–420, 2002. DOI: 10.1007/s000160200002.

[163] A. Smekal, 'Zur quantentheorie der dispersion', *Naturwissenschaften*, vol. 11, no. 43, pp. 873– 875, 1923.

[164] C. V. Raman and K. S. Krishnan, 'A new type of secondary radiation', *Nature*, vol. 121, no. 3048, p. 501, 1928.

[165] E. Smith and G. Dent, *Modern Raman Spectroscopy*. Wiley, 2005.

[166] J. F. Mammone, S. K. Sharma and M. Nicol, 'Raman spectra of methanol and ethanol at pressures up to 100 kbar', *J. Phys. Chem.*, vol. 84, no. 23, pp. 3130–3134, Nov. 1980. DOI: 10.1021/j100460a032.

[167] S. Burikov, T. Dolenko, S. Patsaeva, Y. Starokurov and V. Yuzhakov, 'Raman and IR spectroscopy research on hydrogen bonding in water-ethanol systems', *Mol. Phys.*, vol. 108, no. 18, pp. 2427–2436, 2010. DOI: 10.1080/00268976.2010.516277.

[168] W. L. Peticolas, L. Nafie, P. Stein and B. Faconi, 'Quantum Theory of the Intensities of Molecular Vibrational Spectra', *J. Chem. Phys.*, vol. 52, no. 3, p. 1576, 1970. DOI: 10.1063/1.1673170.

[169] Y. Kato and H. Takuma, 'Experimental Study on the Wavelength Dependence of the Raman Scattering Cross Sections', *J. Chem. Phys.*, vol. 54, no. 12, pp. 5398–5402, 1971. DOI: 10.1063/1.1674840.

[170] M. Fleischmann, P. Hendra and A. McQuillan, 'Raman spectra of pyridine adsorbed at a silver electrode', *Chem. Phys. Lett.*, vol. 26, no. 2, pp. 163–166, May 1974. DOI: 10.1016/0009-2614(74)85388-1.

[171] J. N. Farahani, D. W. Pohl, H.-J. Eisler and B. Hecht, 'Single quantum dot coupled to a scanning optical antenna: A tunable superemitter', *Phys. Rev. Lett.*, vol. 95, p. 017 402, 2005. DOI: 10.1103/PhysRevLett.95.017402.

[172] K. Kneipp, H. Kneipp, I. Itzkan, R. R. Dasari and M. S. Feld, 'Surface-enhanced Raman scattering and biophysics', *J. Phys.: Condens. Matter*, vol. 14, no. 18, R597, 2002.

[173] M. Thomas, S. Mühlig, T. Deckert-Gaudig, C. Rockstuhl, V. Deckert and P. Marquetand, 'Distinguishing chemical and electromagnetic enhancement in surface-enhanced Raman spectra: The case of para -nitrothiophenol', *J. Raman Spectrosc.*, vol. 44, no. 11, pp. 1497–1505, Nov. 2013. DOI: 10.1002/jrs.4377.

[174] M. Moskovits, 'Surface-enhanced spectroscopy', *Rev. Mod. Phys.*, vol. 57, no. 3, pp. 783–826, 1985. DOI: 10.1103/RevModPhys.57.783.

[175] E. C. Le Ru, E. J. Blackie, M. Meyer and P. G. Etchegoin, 'Surface Enhanced Raman Scattering Enhancement Factors: A Comprehensive Study', *J. Phys. Chem. C*, vol. 111, no. 37, pp. 13 794–13 803, 2007. DOI: 10.1021/jp0687908.

[176] S. Nie and S. R. Emory, 'Probing Single Molecules and Single Nanoparticles by Surface-Enhanced Raman Scattering', *Science*, vol. 275, no. 5303, pp. 1102–1106, 1997. DOI: 10.1126/science.275.5303.1102.

[177] D. He, B. Hu, Q.-F. Yao, K. Wang and S.-H. Yu, 'Large-Scale Synthesis of Flexible Free-Sensitivity : Electrospun PVA Nanofibers of Silver Nanoparticles', *ACS Nano*, vol. 3, no. 12, pp. 3993–4002, 2009. DOI: 10.1021/nn900812f.

[178] A. Gutés, C. Carraro and R. Maboudian, 'Silver dendrites from galvanic displacement on commercial aluminum foil as an effective SERS substrate', *J. Am. Chem. Soc.*, vol. 132, no. 5, pp. 1476–1477, 2010. DOI: 10.1021/ja909806t.

[179] A. J. Chung, Y. S. Huh and D. Erickson, 'Large area flexible SERS active substrates using engineered nanostructures', *Nanoscale*, vol. 3, no. 7, pp. 2903–2908, 2011. DOI: 10.1039/c1nr10265f.

[180] W. Wu, L. Liu, Z. Dai, J. Liu, S. Yang, L. Zhou, X. Xiao, C. Jiang and V. A. L. Roy, 'Low-Cost, Disposable, Flexible and Highly Reproducible Screen Printed SERS Substrates for the Detection of Various Chemicals', *Sci. Rep.*, vol. 5, no. October 2014, p. 10 208, 2015. DOI: 10.1038/srep10208.

[181] B.-B. Xu, Z.-C. Ma, L. Wang, R. Zhang, L.-G. Niu, Z. Yang, Y.-L. Zhang, W.-H. Zheng, B. Zhao, Y. Xu, Q.-D. Chen, H. Xia and H.-B. Sun, 'Localized flexible integration of high-efficiency surface enhanced Raman scattering (SERS) monitors into microfluidic channels.', *Lab Chip*, vol. 11, no. 19, pp. 3347–3351, 2011. DOI: 10.1039/c1lc20397e.

[182] M. Fan, Z. Zhang, J. Hu, F. Cheng, C. Wang, C. Tang, J. Lin, A. G. Brolo and H. Zhan, 'Ag decorated sandpaper as flexible SERS substrate for direct swabbing sampling', *Mater. Lett.*, vol. 133, pp. 57–59, 2014. DOI: 10.1016/j.matlet.2014.06.178.

[183] K. D. Alexander, K. Skinner, S. Zhang, H. Wei and R. Lopez, 'Tunable SERS in gold nanorod dimers through strain control on an elastomeric substrate', *Nano Lett.*, vol. 10, no. 11, pp. 4488–4493, 2010. DOI: 10.1021/nl1023172.

[184] W. Lee, S. Y. Lee, R. M. Briber and O. Rabin, 'Self-assembled SERS substrates with tunable surface plasmon resonances', *Adv. Funct. Mater.*, vol. 21, no. 18, pp. 3424–3429, 2011. DOI: 10.1002/adfm.201101218.

[185] Z. M. Zhang, S. Chen, Y. Z. Liang, Z. X. Liu, Q. M. Zhang, L. X. Ding, F. Ye and H. Zhou, 'An intelligent background-correction algorithm for highly fluorescent samples in Raman spectroscopy', *J. Raman Spectrosc.*, vol. 41, no. 6, pp. 659–669, 2010. DOI: 10.1002/jrs.2500.

[186] A. E. Kandjani, M. J. Griffin, R. Ramanathan, S. J. Ippolito, S. K. Bhargava and V. Bansal, 'A new paradigm for signal processing of Raman spectra using a smoothing free algorithm: Coupling continuous wavelet transform with signal removal method', *J. Raman Spectrosc.*, vol. 44, no. 4, pp. 608–621, 2013. DOI: 10.1002/jrs.4232.

[187]   D. Zhang and D. Ben-Amotz, 'Enhanced chemical classification of raman images in the presence of strong fluorescence interference', *Appl. Spectrosc.*, vol. 54, no. 9, pp. 1379–1383, 2000. DOI: 10.1366/0003702001951066.

[188]   A. O'Grady, A. C. Dennis, D. Denvir, J. J. McGarvey and S. E. J. Bell, 'Quantitative Raman spectroscopy of highly fluorescent samples using pseudosecond derivatives and multivariate analysis', *Anal. Chem.*, vol. 73, no. 9, pp. 2058–2065, 2001. DOI: 10.1021/ac0010072.

[189]   R. Deegan, 'Pattern formation in drying drops', *Phys. Rev. E*, vol. 61, no. 1, pp. 475–485, 2000. DOI: 10.1103/PhysRevE.61.475.

[190]   P. J. Yunker, T. Still, M. A. Lohr and A. G. Yodh, 'Suppression of the coffee-ring effect by shape-dependent capillary interactions.', *Nature*, vol. 476, no. 7360, pp. 308–311, Aug. 2011. DOI: 10.1038/nature10344.

[191]   L. Jensen and G. C. Schatz, 'Resonance Raman scattering of rhodamine 6G as calculated using time-dependent density functional theory', *J. Phys. Chem. A*, vol. 110, no. 18, pp. 5973–5977, 2006. DOI: 10.1021/jp0610867.

[192]   E. Widjaja, 'Latent fingerprints analysis using tape-lift, Raman microscopy, and multivariate data analysis methods.', *Analyst*, vol. 134, pp. 769–775, 2009. DOI: 10.1039/b808259f.

[193]   J. S. Day, H. G. M. Edwards, S. A. Dobrowski and A. M. Voice, 'The detection of drugs of abuse in fingerprints using Raman spectroscopy I: Latent fingerprints', *Spectrochim. Acta - Part A Mol. Biomol. Spectrosc.*, vol. 60, pp. 563–568, 2004. DOI: 10.1016/S1386-1425(03)00263-4.

[194]   T. A. Nieminen, V. L. Y. Loke, A. B. Stilgoe, G. Knöner, A. M. Brańczyk, N. R. Heckenberg and H. Rubinsztein-Dunlop, 'Optical tweezers computational toolbox', *J. Opt. A: Pure Appl. Opt.*, vol. 9, no. 8, S196, 2007.

[195]   T. A. Nieminen, N. du Preez-Wilkinson, A. B. Stilgoe, V. L. Y. Loke, A. A. M. Bui and H. Rubinsztein-Dunlop, 'Optical tweezers: Theory and modelling', *J. Quant. Spectrosc. Radiat. Transfer*, vol. 146, pp. 59–80, 2014. DOI: http://dx.doi.org/10.1016/j.jqsrt.2014.04.003.

[196]   P. Domachuk, M. Cronin-Golomb, B. J. Eggleton, S. Mutzenich, G. Rosengarten and A. Mitchell, 'Application of optical trapping to beam manipulation in optofluidics', *Opt. Express*, vol. 13, no. 19, pp. 7265–7275, 2005. DOI: 10.1364/OPEX.13.007265.

List of Figures

List of Tables

Acronyms and Initialisms

2PP two-photon polymerisation. 15–17

6DOF six-degree-of-freedom. 16–18, 45, 50, 77

AD aperture diaphragm. 32, 34

AOM acousto-optic modulator. 12, 13

AR anti-reflection. 10

ATP adenosine triphosphate. 2

BFP back focal plane. 12, 32, 34, 35

CCD charge coupled device imaging sensor. 32, 61

COM centre of mass. 40–43, 48

CWT continuous wavelet transform. 63, 65–67

DC direct current. 26

DI deioinised. 29

DNA deoxyribonucleic acid. 2, 16, 50

DOE diffractive optical element. 13

EBL electron beam lithography. 19–27, 30, 52

EM electromagnetic. 20, 59

FD field diaphragm. 32, 34

FFP front focal plane. 32

FT Fourier transform. 37

FZP Fresnel zone plate. 38, 39

GS Gerchberg-Saxton. 37, 38

GUI graphical user interface. 31, 38, 39

HOT holographical optical tweezers. 4, 31, 32, 34, 36, 38, 40, 42, 45, 47, 52

IPA propan-2-ol. 19, 20, 25–27

IR infrared. 34, 56

LCD liquid crystal display. 35

LED light-emitting diode. 32

LG Laguerre-Gaussian. 13, 14

MM metamaterial. 3, 17

MS metasurface. 3, 17, 18, 73

NA numerical aperture. 6, 17, 31, 32, 34, 52, 61, 62

ND neutral density. 61

NMP *N*-Methyl-2-pyrrolidone. 27, 29

OAM orbital angular momentum. 13

PDMS polydimethylsiloxane. 59, 64, 66, 78

PM photonic membrane. i, 3, 4, 10, 17, 18, 42, 45–53, 66, 69, 73–79, 81, 82

PS polystyrene. 48, 52, 53

Rd6G rhodamine 6G. 4, 55, 59, 64–66

RF radio frequency. 26

RIE reactive ion etching. 19, 26

RNA ribonucleic acid. 16

ROI region of interest. 40, 41

SAM spin angular momentum. 13

SEM scanning electron microscope. 60

SERS surface-enhanced Raman spectroscopy. i, 4, 18–21, 25, 26, 29, 30, 46, 53, 55, 57–68, 77, 78

SLM spatial light modulator. 13, 31, 32, 34–40, 52

SNR signal-to-noise. 66

SPL superposition of prisms and lenses. 38

SPM scanning probe microscopy. 16

UV ultra-violet. 19, 21, 22, 64